UNIVERSITY OF
KWAZULU-NATAL

The evolution of orbital-angular-momentum entanglement of photons in turbulent air

by

Alpha Hamadou Ibrahim

Submitted in fulfillment of the academic requirements for the degree of Doctor of Philosophy in the School of Chemistry and Physics,
University of KwaZulu-Natal, Durban

Supervisor: Dr. Filippus S. Roux

Co-supervisor: Prof. Thomas Konrad

November 2013

Abstract

Quantum entanglement plays an important role in the emerging quantum information processing and communications tasks. To this day, almost all these tasks use quantum systems described by a two dimensional Hilbert space (qubits). The use of multidimensionally entangled quantum systems, provides many advantages. For instance, it has been shown that multidimensional entangled systems provide a higher information capacity and an increased security in quantum cryptography. One way to implement higher dimensional quantum systems is to use the orbital angular momentum (OAM) states of light. The OAM state of light can be used to encode quantum information onto a laser beam which can then be transmitted to a receiver through a turbulent atmosphere. The main question here is how does atmospheric turbulence influence the encoded quantum information?

In the work that follows, we investigate theoretically and experimentally the evolution of the OAM entanglement in atmospheric turbulence. We show how atmospheric turbulence induces cross-talk between the different OAM modes.

We first study numerically and experimentally the decay of OAM entanglement between two qubits propagating in atmospheric turbulence. The turbulence is modelled by a single phase screen based on the Kolmogorov theory of turbulence. It is found that higher order modes are more robust in turbulence. We derive an empirical formula for the distance scale at which entanglement decays in terms of the scale parameters and the OAM value.

Then we study numerically the evolution of OAM entanglement in a turbulent atmosphere modelled by a series of consecutive phase screens. It is found that the evolution of the OAM entanglement can not always be described by a single dimensionless quantity. Under certain conditions, two dimensionless parameters are required to describe the evolution of OAM entanglement in turbulence.

The evolution of OAM entnaglement between two qutrits propagating in turbulence is also considered, it is found that the OAM entanglement between qutrits decays at an equal or faster rate compared to OAM entanglement between qubits.

Our results generally show that the OAM state of light is severely affected by atmospheric turbulence and might not be a suitable candidate for free-space quantum communication.

Declaration 1

The work described in this thesis was carried out at the Council for Scientific and Industrial Research, National Laser Center, while registered with the School of Chemistry and Physics, University of KwaZulu-Natal, Durban, Westville, from February 2011 to November 2013, under the supervision of Dr. Filippus S. Roux and the co-supervision of Prof. Thomas Konrad. These studies represent original work by the author and have not otherwise been submitted in any form for any degree or diploma to any tertiary institution. Where use has been made of the work of others it is duly acknowledged in the text.

Signed: ____________________________

On this _____ day of ___________________2013

As the candidates supervisor I have approved this dissertation for submission.

____
Dr. Filippus S. Roux

On this _____ day of ___________________2013

Declaration 2 – Plagiarism

I, **Alpha Hamadou Ibrahim** declare that

1. The research reported in this dissertation, except where otherwise indicated, is my original research.
2. This dissertation has not been submitted for any degree or examination at any other university.
3. This dissertation does not contain other persons' data, pictures, graphs or other information, unless specifically acknowledged as being sourced from other persons.
4. This dissertation does not contain other persons' writing, unless specifically acknowledged as being sourced from other researchers. Where other written sources have been quoted, then:
    a) Their words have been rewritten but the general information attributed to them has been referenced.
    b) Where their exact words have been used, then their writing has been placed in italics and inside quotation marks, and referenced.
5. This dissertation does not contain text, graphics or tables copied and pasted from the Internet, unless specifically acknowledged, and the source being detailed in the dissertation and in the Bibliography.

Signed: ______________________________

Declaration 3 – Publications

List of publications:

1. A Hamadou Ibrahim, Filippus S. Roux, Melanie McLaren,Thomas Konrad, and Andrew Forbes,“Orbital angular momentum entanglement in turbulence”,
   Physical Review A, 88, 012312
2. A Hamadou Ibrahim, Filippus S. Roux, Sandeep Goyal, Melanie McLaren, Thomas Konrad, and Andrew Forbes, “Observing the decay of orbital angular momentum entanglement, through experimentally simulated turbulence”,
   arXiv:1210.2867 [physics.optics],
3. A Hamadou Ibrahim, Filippus S. Roux, Sandeep Goyal, Melanie McLaren, Thomas Konrad, and Andrew Forbes, “Decay of higher-dimensional entanglement through turbulence”,
   In preparation for publication
4. A Hamadou Ibrahim, Filippus S. Roux, and Thomas Konrad, “Parameter dependence in the atmospheric decoherence of transverse modal entangled photon pairs”,
   In preparation for publication

International conference papers:

1. SPIE Photonics west: Complex Light and Optical Forces VIII , San Francisco, California USA. 1 – 6 February 2014.
   Accepted for Oral presentation: The evolution of OAM-entanglement between two qutrits in turbulence.

2. FiO/LS 2013: Frontiers in Optics and Laser sciences, Orlando, Florida USA. 6 – 10 October 2013.

   Oral presentation: The Decay of the orbital angular momentum entanglement in turbulence.

3. AOIM 2013: 9th International Workshop on Adaptive Optics for Industry and Medicine, Stellenbosch, South Africa. 2 – 6 September 2013.

   Oral presentation: Quantum communication with OAM entangled Photons.

4. International Workshop on Singularities and Topological Structures of Light, Abdus Salam International Centre for Theoretical Physics, Trieste Italy 8 – 12 July 2013.

   Poster presentation: The evolution of OAM entanglement in turbulence.

5. Quantum Africa 2, Mon Aux Sources Hotel, Drakensberg South Africa 3 – 7 September 2012.

   Oral presentation: Numerical study of the Orbital Angular Momentum in atmospheric turbulence.

6. SPIE optics and photonics international conference in San Diego USA 20 – 25 August 2011.

   Oral presentation: Parameter dependence of the decoherence of orbital angular momentum ntanglement due to atmospheric turbulence.

National conference papers:

1. Emerging researcher symposium, International convention centre, CSIR Pretoria,13 29 – 30 October 2013.

   Poster presentation: The evolution of OAM entanglement in turbulence.

2. The 58th annual conference of the South African Institute of Physics, University of ZululandOral Presentation: “Is long distance free-space quantum communication with the OAM state of light feasible?”, 8–12 July 2013.

3. IONS Africa 1, Cathedral Peak Hotel, Drakensberg South Africa 31 August – 02 September 2012.

   Oral presentation: A numerical study of the Orbital Angular Momentum in atmospheric turbulence.

4. The 57th annual conference of the South African Institute of Physics, University of Pretoria, 9 – 13 July 2012

   Oral presentation: Simulating atmospheric turbulence with random phase screens.

5. The 56th annual conference of the South African Institute of Physics, St.Georges Hotel, Pretoria. 12 – 15 July 2011

   Oral presentation: Validation of a numerical simulation to study the decoherence of quantum orbital angular momentum entanglement due to atmospheric turbulence.

6. Emerging researcher symposium, International convention centre, CSIR Pretoria,13 October 2011

   Poster Presentation: Quantum communication with twisted light.

7. The 55th annual conference of the South African Institute of Physics,CSIR International Convention Centre, Pretoria . 27 September - 1 October 2010

   Poster Presentation: Numerical simulation of decoherence of quantum entanglement through atmospheric turbulences.

Signed: ____________________________________

Contents

Abstract i

Declaration 1 iii

Declaration 2 – Plagiarism iv

Declaration 3 – Publications v

List of figures x

List of tables xvi

Symbols and notation xvii

1 Introduction 1

- 1.1 literature review 1
  - 1.1.1 The orbital angular moment of light 1
  - 1.1.2 Quantum entanglement 3
  - 1.1.3 The effect of atmospheric turbulence on the OAM states of light . 6
- 1.2 Objectives 10
- 1.3 Outline of the thesis 11

Acknowledgements 1

2 Theoretical background **12**
2.1 Introduction 12
2.2 The orbital angular momentum of light 13
    2.2.1 Angular momentum in paraxial optics 15
    2.2.2 Optical beam carrying OAM 18
    2.2.3 Generation of light beam with OAM 21
2.3 Quantum entanglement 23
    2.3.1 Spontaneous parametric down-conversion 24
    2.3.2 OAM and multidimensional entanglement 26
    2.3.3 Quantum state tomography 28
2.4 Optical wave in atmospheric turbulence 33
    2.4.1 Statistical description of optical turbulence 34
    2.4.2 Power spectra for refractive-index fluctuations 36
    2.4.3 Simulating atmospheric turbulence: the split-step method 39
    2.4.4 Previous theoretical studies 44
    2.4.5 The single phase screen approximation 44
    2.4.6 The IPE 47
2.5 Summary 50

3 Numerical simulation of the decay of OAM entanglement in turbulence **51**
3.1 Introduction 51
3.2 Numerical simulation 52
    3.2.1 Generating random phase screen 52
    3.2.2 Accuracy of the phase screens 53
    3.2.3 Decoherence process 59
    3.2.4 Validity of the simulation 63
3.3 Results 66
    3.3.1 OAM entanglement through turbulence simulated by a single phase screen 66

3.3.2 OAM entanglement through turbulence simulated by multiple phase screens 71

3.4 Conclusion 81

4 Experimental investigation of the decay of OAM entanglement in turbulence 82

4.1 Introduction 82

4.2 Experimental procedure 83

4.3 Results and discussion 86

4.3.1 Single photon case 88

4.3.2 Two-photon case 90

4.3.3 Truncation problem in the IPE 93

4.4 Conclusions 93

5 Decay of multidimensional entanglement through turbulence 95

5.1 Introduction 95

5.2 Experimental procedure 96

5.3 Numerical procedure 102

5.4 Results and discussion 103

5.5 Simulating down-converted photons with back-projected light 105

5.6 Conclusions 108

6 Conclusion and future work 110

Appendix Appendix A: Calculation of the error bars for the concurrence obtained from the experimental and numerical results 113

List of Figures

2.1 Cross section of the intensity profile and phase of a LG beam with radial index $p = 0$. The phase of the beam goes from zero to 2π ℓ-times. When the beam propagates, the phase follows helical trajectory (last row). . . . 18

2.2 The spiral phase of a LG beam. (a) $\ell = 1$ and (b) $\ell = 2$. 20

2.3 The intensity profile and phase of a BG beam for different values of the radial parameter k_r when $\ell = 1$. 21

2.4 Schematic image of a spiral phase plate. 22

2.5 Hologram used to generate an LG beam with azimuthal index $\ell = 1$. The hologram is obtained by adding a diffraction grating to a spiral phase. . . 22

2.6 Spontaneous parametric down conversion. (a) the non-linear crystal – BBO (Beta Barium Borate) – splits the pump photon into two photons (signal and idler). (b) the combined momentum of the signal and idler photons is equal to the momentum of the pump photon and (c) the combined energy of the signal and idler photons is equal to the energy of the pump photon. 25

2.7 The energy cascade theory of turbulence. 35

2.8 Measuring the phase differences between two coherent beams in turbulence 37

2.9 The split-step method 41

2.10 The split-step method 44

3.1 A graphical representation of a random phase screen. The phase value is given by the grey scale. 53

3.2 A comparison of the structure function of the phase screens with the analytical expression of the structure function. 54

3.3 The shape of the two dimensional Kolmogorov power spectral density with $C_n^2 = 10^{-15}$. 55

3.4 The addition of sub-harmonic samples. 56

3.5 A comparison of the structure function of the phase screens with the analytical expression of the structure function. As we add the sub-harmonics, the structure function of the phase screens approaches the analytical expression. 57

3.6 The scintillation index against the square root of the Rytov variance $\sigma_R^2 = 1.23C_n^2 k^{7/6} z^{11/6}$. 58

3.7 The source generates two photons that are entangled in OAM. Each photon is then sent through a turbulent atmosphere (modelled by a series of phase screens) toward a detector. 59

3.8 The scattering of OAM mode in atmospheric turbulence when a Gaussian beam ($\ell = 0$) propagates for 10 km in strong turbulence ($C_n^2 = 10^{-13}\text{m}^{-2/3}$). Before propagation, only the mode with $\ell = 0$ is present (a). After propagation, the initial mode is scattered into neighbouring modes (b). 60

3.9 The single channel $I \otimes \$$ in Eq. 3.17. Two photons are generated and only one of the two photons propagates in turbulence. 63

3.10 Plot of the concurrences $C\left[(I \otimes \$)|\chi\rangle\langle\chi|\right]$ (partial) and $C\left[(I \otimes \$)|\Psi\rangle\langle\Psi|\right] C(|\chi\rangle)$ (Bell) against the scintillation strength. 64

3.11 $C\left[(I \otimes \$)|\chi\rangle\langle\chi|\right]$ against $C|\chi\rangle$ for 8 different initial states. Each initial state was averaged over 500 realisations of the turbulent medium. The error bars represent the dispersion of each run from the mean. The solid line is the best fitted line through the points. 65

3.12 The concurrence plotted against the scintillation strength (w_0/r_0) when one of the two photons propagates in turbulence. In (a) $|\ell| = 1$, in (b) $|\ell| = 3$, in (c) $|\ell| = 5$ and in (d) $|\ell| = 7$. In the legend, S&R: theoretical curve derived by Smith and Raymer in [84] and NS: Numerical data points. The error bars are calculated as discussed in appendix A. 67

3.13 The concurrence plotted against the scintillation strength (w_0/r_0) when both photons propagate through turbulence. In (a) $|\ell| = 1$, in (b) $|\ell| = 3$, in (c) $|\ell| = 5$ and in (d) $|\ell| = 7$. In the legend, S&R: theoretical curve derived by Smith and Raymer in [84] and NS: Numerical data points. . . 68

3.14 The concurrence (a) and the trace of the density matrix before normalisation (b) plotted against the scintillation strength (w_0/r_0) for different values of ℓ when both photons propagate in turbulence. 68

3.15 The concurrence plotted against the scintillation strength ω_0/r_0 for the S&R theory and the numerical results in the single photon case [(a) and (b)] and in the two-photon case [(c) and (d)]. The horizontal axis is plotted on a logarithmic scale. 70

3.16 The scintillation strength plotted against ℓ on a logarithmic scale for both the single photon case (diamond dots) and the two-photon case (circular dots). The equation of the fitted lines are $\log(\omega_0/r_0) = 0.5\log(\ell) + 0.1303$ in the single photon case and $\log(\omega_0/r_0) = 0.5\log(\ell) + 0.01284$ in the two photon case. 71

3.17 The concurrence plotted against the propagation distance for both the single phase screen and multiple phase screens in the weak scintillation regime. 72

3.18 The concurrence plotted against the scintillation strength (w_0/r_0) for multiple phase screens in the moderate fluctuation regime. 73

3.19 The concurrence plotted against w_0/r_0 (a) and against t (b) for $\ell = 1$ and for different values of $S = \log_{10}(K)$ in the multiple phase screen method. . 75

3.20 Multi phase screen: concurrence plotted against w_0/r_0 76

3.21 The concurrence plotted against w_0/r_0 (a) and against t (b) for $\ell = 5$ and for different values of $S = \log_{10}(K)$ in the multiple phase screen method. . 77

3.22 The concurrence plotted against w_0/r_0 (a) and against t (b) for $\ell = 7$ and for different values of $S = \log_{10}(K)$ in the multiple phase screen method. . 78

3.23 Plots of the concurrence plotted against t for $K = 91.6$ when$|\ell| = 1$. The values of the parameters used for each plot is given in table 3.3 80

4.1 Experimental setup used to detect the OAM eigenstate after SPDC. The plane of the crystal is relayed imaged onto two separate SLMs using lenses, L_1 and L_2 (f_1 = 200 mm and f_2 = 400 mm), where the LG modes are selected. Lenses L_3 and L_4 (f_3 = 500 mm and f_4 = 2 mm) are used to relay image the SLM planes through 10 nm bandwidth interference filters (IF) to the inputs of the single-mode fibres (SMF). The fibres are connected to avalanche photodiodes (APDs), which are then connected to a coincidence counter. 84

4.2 the phase function of the SLM when $\ell = 1$ without the random phase fluctuation simulating turbulence (a) and with the random phase added (b). 85

4.3 The intensity profile of LG beams with different ℓ as they propagates through turbulence with increasing scintillation strength. 86

4.4 Mode scattering under the effect of turbulence given by the coincidence counts for simultaneous measurements of modes with azimuthal index ℓ_A in the signal beam and ℓ_B in the idler beam when only one of the two photons propagates through turbulence [(a), (b) and (c)] and when both photons propagate through turbulence [(d),(e) and (f)]. With no turbulence [(a) and (d)], only anti-correlated coincidences are observed. As the scintillation strength increases to $\omega_0/r_0 = 2$ [(b) and (e)] and $\omega_0/r_0 = 4$ [(c) and (f)], the mode scattering becomes more pronounced. . 87

4.5 The concurrence plotted against the scintillation strength (w_0/r_0) when only one photon is propagated through turbulence. In (a) $|\ell| = 1$, in (b) $|\ell| = 3$, in (c) $|\ell| = 5$ and in (d) $|\ell| = 7$. In the legend, Exp: experimental data points, S&R: theory curve derived by Smith and Raymer in [84], IPE: the infinitesimal propagation equation presented in [90] and NS: Numerical data points. 88

4.6 The concurrence plotted against the scintillation strength (w_0/r_0) when only one photon is propagated through turbulence for $|\ell| = 1, 3, 5$ and 7. (a): the S&R theory; (b): the IPE; (c): The numerical simulation and (d): the experimental results; we normalized the concurrence by dividing the values by the initial value obtained for each ℓ. 89

4.7 The concurrence plotted against the scintillation strength (w_0/r_0) when both photons are propagated through turbulence. In (a) $|\ell| = 1$, in (b) $|\ell| = 3$, in (c) $|\ell| = 5$ and in (d) $|\ell| = 7$. In the legend, Exp: experimental data points, S&R: theory curve derived by Smith and Raymer in [84], IPE: the infinitesimal propagation equation presented in [90] and NS: Numerical data points. 91

4.8 The concurrence plotted against the scintillation strength (w_0/r_0) when both photons propagate through turbulence for $|\ell| = 1, 3, 5$ and 7. (a): the S&R theory; (b): the IPE; (c): The numerical simulation and (d): the experimental results; we normalized the concurrence by dividing the values by the initial value obtained for each ℓ. 92

5.1 The tangle and the concurrence squared plotted against the scintillation strength (w_0/r_0). These curve are the S&R theory calculation for the evolution of the OAM entanglement between two qubits ($|\ell| = 1$) as they evolve in atmospheric turbulence (section. 2.4.5). 98

5.2 the OAM spectrum for LG modes (blue); for BG modes with $k_r =$ 21 rad/mm (green) and for BG modes with $k_r = 35$ rad/mm (red). 99

5.3 Real part of the density matrices describing the state of two qutrits represented by photons generated through SPDC for different ℓ values and both LG and BG modes. The x and y axis represent the basis vectors. . . 101

5.4 The tangle plotted against the scintillation strength (w_0/r_0) for both the experimental (Exp) and numerical (NS) results. (a): $\ell = 1$, (b): $\ell = 3$, (c): $\ell = 5$ and (d): plot of the experimental results for the different values of $|\ell|$ considered. The experimental results were normalised to start at 4/3 like the numerical curves. 103

5.5 Numerical (a) and experimental (b) results of the evolution of the tangle between two qutrits against the scintillation strength for $|\ell| = 1, 3$ and 5. . 104

5.6 (a) Simplified diagram of the experimental setup used to detect the OAM eigenstates after SPDC.(b) Diagram of the setup used to simulate the down-conversion experiment with back projected classical light. One of the APDs is replaced with a diode laser at a wavelength of 710 nm and the BBO crystal with a mirror. 106

5.7 The real part density matrix representing the state of the two qutrits obtained from a full quantum state tomography. (a) theoretical density matrix, (b) density matrix obtain from down-converted photons, (c) density matrix obtain from back-projected classical light. The x and y axis represent the basis vectors 107

5.8 The tangle plotted against the scintillation strength w_0/r_0 for both the down-conversion experiment and the back projection experiment. 108

List of Tables

3.1 Distance scale at which entanglement decays for OAM entangled photons in a beam with $\omega_0 = 10$ cm, a wavelength of $\lambda = 1550$ nm, on a horizontal path in moderate turbulence ($C_n^2 = 10^{-15}$ m$^{-2/3}$). 70
3.2 Parameters used for the plots in Fig. 3.19, 3.20, 3.21 and 3.22 74
3.3 Parameters used for the plots in Fig. 3.23 ($K = 91.6$). 80

5.1 Comparison of the fidelity, the linear entropy and the tangle for the theoretical density matrix and the matrices obtained in down-conversion and back-projection experiments. 107

Symbols and Notation

C_n^2	Refractive-index structure constant [$\mathrm{m}^{-2/3}$]
ℓ	azimuthal mode index
$\hbar$	Planck constant ($6.62606957 \times 10^{-34}\mathrm{J} \cdot \mathrm{s}$)
$J_a(\cdot)$	Bessel function of order a
k	wave-number
k_r	radial wave-number
k_z	longitudinal wave-number
L_0	Outer scale of turbulence
l_0	Inner scale of turbulence
p	radial mode index
r_0	Fried parameter, also known as the atmospheric coherence length
w_0	beam radius at the waist
z_R	Rayleigh range
APD	Avalanche photodiodes

BBO	beta-barium borate
BG	Bessel-Gauss
IPE	Infinitesimal propagation equation
LG	Laguerre-Gauss
MLE	Maximum likelihood estimate
OAM	Orbital angular momentum
S&R	Smith and Raymer
SLM	Spatial light modulator
SPDC	Spontaneous parametric down-conversion

Chapter 1

Introduction

1.1 literature review

1.1.1 The orbital angular moment of light

Even though it was suspected long ago that light has mechanical properties, it was only after Maxwell's unified theory of optics, electricity, and magnetism [1] that a theory quantifying these mechanical properties was possible. Maxwell presented a calculation for the pressure exerted by radiation on the earth's surface in his treatise published in 1891. However, it was Poynting who quantified the momentum and energy flux associated with an electromagnetic field [2]. By using a mechanical anology, Poynting further deduced in 1909 that circularly polarised light must carry an angular momentum [3]. He proposed a method for measuring that angular momentum based on the following argument. Circularly polarised light can be converted into a linearly polarised light by propagating through a series of suspended quarter-wave plates. By doing so, the beam should transfer all of its angular momentum to the wave plates, thereby inducing a torque in the suspension. It was only in 1936 that Beth realised an elegant variation of Poynting's proposed experiment and successfully detected the effect of light's angular momentum [4]. Beth experiment considered only polarisation and therefore the measured angular momentum is the spin angular momentum (SAM) also referred to as the intrinsic angular momentum [5–7]. It can have a value between $\sigma\hbar$ where

$\sigma = +1$ for left-handed circularly polarised light and $\sigma = -1$ for right-handed circularly polarised light.

It was also known long ago that a calculation of light's angular momentum produced contributions which did not depend on polarisation. For instance, it was known that multipolar processes could produce radiation which possesses an angular momentum larger than $\hbar$ [8, 9]. As an example, the interaction of light with atomic or molecular systems may cause an electric quadrupole transition. For that to occur, an angular momentum exchange of $2\hbar$ in the angular momentum of the atomic state is required. This means that the emitted light will carry an angular momentum of $2\hbar$, implying that a photon can carry an angular momentum larger that $\hbar$. The part of the angular momentum not resulting from polarisation became known as orbital angular momentum (OAM) [5]. Darwin was one of the first to attempt to explain the extra momentum in higher-order transitions [10]. He hypothesised that the extra momentum could be carried away by an emitted photon when the centre of mass of the atomic system is slightly displaced from the optical axis.

The current interest in the OAM states of light was sparked by the recognition by Allen *et al.* in 1992 that it was possible to generate laser beams in the laboratory that carry integer multiples of $\hbar$ of OAM per photon [11, 12]. They showed that any light beam with the azimuthal phase dependence $\exp(\mathrm{i}\ell\phi)$ will carry an OAM of $\ell\hbar$ per photon. Such a light beam has a helical phase front with helicity ℓ that can adopt, in principle, any integer value between $-\infty$ and ∞. The OAM can therefore have a value much larger than the SAM which is limited to a value between $-\hbar$ and $\hbar$.

Light beams carrying OAM were initially realised as Laguerre-Gaussian (LG) laser modes [12]. The LG modes were initially produced by transforming Hermite-Gaussian modes into LG modes by means of cylindrical-lens mode converters [12]. Subsequent methods for generating LG modes include the use of spiral phase plates [13], the use of devices called *q-plates* that generate light with OAM by exploiting the SAM-OAM coupling in an inhomogeneous anisotropic medium [14, 15] and forked Holograms [16–18]. The preferred method for generating light with OAM nowadays is the use of forked holograms because of the ease and flexibility of this method. These holograms are now implemented using spatial light modulators (SLMs) which are computer-controlled diffractive devices [19]. The LG beam is not the only beam that carries OAM, there exist other beams that have a helical wave front and can also carry orbital angular momentum. These include Bessel beams [20], Bessel-Gauss beams [21], Mathieu beams [22], and Ince-Gauss beams [23]. However, in this thesis only the LG and Bessel beams will be considered.

Since the publication of the paper by Allen *et al.* in 1992, photonic OAM has been utilised for numerous applications. For instance, to trap and rotate absorbing micro-sized particles [24–27], to produce and drive complex micromachines [28,29], to drive micro-optomechanical pumps for microfluidics [30,31] and for imaging and metrology [32–35]. The OAM states of light have equally been exploited for communication purposes where it was shown that unlike the polarisation degree of freedom, the OAM can be used to encode more than one bit per photon [36–39]. In particular, photonic OAM has been considered for free-space optical communication [40,41].

The OAM states of light found many application in quatum information processing and communication too. Since the concept of OAM applies to single photons as well, photonic OAM represents a multi-level quantum system. The early experiment in quantum information were based on SAM, using the polarisation degree of freedom of photons. However, one can only implement two-dimensional quantum systems (quantum systems described by a two-dimensional Hilbert space) using the polarisation of a photon. The OAM states of the photon on the other hand can be used to implement multidimensional quantum systems [42,43].

1.1.2 Quantum entanglement

For a comprehensive review on quantum entanglement, see Ref. [44] and [45]. Only some salient points are presented here. The word entanglement comes from the translation of the German word “Verschränkung ”coined by Erwin Schödinger to describe a correlation of a quantum nature between two particles that interact and then separate [46]. Initially, quantum entanglement was regarded as a paradoxical and problematic aspect of quantum physics when Einstein, Podolski and Rosen (EPR) pointed it out in 1935 in a thought experiment attempting to show that quantum mechanics was an incomplete theory [47]. Their thought experiment proposed a pure state, now known as an EPR-state, consisting of two subsystems A and B that interacted in the past and whose properties remain correlated even if they have been spatially separated. The EPR-state cannot be written as a product of states of the subsystems A and B. In other words, the subsystem A and B are entangled. Quantum entanglement allows one to predict the properties of subsystem B from a measurement of the properties of subsystem A and vice versa regardless of their spatial separation. EPR concluded that there were two possible explanations: either there was some interaction between the particles, even though they were separated, or the information about the outcome of all possible measurements was already present in both particles. The first explanation implied that information could travel faster than the speed of light and was thus in conflict with the theory of relativity. EPR preferred the second explanation concluding that quantum mechanics was incomplete. According to that explanation, the information was concealed in some "hidden variables." This is what is now known as the EPR-paradox.

Ever since the formulation of the EPR-paradox, entanglement played an important role in the development of quantum theory as it is the main trait that clearly distinguishes quantum mechanics from its classical counter part. For instance, it violated at least one of the classical postulates known as local realism that state that

- objects have properties prior to and independent of measurements (realism) and
- measurement outcomes obtained at one location are independent of actions at another spatial location (locality).

With quantum entanglement these postulates cannot be jointly maintained. It was only in 1964 that the flaw in EPR's argument was discovered by Bell who proved that one of their assumptions (the principle of locality) was inconsistent with the interpretation of quantum mechanics based on hidden variables [48, 49]. Bell specifically demonstrated that entanglement should give rise to correlations stronger than those allowed by any theory obeying local realism between outcomes of measurements. He derived an inequality (now known as "the Bell inequality"), that gives an upper bound for the strength of correlations resulting from a theory obeying local realism and showed that, according to quantum theory, certain entangled states violate this inequality.

The Bell inequality provided a framework for the investigation of quantum entanglement experimentally. But it was only in 1972 that quantum entanglement was first demonstrated experimentally by Freedmann *et al.* [50].

Besides its fundamental role in our understanding of quantum physics, quantum entanglement is nowadays regarded as a resource that allows the implementation of certain tasks that are impossible or very difficult otherwise [51]. Some of these tasks are quantum teleportation [52], quantum computing [53], quantum metrology [54], superdense coding [55] and quantum cryptography [56]. Most of these tasks make use of two-dimensional entangled quantum systems. However, multidimensionally entangled systems have been proved to significantly improve many quantum information tasks. For instance, it has been shown that multidimensional entangled systems provide a higher information capacity [57, 58] and an increased security in quantum cryptography [59, 60]. From a more fundamental viewpoint, closing the detection loophole in Bell test experiments is more feasible with the use of multidimensional entangled systems [43, 61, 62]. Two-photon high-dimensional entanglement has been demonstrated by exploiting the frequency of the optical field [63], the energy-time and time-bin properties [64, 65], or transverse spatial correlation of photons [42, 66–68]. Multidimensional entanglement has also been implemented by combining different degrees of freedom [69–71]. This is known as hyperentanglement

One promising way of implementing multidimensional entangled quantum systems is to use the OAM states of light [42, 43, 72]. A pair of photons entangled in their OAM degree of freedom can be generated through the nonlinear process of spontaneous parametric down conversion (SPDC).

An interesting application of the OAM in quantum information is quantum key distribution (QKD) [56, 73–76]. Quantum key distribution was developed because there was a need for secure means of sharing a private key for *private key cryptosystems* [51]. The security of QKD is based on the fundamental laws of quantum mechanics. In particular, QKD schemes exploit the fact that observing a quantum system disturbs the system. Thus in a perfectly implemented QKD system, the parties sharing the key would know if an eavesdropper tries to get a copy of the key as that would introduce disturbances in the system. Most of the implementations of QKD use the polarisation degree of freedom to encode information. Because the polarisation is limited to only two states, only one bit of information can be impressed onto each photon. But as stated earlier, QKD schemes can be improved with the use of multidimensional quantum systems. One of the biggest challenges that QKD or quantum communication with OAM faces is the distortion-free transmission of OAM-encoded photons over large distances. Most optical fibres in use today are single mode fibres, they can only transport light with zero OAM (the fundamental mode). These fibres cannot be used to transport light with non-zero OAM. A possible solution to this problem is to use free-space information transfer [40, 41]. However, OAM modes suffer distortions due to atmospheric turbulence, which negatively affects the information encoded in the OAM photon states. In order to implement a free-space quantum communication system using photonic OAM, one needs to understand how atmospheric turbulence affects the OAM states of photons.

1.1.3 The effect of atmospheric turbulence on the OAM states of light

There have been many studies addressing the effect of atmospheric turbulence on the OAM states of photons. Paterson studied theoretically the effect of atmospheric turbulence on the OAM of single photons [41]. He used LG modes to derive an expression for the scattering probability of OAM modes. He further calculated the channel capacity and quantified the effect of turbulence on a single-photon, OAM based line-of-sight classical communication system. The expression giving the scattering probability of the OAM modes is an integral that is not easy to solve analytically. In order to solve that integral, Paterson restricted his analysis to the weak turbulence regime. In this regime, intensity fluctuations or scintillation caused by the turbulent atmosphere are sufficiently small that they can be neglected. One can therefore assume that the cumulative effect of the turbulence over the propagation path can be considered as a pure phase perturbation on the beam at the output plane. This will be referred to as the single phase screen approximation in this thesis. Paterson's results show that even weak aberrations have significant effects on the OAM and this poses a considerable problem for communication systems based on OAM. He however concluded that adaptive optics may be of considerable benefit.

Tyler and Boyd also presented an analytical study of the effect of atmospheric turbulence on a vortex beam having the form $A_0 \exp(i\ell\phi)$ [77]. They found that the probability of a photon retaining its initial OAM states after propagating through the atmosphere is given by $\langle s_0 \rangle = [1 + (1.845D/r_0)^2]^{-1/2}$. In the previous expression, D is the aperture diameter and r_0 is the Fried coherence diameter, which is a measure of the transverse distance scale over which refractive index correlations remain correlated [78]. Their study is also limited to the weak fluctuations regime since they also used the single phase screen approximation.

The effect of Kolmogorov turbulence on entangled OAM states of down-converted photons was considered by Gopaul and Andrews [79]. They numerically investigated three cases: first they calculated the probability $P(\ell_0)$ for a single photon to conserve its initial OAM value after it has propagated in turbulence. Next they considered a pair of OAM entangled photons (generated through SPDC) propagating in turbulence and they calculated the probability $P(\ell_1)$ of detecting one photon with ℓ_1 in the signal mode. Then, still considering the down converted photons, they calculated the probability $P(\ell_1, \ell_2)$ of jointly detecting photons with ℓ_1 in the signal mode and ℓ_2 in the idler mode. Their results show that entangled photons are less robust to the effects of Kolmogorov turbulence compared to single photons $[P(\ell_1, \ell_2) < P(\ell)]$ and that signal photons are more robust than single photons $[[P(\ell) < P(\ell_1)]$ when $\ell_0 = \ell = 0$.

The single phase screen approximation has also been used in experimental studies of the effect of turbulence on the OAM states. For instance, Malik *et al.* presented an experimental implementation of a free-space 11-dimensional communication system using OAM modes [80]. They showed that their communication system has a maximum measured OAM channel capacity of 2.12 classical bits/photon. They simulated turbulence with a single Kolmogorov phase screen displayed on a phase-only SLM. They found that the channel capacity is increasingly degraded with increasing turbulence strength and that the effects of turbulence could be mitigated by increasing the spacing between detected OAM modes. Rodenburg *et al.* also used a single Kolmogorov phase screen displayed on a phase-only SLM to study the crosstalk induced by turbulence on OAM channels [81]. They measured the crosstalk in OAM for 11 differents modes (ℓ from -5 to 5) and showed that the purity of the modes within that range is uniformly degraded irrespective of the input mode number. Their results suggest that a system implementing adaptive optics to reduce the effects of turbulence can operate independently of the communications channel.

Other experimental studies not based on the single phase screen approximation include the work by Rodenburg *et al.* where a 1 km thick turbulent medium with atmospheric structure constant $C_n^2 = 1.8 \times 10^{-14}\text{m}^{-2/3}$ was simulated in the lab with two phase screens and the crosstalk in the communication channel is reduced using an adaptive correction of the turbulence as well as optimization of the channel encoding [82]. Pors *et al.* also presented an experimental study of the effect of turbulence on the coincidence detection of two OAM-entangled photons generated by SPDC [83]. They simulated atmospheric turbulence with a turbulent cell where cold and hot air are mixed to bring about random variations of the refractive index. They show that the number of entangled modes (the Shannon dimensionality) decreases with increasing scintillation. They also found that the shape of the coincidence curve is robust under the action of turbulence even though the coincidence counts drop with increasing turbulence. However, none of these experimental studies directly consider the effect of turbulence on the OAM entanglement. This is one of the issues that will be addressed in this thesis.

The evolution of OAM entanglement between two photons have also been considered theoretically. Smith and Raymer studied analytically the evolution of OAM entanglement between two qubits propagating in turbulence [84]. They made use of the single phase screen approximation which limits the validity of their findings to the weak fluctuation regime. They further used the quadratic approximation of the refractive structure function [85, 86]. Their results show that modes with higher OAM value are more robust in turbulence but that photons in such modes scatter more into other modes. In other words, turbulence induced crosstalk affects higher modes more severely.

The single phase screen approximation makes it easy to obtain an analytical expression for the evolution of OAM entanglement in turbulence, but it is limited to the weak fluctuation regime. For a general description of the effect of turbulence on the OAM states of a photon, one needs to go beyond the single phase screen approximation. A method to numerically simulate atmospheric turbulence is the split-step method [87,88] where the atmospheric turbulence is modelled by a series of consecutive phase screens. This method is valid in both the weak and strong fluctuation regimes. Anguita *et al.* used the split-step method to numerically study the effect of turbulence on multichannel free-space optical communication system based on OAM-carrying beams [89]. They found that turbulence induces attenuation and crosstalk among channels. By considering a model in which the constituent channels are binary symmetric and the crosstalk is a Gaussian noise source, they found optimal sets of OAM states at each turbulence condition studied and determined the aggregate capacity of the multichannel system at those conditions. Their results also show that OAM-multiplexed free-space optical systems operating in the weak turbulence regime offer reasonable performance and that the aggregate capacity of the channel decreases as the turbulence increases.

Another analytical work considering the evolution of OAM entanglement in turbulence is the work by Roux where a multiple phase screen approach was used to derive a first-order differential equation describing the evolution of OAM entanglement in turbulence [90]. Because this work is based on a multiple phase screen approach, it is valid in both the weak and strong fluctuation regimes.

1.2 Objectives

This thesis deals with the evolution of OAM entanglement in atmospheric turbulence. Our specific goals are the following:

- Our first goal is to verify the analytical work of Smith and Raymer using numerical simulations. That is, we will present a numerical study of the evolution of OAM entanglement between a pair of qubits evolving in turbulence. We will simulate the turbulent atmosphere with a single phase screen based on the Kolmogorov theory of turbulence. We will used LG modes.
- It has been mentioned earlier that the single phase screen approximation is only valid in the weak fluctuation regime. Our second goal is to go beyond the single phase screen approximation. We will present a numerical study of the evolution of OAM entanglement between two qubits propagating in turbulence. We model the turbulence with a series of consecutive phase screens based on the Kolmogorov theory of turbulence. We will compare our results with those obtained by Smith and Raymer [84] and Roux [90].
- Our third objective is to present the first experimental study, to our knowledge, directly considering the evolution of OAM entanglement in turbulence. We consider qubits represented by photons entangled in their OAM degrees of freedom, and we simulate the turbulent atmosphere with a single phase screen displayed on an SLM.

- Our fourth objective is the study of higher dimensional entanglement in turbulence. More precisely we present a theoretical and experimental study of the evolution of OAM entnalgement between two qutrits. Here we consider paraxial Bessel-Gauss beams.

1.3 Outline of the thesis

This thesis is organised as follows: In Chapter 2 the theoretical background that will be used in the subsequent chapters is introduced. In Chapter 3 we present our numerical scheme and the numerical results of the evolution of OAM entanglement between two qubits in both the weak and the strong fluctuation regimes. Our experimental study of the evolution of OAM entanglement between two qubits is presented in Chapter 4. Chapter 5, is about the evolution of OAM entanglement between two qutrits represented by photons propagating in turbulence. Finally, a summary of this thesis and some suggestions for possible future work are provided in Chapter 6.

Chapter 2

Theoretical background

2.1 Introduction

The aim of this introductory chapter is to review the theoretical background that will be used in the subsequent chapters. This chapter is organised as follows. The concept of the orbital angular momentum of light (OAM) is presented in section 2.2. The photon fields considered in this thesis are assumed to be paraxial, thus subsection 2.2.1 discusses the OAM of light in paraxial optics. Optical beams carrying OAM are introduced in subsection 2.2.2 and methods of generating these beams are discussed in subsection 2.2.3.

The concept of quantum entanglement is discussed in section 2.3 where we also discuss the spontaneous parametric down-conversion process as a means of generating entangled photon pairs (subsection 2.3.1) and the OAM state of light as a means of implementing multidimensional entangled systems (subsection 2.3.2). The concept of quantum state tomography is presented in 2.3.3.

In section 2.4, we introduce the concept of atmospheric turbulence and its effects on a propagating optical wave. A statistical description of the turbulence is presented in subsection 2.4.1 and the power spectra of the refractive-index fluctuations are introduced in subsection 2.4.2. These spectra are derived from the Kolmogorov theory of turbulence. The method that will be used in the following chapters to simulate atmospheric turbulence is then discussed in subsection 2.4.3.

Previous theoretical studies dealing with the evolution of the OAM entanglement in turbulence are presented in subsection 2.4.4.

2.2 The orbital angular momentum of light

The total momentum of the field [5–7]

$$\mathbf{J} = \epsilon_0 \int \mathbf{r} \times [\mathbf{E} \times \mathbf{B}] \, \mathrm{d}^3\mathbf{r} \tag{2.1}$$

can be separated into two components, one which is known as the spin or intrinsic part and the other as the orbital part. To see that, let write the n'th component of the Poynting vector as

$$\begin{aligned} \epsilon_0(\mathbf{E} \times \mathbf{B})_n &= \epsilon_0[\mathbf{E} \times (\nabla \times \mathbf{A})]_n \\ &= \epsilon_0 \sum_i (E_i \nabla_n A_i - E_i \nabla_i A_n) \\ &= \epsilon_0 \sum_i \{E_i \nabla_n A_i - \nabla_i (E_i A_n)\} \,, \end{aligned}$$

where $\mathbf{A}$ is a vector potential ($\mathbf{B} = \nabla \times \mathbf{A}$). To obtain the previous result, we used the identity $\mathbf{A} \times (\mathbf{B} \times \mathbf{C}) = \mathbf{B}(\mathbf{A} \cdot \mathbf{C}) - \mathbf{C}(\mathbf{A} \cdot \mathbf{B})$ and the fact that $\nabla \cdot \mathbf{E} = 0$.

By making use of the of the completely antisymmetric tensor ϵ_{lmn}, one can write the components of the vector product in Eq. (2.1) as

$$\begin{aligned} \epsilon_0[\mathbf{r} \times (\mathbf{E} \times \mathbf{B})]_l &= \epsilon_0 \epsilon_{lmn} r_m (\mathbf{E} \times \mathbf{B})_n \\ &= \epsilon_0 \epsilon_{lmn} \sum_i r_m [E_i \nabla_n A_i - \nabla_i E_i A_n] \\ &= \epsilon_0 \sum_i \{\epsilon_{lmn} r_m E_i \nabla_n A_i - \epsilon_{lmn} \nabla_i r_m E_i A_n + \epsilon_{lmn} (\nabla_i r_m) E_i A_n\} \,, \\ &= \epsilon_0 \sum_i \{\epsilon_{lmn} r_m E_i \nabla_n A_i - \epsilon_{lmn} \nabla_i r_m E_i A_n + \epsilon_{lmn} E_m A_n\} \,, \end{aligned} \tag{2.2}$$

where we have made use of the fact that $\nabla_i r_m = \delta_{im}$ (with δ_{im} being the Kronecker delta). The previous expression can be rewritten as

$$\epsilon_0[\mathbf{r} \times (\mathbf{E} \times \mathbf{B})]_l = \epsilon_0 \sum_i \{E_i [\mathbf{r} \times \nabla]_l A_i - \nabla \cdot \mathbf{E}[\mathbf{r} \times \mathbf{A}]_l + (\mathbf{E} \times \mathbf{A})_l\} \,.$$

Thus, Eq. (2.1) can be rewritten as

$$\mathbf{J} = \epsilon_0 \int \sum_i E_i[\mathbf{r} \times \nabla] A_i \, \mathrm{d}^3\mathbf{r} - \epsilon_0 \int \nabla \cdot \mathbf{E}[\mathbf{r} \times \mathbf{A}] \, \mathrm{d}^3\mathbf{r} + \epsilon_0 \int (\mathbf{E} \times \mathbf{A}) \, \mathrm{d}^3\mathbf{r}. \tag{2.3}$$

The second volume integral can be transformed into a surface integral by making use of the divergence theorem (also known as Guass's theorem or Green's theorem) [7]:

$$\int_{\mathcal{V}} (\nabla \cdot \mathbf{v}) \, \mathrm{d}\tau = \oint_{\mathcal{S}} \mathbf{v} \cdot \mathrm{d}\mathbf{a} \tag{2.4}$$

We then get

$$\mathbf{J} = \epsilon_0 \int \sum_i E_i[\mathbf{r} \times \nabla] A_i \, \mathrm{d}^3\mathbf{r} - \epsilon_0 \oint \mathbf{E}[\mathbf{r} \times \mathbf{A}] \cdot \mathrm{d}\mathbf{s} + \epsilon_0 \int (\mathbf{E} \times \mathbf{A}) \, \mathrm{d}^3\mathbf{r}. \tag{2.5}$$

The surface term can be discarded in the limit of sufficiently large integration volume and for electromagnetic fields that are well localised inside the integration box [5, 91]. Under these conditions, the total angular momentum separates into two parts: the total spin angular momentum (SAM) $\mathbf{J_s}$ and OAM $\mathbf{J_o}$ given by

$$\mathbf{J_s} = \epsilon_0 \int \mathbf{E} \times \mathbf{A} \, \mathrm{d}^3\mathbf{r} \tag{2.6}$$

$$\mathbf{J_o} = \epsilon_0 \int \sum_i E_i(\mathbf{r} \times \nabla) A_i \, \mathrm{d}^3\mathbf{r}. \tag{2.7}$$

Spin and orbital angular momenta have different mechanical effects. For instance, if we take planet earth as an example, the SAM causes the planet to spin about its axis thereby giving rise to the alternation of day and night. The orbital angular momentum on the other hand causes the planet to rotate around the sun, giving rise to the annual cycle. For light, these different effects can be observed by illuminating tiny birefringent particles with light having angular momentum. The SAM causes the particle to rotate on its own axis and the OAM causes it to rotate around the beam axis [26, 92].

2.2.1 Angular momentum in paraxial optics

The paraxial approximation

The paraxial approximation assumes that the propagation distance for an optical wave is much larger than the transverse spreading of the wave [86]. The equation governing the evolution of an optical field over time and space is the wave equation

$$\nabla^2 u - \frac{1}{c^2}\frac{\partial^2 u}{\partial t^2} = 0, \tag{2.8}$$

where c is the speed of light and ∇^2 is the Laplacian which is given in rectangular coordinates by

$$\nabla^2 u = \frac{\partial^2 u}{\partial x^2} + \frac{\partial^2 u}{\partial y^2} + \frac{\partial^2 u}{\partial z^2}. \tag{2.9}$$

The wave equation [Eq. (2.8)] can be simplified by making use of the paraxial approximation as follows. Let us consider a monochromatic wave that originates in the plane at $z = 0$ and propagates along the positive $z-$axis, then we look at the solution of the form $u(\mathbf{r}, t) = U(x, y, z) \exp[i\omega t - ikz]$ where k is the wave number and ω the angular frequency (the two are related through $\omega = kc$). Substituting this in Eq. (2.8), we get

$$\frac{\partial^2 U}{\partial x^2} + \frac{\partial^2 U}{\partial y^2} + \frac{\partial^2 U}{\partial z^2} - 2ik\frac{\partial U}{\partial z} = 0, \tag{2.10}$$

Now if we assume that the transverse spreading of the wave is smaller than the propagation distance, the diffraction effects on the optical wave $U(x, y, z)$ change slowly with the propagation distance and the transverse variations. Hence we can assume that

$$\left|\frac{\partial^2 U}{\partial z^2}\right| \ll \left|2k\frac{\partial U}{\partial z}\right|, \quad \left|\frac{\partial^2 U}{\partial z^2}\right| \ll \left|\frac{\partial^2 U}{\partial x^2}\right|, \quad \left|\frac{\partial^2 U}{\partial z^2}\right| \ll \left|\frac{\partial^2 U}{\partial y^2}\right|. \tag{2.11}$$

Thus the wave equation becomes

$$\frac{\partial^2 U}{\partial x^2} + \frac{\partial^2 U}{\partial y^2} - 2ik\frac{\partial U}{\partial z} = 0. \tag{2.12}$$

Equation (2.12) is known as the *paraxial wave equation*, it is sometimes also referred to as the *parabolic equation* [86].

Angular momentum of paraxial beams

Paraxial beams are beams of light for which the transverse spreading is much smaller than the propagation distance as they propagate. The expression of the angular momentum is simplified in the paraxial regime. To see this, we work in the Lorentz gauge and we consider the vector potential

$$\mathcal{A} = \mathbf{A}e^{i\omega t} \tag{2.13}$$

with

$$\mathbf{A} = (\alpha\hat{\mathbf{x}} + \beta\hat{\mathbf{y}})ue^{-ikz}, \tag{2.14}$$

where $\hat{\mathbf{x}}$ and $\hat{\mathbf{y}}$ are unit vectors in the $x-$ and $y-$ directions respectively, α, and β are complex number satisfying $|\alpha|^2 + |\beta^2| = 1$ and u is the amplitude of the beam.

The electric and magnetic fields are given in terms of the vector potential by

$$\mathcal{E} = -\nabla V - \frac{\partial \mathcal{A}}{\partial t} \tag{2.15}$$

and

$$\mathcal{B} = \boldsymbol{\nabla} \times \mathcal{A}, \tag{2.16}$$

where $\mathbf{V}$ is a scalar potential which is related to the vector potential in the Lorentz gauge through

$$\boldsymbol{\nabla} \cdot \mathbf{A} + \frac{1}{c^2}\frac{\partial V}{\partial t} = 0. \tag{2.17}$$

In the paraxial approximation, the vector potential in Eq.(2.13) leads to the following electric and magnetic fields:

$$\begin{aligned}
\mathbf{E} &= -i\omega\mathbf{A} + \boldsymbol{\nabla}\left(\frac{c^2}{i\omega}\nabla \cdot \mathbf{A}\right) \\
&= \left[-i\omega\alpha u\hat{\mathbf{x}} - i\omega\beta u\hat{\mathbf{y}} + c\left(\alpha\frac{\partial u}{\partial x} + \beta\frac{\partial u}{\partial y}\right)\hat{\mathbf{z}}\right] e^{-ikz}, \qquad (2.18) \\
\mathbf{B} &= \left[i\beta ku\hat{\mathbf{x}} - i\alpha ku\hat{\mathbf{y}} + \left(\beta\frac{\partial u}{\partial x} - \alpha\frac{\partial u}{\partial y}\right)\hat{\mathbf{z}}\right] e^{-ikz}.
\end{aligned}$$

From these fields, one can calculate the time-average of the linear momentum density

$$\begin{aligned}\bar{\mathbf{p}} &= \frac{\epsilon_0}{2}(\mathbf{E}^* \times \mathbf{B} + \mathbf{E} \times \mathbf{B}^*) \\ &= \frac{\epsilon_0}{2}[i\omega(u^*\nabla u - u\nabla u^*) + 2\omega k|u|^2\hat{\mathbf{z}} - \omega\sigma\nabla|u|^2 \times \hat{\mathbf{z}}], \qquad (2.19)\end{aligned}$$

where $\sigma = i(\alpha\beta^* - \alpha^*\beta)$. In cylindrical polar coordinates (ρ, ϕ, z), Eq. (2.19) becomes

$$\bar{\mathbf{p}} = i\omega\frac{\epsilon_0}{2}(u^*\nabla u - u\nabla u^*) + \omega k\epsilon_0|u|^2\mathbf{z} - \omega\sigma\frac{\epsilon_0}{2}\frac{\partial|u|^2}{\partial r}\hat{\phi}. \qquad (2.20)$$

Thus if we consider a circularly polarised beam propagating in the z direction and having an amplitude of the form

$$u(r, \phi, z) = U(r, z)e^{i\ell\phi}, \qquad (2.21)$$

the ϕ and z components of the linear momentum density are [11, 93, 94]

$$\begin{aligned}p_z &= \epsilon_0\omega k|u|^2, \qquad (2.22)\\ p_\phi &= \epsilon_0\left(\frac{\omega\ell}{r}|u|^2 - \frac{1}{2}\omega\sigma\frac{\partial|u|^2}{\partial r}\right). \qquad (2.23)\end{aligned}$$

The component p_z is the linear momentum in the propagation direction, the second term in p_ϕ gives rise to the SAM, where $\sigma = \pm 1$ for left, right-handed circularly polarised light and $-1 < \sigma < 1$ for elliptically polarised light (Note that in the paraxial approximation p_ϕ is much smaller than p_z, i.e. $p_\phi/p_z \ll 1$). The first term in p_ϕ has an ℓ dependence and gives rise to the OAM. Its cross product with $\hat{\mathbf{r}}$ gives the orbital angular momentum density

$$j_{oz} = (r\hat{r}) \times \left(\epsilon_0\frac{\omega\ell}{r}|u|^2\hat{\phi}\right) = \epsilon_0\omega\ell|u|^2\hat{z}. \qquad (2.24)$$

The energy density of the beam is given by

$$w = c\epsilon_0\langle\mathbf{E} \times \mathbf{B}\rangle_z = c\epsilon_0\omega k|u|^2 = \epsilon_0\omega^2|u|^2, \qquad (2.25)$$

and the ratio of the orbital angular momentum density to the energy density is

$$\frac{J_{oz}}{w} = \frac{\epsilon_0\omega\ell|u|^2}{\epsilon_0\omega^2|u|^2} = \frac{\ell}{\omega}. \qquad (2.26)$$

By multiplying both the numerator and the denominator of Eq.(2.26) by $\hbar$, we get $\hbar\ell/\hbar\omega$. This suggests that an OAM of $\hbar\ell$ must be associated with each photon since $\hbar\omega$ is the energy associated with each photon.

2.2.2 Optical beam carrying OAM

It was shown in the previous section that any beam of light with the azimuthal dependence $\exp(i\ell\phi)$ in its amplitude will carry an OAM of $\hbar\ell$ per photon regardless of the radial profile. The most popular physically realisable light beams with this azimuthal dependence are Laguerre-Gaussian beams and Bessel beams [94–96].

Laguerre-Gaussian beams

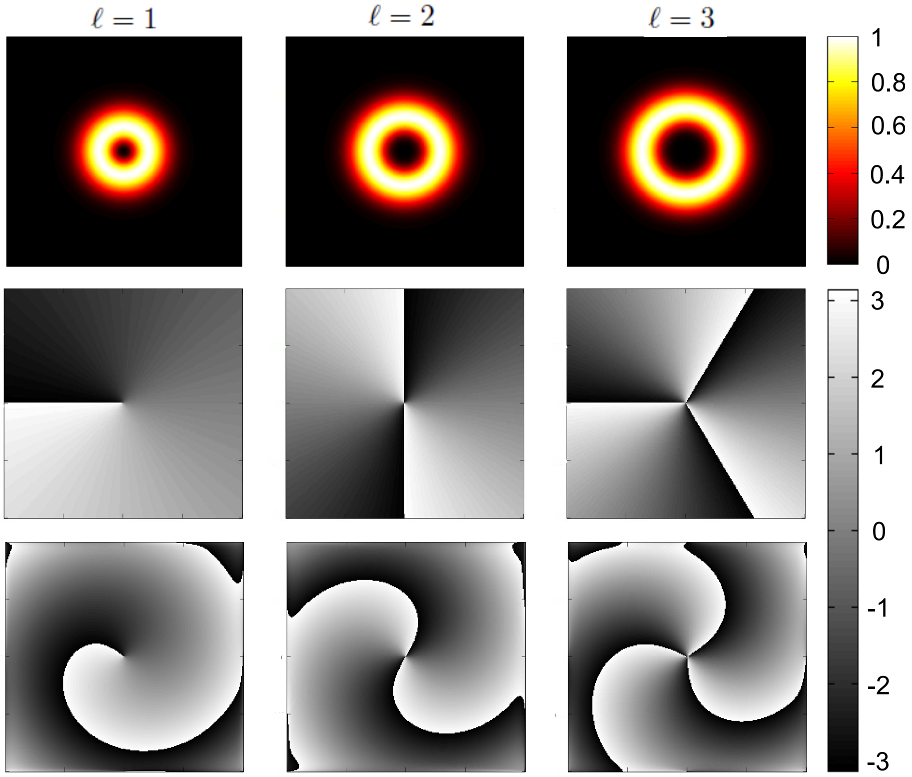

Figure 2.1: Cross section of the intensity profile and phase of a LG beam with radial index $p = 0$. The phase of the beam goes from zero to 2π ℓ-times. When the beam propagates, the phase follows helical trajectory (last row).

Laguerre-Gaussian (LG) modes are solutions of the paraxial wave equation in cylindrical coordinates. The electric field of the LG mode can be represented by

$$\begin{aligned} M_{\ell p}^{\mathrm{LG}}(r,\phi,z) &= \sqrt{\frac{2p!}{\pi(p+|\ell|)!}}\frac{1}{w(z)}\left(\frac{\sqrt{2}r}{w(z)}\right)^{|\ell|} L_p^{|\ell|}\left(\frac{2r^2}{w^2(z)}\right) \\ &\times \exp\left[-\frac{r^2}{w^2(r)}-\frac{ikr^2}{2R(z)}\right] \\ &\times \exp\left[-i(2p+|\ell|+1)\arctan\left(\frac{z}{z_R}\right)\right]\exp(i\ell\phi), \end{aligned}$$

where

$$w(z) = w_0\sqrt{1+\left(\frac{z}{z_R}\right)^2} \tag{2.27}$$

is the width ($1/e^2 - radius$) of the beam as a function of z,

$$R(z) = z\left(1+\frac{z_R^2}{z^2}\right) \tag{2.28}$$

is the radius of curvature of the beam's wavefront and

$$(2p+|\ell|+1)\arctan\left(\frac{z}{z_R}\right) \tag{2.29}$$

is the Gouy phase. The character $L_p^{|\ell|}$ represents the generalized Laguerre polynomials with the parameters ℓ and p being the azimuthal and the radial mode indices, respectively. The beam waist radius is given by w_0, z_R is the Rayleigh range ($= \pi w_0^2/\lambda$) and λ is the wavelength.

Figure 2.1 shows the intensity profile and the phase cross section of the LG mode at a given z for $\ell = 1, 2$ and 3 when the radial index $p = 0$. For these values of p and ℓ, the intensity profile of the beam is a single bright ring that increases in diameter with ℓ. The phase is undefined at the centre of the beam (for beams with non-zero OAM) consequently, the intensity is zero at the centre of the beam. The phase of the beam looks like a screw for $\ell = 1$, and like a double helix when $\ell = 2$. This is clearly illustrated in Fig. 2.2.

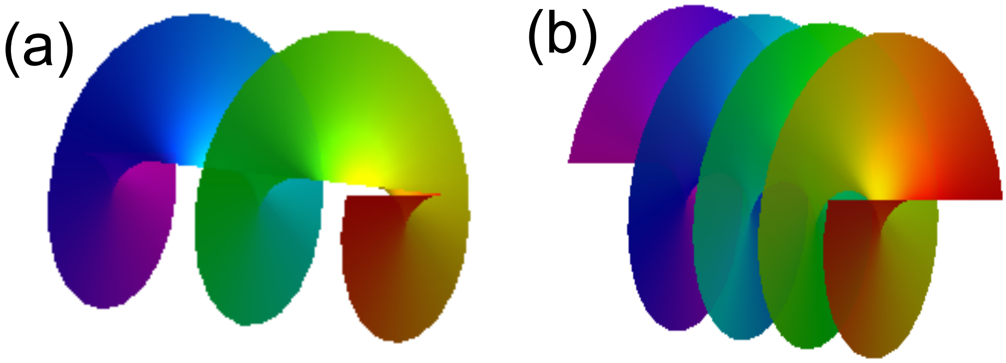

Figure 2.2: The spiral phase of a LG beam. (a) $\ell = 1$ and (b) $\ell = 2$.

Bessel beams

Another solution of the wave equation having the azimuthal dependence $\exp(i\ell\phi)$ are Bessel modes:

$$M_\ell^B(r, \phi, z) = J_\ell(k_r r)\exp(ik_z z)\exp(i\ell\phi), \tag{2.30}$$

where $J_\ell(\cdot)$ is the Bessel function of the first kind, k_r and k_z are the transverse and longitudinal wave numbers respectively. Unlike LG beams, Bessel beams are not well localised at small r values. It should also be noted that the transverse profile of the Bessel beam described by Eq.(2.30) is unbounded. However, practical realizations of Bessel beams always have finite transverse extent.

An example of realisable Bessel beams with finite transverse profile is the paraxial Bessel-Gauss (BG) beam [21] that is described in cylindrical coordinates by

$$M_\ell^{BG}(r, \phi, z; k_r) = \frac{iz_R}{q(z)} J_\ell\left(\frac{iz_R k_r r}{q(z)}\right)\exp\left[-\frac{k_r^2 z_R z}{2kq(z)} - \frac{ikr^2}{2q(z)} - ikz\right]\exp(i\ell\phi), \tag{2.31}$$

where $q(z) = z + iz_R$. The radial profile of the beam can be scaled by choosing different values of k_r as illustrated in Fig. 2.3 where we plot the cross section of the intensity profile and phase of a BG beam for different values of k_r.

An interesting property of Bessel beams is that they do not diffract as they prop-

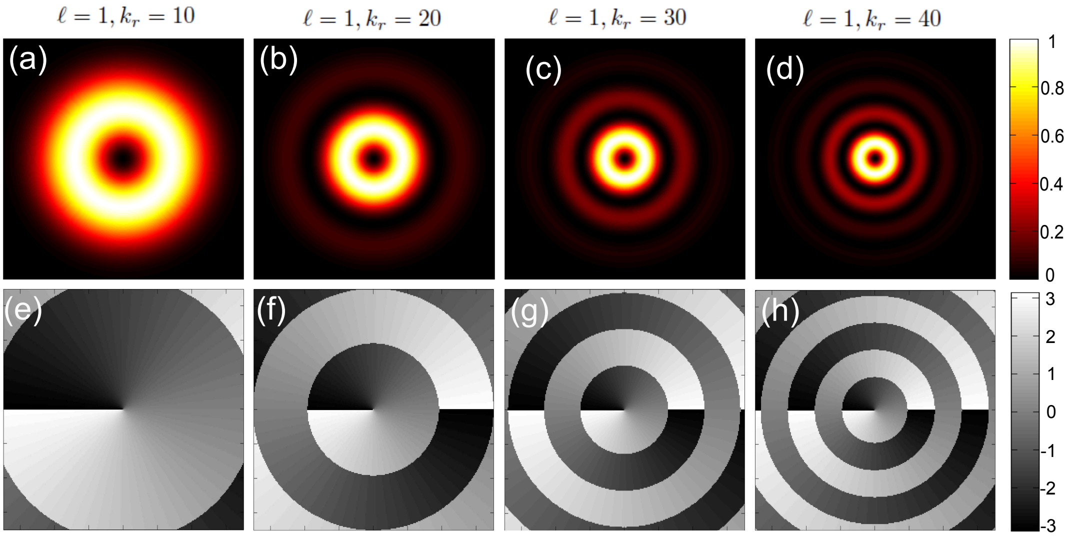

Figure 2.3: The intensity profile and phase of a BG beam for different values of the radial parameter k_r when $\ell = 1$.

agate, but practical Bessel beams are non-diffracting only for a finite propagation length since they always have finite transverse extent [97].

2.2.3 Generation of light beam with OAM

Light beams with OAM were initially generated with the use of cylindrical lenses as mode converters [12]. However, it was later shown that a beam containing a phase singularity described by the $e^{i\ell\phi}$ phase dependence could be generated with the use of a spiral phase plate (SPP) [13]. The SPP is a transparent circular plate with a thickness proportional to the azimuthal angle around its the centre. The SPP resembles one period of a circular staircase and has a phase edge dislocation of hight d as illustrated in Fig. 2.4. The SPP will impart a phase shift

$$\delta\theta = \frac{(n-1)d}{\lambda}\phi \tag{2.32}$$

on a beam with wavelength λ passing through it. In the previous equation, ϕ is the azimuthal angle, n is the refractive index of the SPP and the refractive index of the surrounding medium is assumed to be 1. In order to generate a beam with a well-defined value of OAM like $\ell\hbar$, the total phase around the SPP must be an

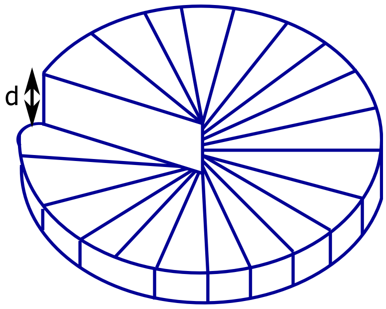

Figure 2.4: Schematic image of a spiral phase plate.

integer multiple of 2π. To achieve such a beam, the physical height of the step in the SPP must be given by

$$d = \frac{\ell\lambda}{(n-1)}. \tag{2.33}$$

Light with OAM can also be generated by exploiting the interaction between SAM and OAM or the SAM-OAM coupling in an inhomogeneous anisotropic medium [14]. Devices called *q-plates* can generate a desired OAM by exploiting a SAM sign-change. Consequently, the handedness of the spiral phase of the beam generated is controlled by the polarization of the initial beam [14, 15].

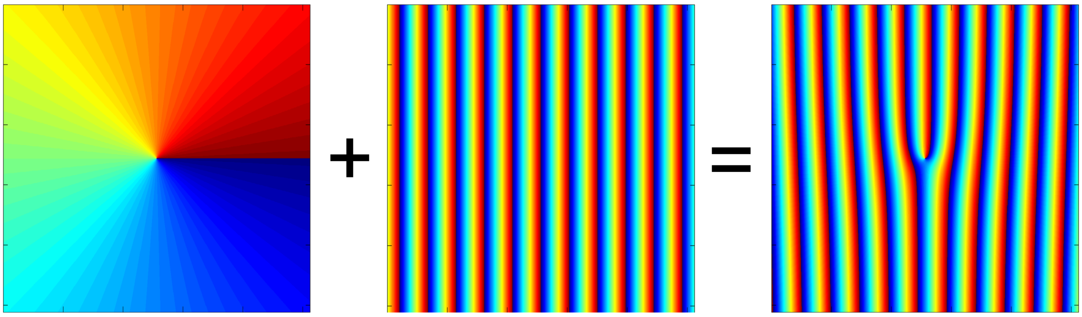

Figure 2.5: Hologram used to generate an LG beam with azimuthal index $\ell = 1$. The hologram is obtained by adding a diffraction grating to a spiral phase.

A more practical way for generating light with OAM is by using diffraction on a fork-like or pitchfork hologram [16–18]. LG beams are nowadays conveniently generated by using "computer generated holograms" obtained by adding a diffraction grating to a spiral phase as illustrated in Fig. 2.5. These holograms can then be displayed on a spatial light modulator (SLM) which are devices having pixellated liquid crystal displays. A LG beam with the desired OAM is then obtained by illuminating an SLM displaying the corresponding fork hologram. This is the method that will be used in the present work.

2.3 Quantum entanglement

All the concepts presented so far in this chapter are purely classical. However, the same concepts also hold in the quantum domain when one considers single photons. It is important to study the OAM state of photons because7, as we will see later, it can be used to implement higher dimensional quantum systems for quantum information tasks. The main resource that is exploited by these tasks is quantum entanglement.

Quantum entanglement is one of the most distinct phenomena in quantum physics. It is associated with non-classical correlations between subsystems of a quantum composite system. A pure state of a composite quantum system is said to be entangled if it cannot be written as a product state, that is, if it cannot be factorised in terms of pure states of each of the subsystems. Otherwise the state is said to be separable. Thus a pure state of a bipartite system consisting of subsystems A and B is entangled if it cannot be factorised as $|a\rangle \otimes |b\rangle$, where $|a\rangle$ and $|b\rangle$ are pure states of subsystems A and B respectively. Consider for example the maximally entangled two-qubits (quantum bits: two-level quantum mechanical systems) state

$$|\Psi\rangle = \frac{1}{\sqrt{2}}\{|0\rangle_A|0\rangle_B + |1\rangle_A|1\rangle_B\}, \tag{2.34}$$

it is not possible to attribute to either subsystem a definite pure state. In other words, $|\Psi\rangle$ cannot be written as $|a\rangle_A \otimes |b\rangle_B$, where $|a\rangle_A$ is a state of the first qubit and $|b\rangle_B$ is a state of the second qubit. The state $|0\rangle_A|0\rangle_B$ on the other hand is separable; it is clear that each of the subsystems is in the state $|0\rangle$.

A mixed state of a bipartite system consisting of subsystems A and B is entangled if it cannot be represented as a mixture of factorisable pure states of the system. That is, if its density matrix cannot be written as [51]

$$\rho = \sum_i p_i \rho_A^i \otimes \rho_B^i, \tag{2.35}$$

where the p_i are probabilities ($0 \leq p_i \leq 1, \sum_i p_i = 1$), ρ_A^i and ρ_B^i are density matrices representing pure states of subsystems A and B, respectively. The state

$$\rho = \frac{1}{2}(|00\rangle\langle 00| + |11\rangle\langle 11|) \tag{2.36}$$

is an example of a mixed separable state of two qubits and the state

$$\rho_W = \frac{1-p}{4}\mathbb{I}_4 + p|\Psi\rangle\langle\Psi| \tag{2.37}$$

is an example of a mixed entangled state of two qubits. The state ρ_W is known as the Werner state, it is a mixture of a maximal entanglement $|\Psi\rangle$ and a completely mixed state represented by the identity operator on the Hilbert space of the two-particles $\mathbb{I}_4$. This Werner state is entangled for $p > 1/3$.

The entangled states that will be considered in this thesis are represented by the OAM state of photons. The method used for generating these OAM-entangled photons is a process called spontaneous parametric down-conversion and it is introduced in the next section.

2.3.1 Spontaneous parametric down-conversion

The early experiments with entangled states employed atomic cascades in calcium to generate the entangled photon pairs [50, 98, 99]. However, In the 1980s and 1990s new sources of correlated photon pairs with higher flux rates were developed by techniques of non-linear optics. The correlated photon pairs were generated by a process known as spontaneous parametric down-conversion (SPDC) in which a single photon from a pump laser at angular frequency ω_p is converted into a pair of signal and idler photons at angular frequencies ω_s and ω_i as illustrated in Fig. 2.6. In this process, an intense pump wave splits into signal and idler waves via the

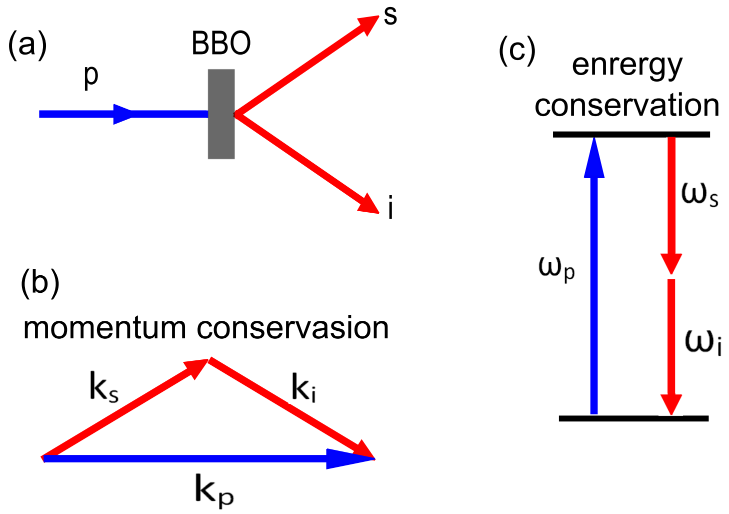

Figure 2.6: Spontaneous parametric down conversion. (a) the non-linear crystal – BBO (Beta Barium Borate) – splits the pump photon into two photons (signal and idler). (b) the combined momentum of the signal and idler photons is equal to the momentum of the pump photon and (c) the combined energy of the signal and idler photons is equal to the energy of the pump photon.

non-linear susceptibility $\chi^{(2)}$ of the medium. The pump photon does not exchange energy with the crystal. Consequently the energy conservation condition is given by

$$\omega_p = \omega_s + \omega_i. \tag{2.38}$$

The process is much more efficient when the wave vectors of the three photons satisfy the conservation of momentum condition given by

$$\vec{k_p} = \vec{k_s} + \vec{k_i}. \tag{2.39}$$

The energy and momentum conservation conditions given above are collectively known as phase-matching conditions. Phase-matching conditions can be satisfied in noncentrosymmetric crystals, since these are the only type of crystals with a nonvanishing $\chi^{(2)}$ [100, 101]. An example of such crystals is the β-barium borate (BBO) crystal.

There are two types of SPDC; type-I and type-II. Type I refers to the situation when the signal and idler photons have the same polarisation, which is orthogonal to the pump polarisation and type-II refers to the situation when the signal and the idler have orthogonal polarisations.

SPDC was first exploited in an experiment in 1988 where it was used to produce polarisation-entangled photons [102]. Since then, SPDC has been the preferred way of generating entangled photons because of the relative simplicity of the process.

2.3.2 OAM and multidimensional entanglement

Entanglement is the main resource used in most quantum information protocols. Most of these protocols exploit two-dimensional entangled systems as multidimensional entanglement is not easy to manipulate and to quantify. However, the use of multidimensional entanglement in quantum information protocols provides many advantages as stated in the previous chapter.

Light with OAM attracted a lot of attention from the quantum information community in the past few years mainly because the OAM state of light can be used to implement multidimensional entangled states.

It was shown in Ref. [103] that the orbital angular momentum is also conserved during SPDC. This is a consequence of momentum conservation. If one assumes that the beams propagate in the same direction after the crystal (collinear geometry) and that the beams are not affected by birefringence as they propagate along one of the principal axes of the crystal, then one can write the state of the generated photons $|\Psi\rangle_{s,i}$ as [104–106]

$$|\Psi\rangle_{s,i} = N_{SPDC} \int d\mathbf{q}_s, d\mathbf{q}_i \exp\left[-A|\mathbf{q}_s - \mathbf{q}_i|^2 - B|\mathbf{q}_s + \mathbf{q}_i|^2\right] |\mathbf{q}_s\rangle|\mathbf{q}_i\rangle, \qquad (2.40)$$

where $|\mathbf{q}_s\rangle, |\mathbf{q}_i\rangle$ represent signal and idler photons respectively, in plane wave modes with transversal momentum $\mathbf{q}_s = (q_s^x, q_s^y)$ and $\mathbf{q}_i = (q_i^x, q_i^y)$,

$$N_{SPDC} = \frac{|AB|^{1/2}}{\pi} \qquad (2.41)$$

is a normalisation constants and A and B are two constants that can be used to tune the momentum correlations among the photons. If one considers the simplest case and takes the centre of the crystal as the origin of coordinates $z = 0$, the constants A and B depend on experimental conditions through

$$A = \frac{w_p^2}{4} \quad \text{and} \quad B = \frac{\alpha L}{4k_p^0}, \tag{2.42}$$

where w_p is the width of the pump beam, L is the length of the crystal, $k_p^0 = \omega_p n_p/c$, with ω_p and n_p being the corresponding angular frequency and refractive index of the pump beam, respectively and α is a fitting constant. The phase-matching condition appears as a sinc function in the state of the two photons. However, that sinc function can be approximated by a Gaussian function as in Eq. (2.40) when $\alpha = 0.455$.

It is useful to write the state of the two photons given by Eq. (2.40) in it's Schmidt decomposition, that is, [107, 108]

$$\Psi(\mathbf{q_i}, \mathbf{q_s}) := \langle \mathbf{q_i}, \mathbf{q_s} | \Psi \rangle_{s,i} = \sum_{a,b} \sqrt{\lambda_{a,b}} u_{a,b}(\mathbf{q_i}) u_{a,b}^*(\mathbf{q_s}) \tag{2.43}$$

where the functions $u_{a,b}$ are the Schmidt modes and depend on the coordinate system employed and the $\lambda_{a,b}$ are the corresponding Schmidt coefficients. In cylindrical coordinates, the Schmidt modes are the LG modes introduced in section 2.2.2. Thus the Schmidt decomposition of $\Psi_{s,i}$ in cylindrical coordinates $[\Psi(\mathbf{q_i}, \mathbf{q_s}) \rightarrow \Psi(\rho_i, \rho_s, \varphi_i, \varphi_s)]$ is given by

$$\Psi_{s,i} = \sum_{\ell=-\infty}^{\infty} \sum_{p=0}^{\infty} (-1)^{|\ell|} (1-z) z^{|\ell|/2+p} LG_p^{\ell}(\rho_i, \varphi_i) LG_p^{-\ell}(\rho_s, \varphi_s) \tag{2.44}$$

with

$$z = \frac{(A-B)^4}{(A^2-B^2)^2}. \tag{2.45}$$

One can thus write the state of the two photons in the LG basis $|\ell, p\rangle$ as

$$|\Psi\rangle_{s,i} = \sum_{\ell=-\infty}^{\infty} \sum_{p=0}^{\infty} c_p^{\ell} |\ell, p\rangle_s | -\ell, p\rangle_i. \tag{2.46}$$

The measurements that will be presented in the subsequent chapters are insensitive to the radial structure of the mode. One can therefore ignore the radial index and write the state of the two photons in a simpler form as

$$|\Psi\rangle_{s,i} = \sum_{\ell=-\infty}^{\infty} c_\ell |\ell\rangle_s |-\ell\rangle_i. \tag{2.47}$$

The OAM state space is theoretically infinite-dimensional, this means that the state in Eq.(2.47) is in principle an infinite-dimensional entangled state. However, only a subset of OAM states can be generated and measured experimentally.

2.3.3 Quantum state tomography

Determining an unknown quantum state ρ is not a trivial exercise. It is in principle impossible to determine the state of an unknown quantum system ρ if one only has a single copy of ρ. This is because there is no quantum measurement which can accurately distinguish non-orthogonal states like $|0\rangle$ and $(|0\rangle + |1\rangle)/\sqrt{2}$ [51]. Quantum state tomography is a procedure that allows one to experimentally estimate the state of an unknown quantum system through repeated measurements on copies of that system [109, 110]. Usually the state to be characterised is produced by an experiment, one can prepare many copies of that state by repeating the experiment. In order to uniquely identify the state, the set of measurements have to be *tomographically complete*, that is, the operators measured have to form an operator basis on the system's Hilbert space so as to provide all the information about the system. Thus any operator – in particular the density operator – can be written as a linear combination of the basis operators with uniquely determined coefficients. For example, the operators $\sigma_0/\sqrt{2}$, $\sigma_1/\sqrt{2}$, $\sigma_2/\sqrt{2}$, $\sigma_3/\sqrt{2}$ form an operator basis for a qubit where σ_0 is the identity matrix and σ_1, σ_2 and σ_3 are the Pauli matrices given by

$$\sigma_0 = \begin{bmatrix} 1 & 0 \\ 0 & 1 \end{bmatrix}, \tag{2.48}$$

$$\sigma_1 = \begin{bmatrix} 0 & 1 \\ 1 & 0 \end{bmatrix}, \tag{2.49}$$

$$\sigma_2 = \begin{bmatrix} 0 & -i \\ i & 0 \end{bmatrix}, \tag{2.50}$$

$$\sigma_3 = \begin{bmatrix} 1 & 0 \\ 0 & -1 \end{bmatrix}. \tag{2.51}$$

The density matrix ρ of a qubit's state can be written in terms of the matrices above as

$$\rho = \frac{\mathrm{tr}(\rho)\sigma_0 + \mathrm{tr}(\sigma_1\rho)\sigma_1 + \mathrm{tr}(\sigma_2\rho)\sigma_2 + \mathrm{tr}(\sigma_3\rho)\sigma_3}{2}. \tag{2.52}$$

Since $\mathrm{tr}(O\rho)$ is the expectation value of the observable O, one can estimate the value of $\mathrm{tr}(O\rho)$ by measuring the observable O a large number of times n and computing the average of the measured quantities. The expectation values of the three observables σ_1, σ_2 and σ_3 can thus be obtained with a high level of confidence in the limit of large sample size. A good estimate of ρ can therefore be obtained provided that one has a large enough sample size.

In order to measure the observables corresponding to the Pauli matrices, one has to perform a projective measurement corresponding to the eigenstates of each matrix. The eigenvalues of all the Pauli matrices are either 1 or -1. Let u_n and v_n be the eigenvectors associated with the eigenvalues 1 and -1 respectively for the Pauli matrix σ_n where $n = 1, 2$ and 3. One can write the Pauli matrix σ_n as the operator

$$\sigma_n = |u_n\rangle\langle u_n| - |v_n\rangle\langle v_n|. \tag{2.53}$$

Then

$$\begin{aligned} \mathrm{tr}\{\sigma_n\rho\} &= \mathrm{tr}\{|u_n\rangle\langle u_n|\rho\} - \mathrm{tr}\{|v_n\rangle\langle v_n|\rho\} \qquad (2.54) \\ &= \langle u_n|\rho|u_n\rangle - \langle v_n|\rho|v_n\rangle. \end{aligned}$$

The quantity $\langle u_n|\rho|u_n\rangle$ can be approximated by measuring the coincidence counts corresponding to the projection operator $|u_n\rangle\langle u_n|$ and normalising the results by dividing by the total count rate (corresponding to $\mathrm{tr}\{\sigma_0\rho\}$), that is,

$$\langle u_n|\rho|u_n\rangle = \frac{\text{count rate for projective measurement}}{\text{total count rate}}. \tag{2.55}$$

The identity operator can be written as

$$\sigma_0 = |u_n\rangle\langle u_n| + |v_n\rangle\langle v_n|. \tag{2.56}$$

Thus

$$\mathrm{tr}\{\sigma_0\rho\} = \langle u_n|\rho|u_n\rangle + \langle v_n|\rho|v_n\rangle. \tag{2.57}$$

Therefore, one can estimate $\mathrm{tr}\{\sigma_n\rho\}$ using the coincidence count rates by

$$\mathrm{tr}\{\sigma_n\rho\} = \frac{\text{count rate for } u_n - \text{count rate for } v_n}{\text{count rate for } u_n + \text{count rate for } v_n}. \tag{2.58}$$

The expansion in Eq. 2.52 can be generalised to the case where one has 2 qubits and to the case of qudits. In the case of 2 qubits, it becomes [51]

$$\rho = \sum_{m,n} \frac{\mathrm{tr}\{\sigma_n \otimes \sigma_m \rho\}\sigma_n \otimes \sigma_m}{4}, \tag{2.59}$$

where n, m are chosen from the set $0, 1, 2, 3$. Each term in Eq. (2.59) can be estimated by measuring observables which are products of Pauli matrices. The tensor product of the Pauli matrices can also be written in terms of the eigenvectors as follows

$$\begin{aligned} \sigma_m \otimes \sigma_n &= (|u_m\rangle\langle u_m| - |v_m\rangle\langle v_m|) \otimes (|u_n\rangle\langle u_n| - |v_n\rangle\langle v_n|) \\ &= |u_m u_n\rangle\langle u_m u_n| - |v_m u_n\rangle\langle v_m u_n| - |u_m v_n\rangle\langle u_m v_n| + |v_m v_n\rangle\langle v_m v_n|. \end{aligned} \tag{2.60}$$

Thus $\mathrm{tr}\{\sigma_m \otimes \sigma_n\rho\}$ can be written as

$$\mathrm{tr}\{\sigma_m \otimes \sigma_n \rho\} = \langle u_m u_n|\rho|u_m u_n\rangle - \langle v_m u_n|\rho|v_m u_n\rangle - \langle u_m v_n|\rho|u_m v_n\rangle + \langle v_m v_n|\rho|v_m v_n\rangle. \tag{2.61}$$

This quantity can be estimated from the coincidence count rate as was done in the case of one qubit above. In the case where $n, m = 1, 2, 3$, one gets

$$\begin{gathered}\mathrm{tr}\{\sigma_n \otimes \sigma_m \rho\} = \\ \frac{\text{count rate for } u_n u_m - \text{count rate for } v_n u_m - \text{count rate for } u_n v_m + \text{count rate for } v_n v_m}{\text{count rate for } u_n u_m + \text{count rate for } v_n u_m + \text{count rate for } u_n v_m + \text{count rate for } v_n v_m}.\end{gathered} \tag{2.62}$$

In the case of a tensor product between a Pauli matrix and the identity matrix, one can write

$$\begin{aligned}\sigma_0 \otimes \sigma_n &= (|u_m\rangle\langle u_m| + |v_m\rangle\langle v_m|) \otimes (|u_n\rangle\langle u_n| - |v_n\rangle\langle v_n|) \\ &= |u_m u_n\rangle\langle u_m u_n| + |v_m u_n\rangle\langle v_m u_n| - |u_m v_n\rangle\langle u_m v_n| - |v_m v_n\rangle\langle v_m v_n|\end{aligned} \tag{2.63}$$

and

$$\begin{aligned}&\mathrm{tr}\{\sigma_0 \otimes \sigma_n \rho\} = \langle u_m u_n|\rho|u_m u_n\rangle + \langle v_m u_n|\rho|v_m u_n\rangle - \langle u_m v_n|\rho|u_m v_n\rangle - \langle v_m v_n|\rho|v_m v_n\rangle \\ &= \frac{\text{count rate for } u_n u_m + \text{count rate for } v_n u_m - \text{count rate for } u_n v_m - \text{count rate for } v_n v_m}{\text{count rate for } u_n u_m + \text{count rate for } v_n u_m + \text{count rate for } u_n v_m + \text{count rate for } v_n v_m}\end{aligned} \tag{2.64}$$

Also,

$$\begin{aligned}\sigma_m \otimes \sigma_0 &= (|u_m\rangle\langle u_m| - |v_m\rangle\langle v_m|) \otimes (|u_n\rangle\langle u_n| + |v_n\rangle\langle v_n|) \\ &= |u_m u_n\rangle\langle u_m u_n| - |v_m u_n\rangle\langle v_m u_n| + |u_m v_n\rangle\langle u_m v_n| - |v_m v_n\rangle\langle v_m v_n|\end{aligned} \tag{2.65}$$

and

$$\begin{aligned}&\mathrm{tr}\{\sigma_m \otimes \sigma_0 \rho\} = \langle u_m u_n|\rho|u_m u_n\rangle - \langle v_m u_n|\rho|v_m u_n\rangle + \langle u_m v_n|\rho|u_m v_n\rangle - \langle v_m v_n|\rho|v_m v_n\rangle \\ &= \frac{\text{count rate for } u_n u_m - \text{count rate for } v_n u_m + \text{count rate for } u_n v_m - \text{count rate for } v_n v_m}{\text{count rate for } u_n u_m + \text{count rate for } v_n u_m + \text{count rate for } u_n v_m + \text{count rate for } v_n v_m}\end{aligned} \tag{2.66}$$

In the case a $d-$dimensional state (*qudits*), one can expand the density matrix of the state in terms of the generalised Gell-Mann matrices τ_i, that is

$$\rho = \frac{1}{d}\sum_{i=0}^{d^2-1} \mathrm{tr}(\tau_i \rho)\tau_i, \tag{2.67}$$

and in the case of n qudits, one can expand ρ in terms of the products of the generalised Gell-Mann matrices as follows

$$\rho = \sum_{m,n} \frac{\mathrm{tr}(\tau_m \otimes \tau_n \rho)\tau_m \otimes \tau_n}{d^2}, \tag{2.68}$$

where now m, n are chosen from the set $0, 1, 2, \cdots d^2 - 1$. For $d = 3$, the Gell-Mann matrices are given by

$$\begin{aligned}
\tau_0 &= \begin{bmatrix} 1 & 0 & 0 \\ 0 & 1 & 0 \\ 0 & 0 & 1 \end{bmatrix}, \quad \tau_1 = \begin{bmatrix} 0 & 1 & 0 \\ 1 & 0 & 0 \\ 0 & 0 & 0 \end{bmatrix}, \quad \tau_2 = \begin{bmatrix} 0 & -i & 0 \\ i & 0 & 0 \\ 0 & 0 & 0 \end{bmatrix}, \\
\tau_3 &= \begin{bmatrix} 1 & 0 & 0 \\ 0 & -1 & 0 \\ 0 & 0 & 0 \end{bmatrix}, \quad \tau_4 = \begin{bmatrix} 0 & 0 & 1 \\ 0 & 0 & 0 \\ 1 & 0 & 0 \end{bmatrix}, \quad \tau_5 = \begin{bmatrix} 0 & 0 & -i \\ 0 & 0 & 0 \\ i & 0 & 0 \end{bmatrix}, \\
\tau_6 &= \frac{1}{\sqrt{3}}\begin{bmatrix} 1 & 0 & 0 \\ 0 & 1 & 0 \\ 0 & 0 & -2 \end{bmatrix}, \quad \tau_7 = \begin{bmatrix} 0 & 0 & 0 \\ 0 & 0 & 1 \\ 0 & 1 & 0 \end{bmatrix}, \quad \tau_8 = \begin{bmatrix} 0 & 0 & 0 \\ 0 & 0 & -i \\ 0 & i & 0 \end{bmatrix}.
\end{aligned} \tag{2.69}$$

The most important drawback of the quantum state tomography is that the reconstructed density matrix often has negative eigenvalues due to experimental imperfections. In the present work, these negative eigenvalues are removed by adding the absolute value of the most negative eigenvalue to the diagonal elements of the reconstructed density matrix and renormalising the results. Furthermore, if the error bars of the resulting eigenvalues, computed from Poisson statistics, still pushed below zero, the mean and standard deviations of these eigenvalues are adjusted so that they remain above zero.

An alternative method of reconstructing the density matrix is the maximum likelihood estimate (MLE) [111]. It is based on the principle that the best estimate of the density matrix is the state that maximises the probability of the measured data $\mathcal{M}$ in the presence of the constraints (for example a positive density matrix). In other words, the best estimate ρ is the state that maximises the likelihood function [111, 112]

$$\mathcal{L}(\rho) \equiv p(\mathcal{M}|\rho). \tag{2.70}$$

The MLE also has a major flaw: if due to experimental imperfection the state reconstructed is not a physically valid state (valid density matrix), the MLE will reconstruct that state as a pure state. For example if we consider qubits and that experimental imperfections lead to a state that lies outside of the Bloch sphere, the MLE will try to reconstruct the closest valid state instead and this is a state that lies on the surface of the Bloch sphere [112].

In fact, it was shown in Ref. [112] that the zero eigenvalues produced by the MLE are related to the negative eigenvalues produced by the the quantum state tomography. That is, for a given dataset, if the quantum state tomography produces a density matrix with negative eigenvalues, then the MLE will produce a density matrix representing a pure state. This can be a problem if one is interested in a non-unitary evolution of the entanglement.

2.4 Optical wave in atmospheric turbulence

Refractive index fluctuations in the atmosphere are a direct consequence of the temperature fluctuations resulting from the turbulent motion of the air due to winds and convection. The earth's atmosphere is a viscous fluid and can be considered to have two different states of motion: laminar flow and turbulent flow. In laminar flow, the velocity characteristics are assumed to be uniform. In turbulent flow, air of different temperatures mixes, so the velocity field is no longer uniform, and it acquires randomly distributed pockets of air, called turbulent eddies . These eddies have varying characteristic sizes and temperatures. Since the refractive index of air depends on temperature, the atmosphere has a random refractive-index profile. Optical turbulence is therefore the fluctuations in the index of refraction resulting from small temperature fluctuation [86].

Even though refractive index fluctuations are small, a propagating optical wave will pass through a series of these fluctuations. The resulting accumulated effect on the wave is quite significant. Examples of these effects include mirage and looming. Mirages occur on hot days when the air closer to earth surface is hotter than that above. This causes a negative temperature gradient that bends the light rays parallel to the earth upward resulting in the shimmering of the horizon. Looming on the other hand occurs at night time when the temperature gradients are positive causing light rays to bend downward. This downward bending of rays allows one to see objects below the horizon. The effects of turbulence on the field in this discussion assumes a scalar approach since the polarization of an optical field does not alter by turbulence in the first order of approximation.

2.4.1 Statistical description of optical turbulence

The earlier classical descriptions of turbulence were dealing with the problem of discovering how random velocity components are generated by laminar flow and how they evolve once they have been created. These velocity fluctuations are given by solutions of the Navier-Stokes equation of hydrodynamics [113]:

$$\frac{\partial}{\partial t} v(r,t) + [v(r,t) \cdot \bigtriangledown]\, v(r,t) = \nu \bigtriangledown^2 v(r,t). \tag{2.71}$$

The Navier-Stokes equation is difficult to solve analytically for fully developed turbulence. Kolmogorov developed a statistical theory of turbulence based on physical insight and dimensional analysis [114]. He suggested that the kinetic energy in large eddies is transferred into smaller eddies as depicted in Fig. 2.7. This is known as the energy cascade theory and it was first introduced by Richardson [86, 115]. Richardson explained that the smaller scale motion in the atmosphere originated as a result of larger ones. A cascade process, in which larger eddies are broken down into smaller ones, continues down to scales in which the kinetic energy is dissipated as heat.

The average size of the largest eddies, L_0, is called the outer scale and the average size of the smallest turbulent eddies, l_0, is called the inner scale. At very small scales (smaller than the inner scale) the energy dissipation caused by friction prevents the turbulence from sustaining itself. The range of eddy sizes between the inner and outer scales is called the inertial sub-range .

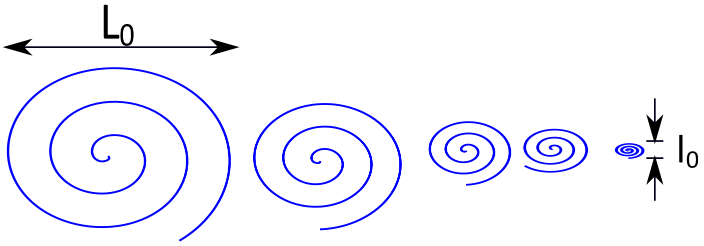

Figure 2.7: The energy cascade theory of turbulence.

Kolmogorov assumed that eddies within the inertial sub-range are statistically homogeneous and isotropic within small regions of space, meaning that properties like velocity and refractive index have stationary increments. This allowed him to use dimensional analysis to determine that the average speed of turbulent eddies v must be proportional to the cubic root of the scale size of eddies [114]. That is,

$$v \propto r^{1/3}. \tag{2.72}$$

He further showed that the structure function of the wind velocity in the inertial sub-range satisfies the 2/3 power law

$$D_v = \langle [v(\mathbf{x_1}) - v(\mathbf{x_2})]^2 \rangle = C_v^2 r^{2/3}, \quad l_0 \leq r \leq L_0, \tag{2.73}$$

where $v(\mathbf{x})$ is the turbulent component of velocity at point $\mathbf{x} = x\hat{x} + y\hat{y} + z\hat{z}$, $r = |\mathbf{x_2} - \mathbf{x_1}|$ is the distance between the two observation points, and C_v^2 is the velocity structure constant (in unit of $\mathrm{m}^{4/3}\mathrm{s}^{-2}$). At small scale size ($r \ll l_0$), the structure function is given by a slightly different relation

$$D_v = C_v^2 l_0^{-4/3} r^2, \quad 0 \leq r \leq l_0. \tag{2.74}$$

There is no general description of the structure function for scale size larger than the outer scale. This is due to the fact that the fluctuations are anisotropic in that limit [86].

Obukov [116] and Corrsin [117] independently extended Kolmogorov's model to statistically isotropic and homogeneous temperature fluctuations. The statistical description of the fluctuations in the atmosphere's refractive index is similar to that of temperature fluctuation since the change in refractive index is directly related to the change in temperature. Obukov [116] further extended the Kolmogorov model to refractive index fluctuations. He obtained the following expression for the structure function for the refractive index fluctuations,

$$D_n(r) = \langle [n(\mathbf{x_1}) - n(\mathbf{x_2})]^2 \rangle = \begin{cases} C_n^2 l_0^{-4/3} r^2 & 0 \leq r \leq l_0, \\ C_n^2 r^{2/3}, & l_0 \leq r \leq L_0, \end{cases} \tag{2.75}$$

where C_n^2 is the index-of-refraction structure constant (in units of $\mathrm{m}^{-2/3}$). The value of C_n^2 near ground typically ranges from 10^{-17} $\mathrm{m}^{-2/3}$ or less for "weak turbulence", up to about 10^{-13} $\mathrm{m}^{-2/3}$ or more for "strong turbulence" [86]. It is reasonable to assume C_n^2 to be constant for short time intervals, fixed propagation distance and constant height above the ground. But that assumption is no longer valid for vertical and slant-path propagation as C_n^2 varies with altitude.

2.4.2 Power spectra for refractive-index fluctuations

It is often necessary to have a spectral description of the refractive-index fluctuations. The effect of the turbulence on an optical wave comes in the form of random phase modulations that are continuously introduced along the propagation path. The random phase imparted on a propagating beam is related to the refractive index fluctuation through

$$\theta(\mathbf{X}) = k_0 \int_0^{\Delta z} \delta n(\mathbf{x}) \, \mathrm{d}z, \tag{2.76}$$

where Δz represents the propagation distance through the turbulence, $\mathbf{x} = x\hat{x} + y\hat{y} + z\hat{z}$ and $\mathbf{X} = x\hat{x} + y\hat{y}$.

One can devise an experiment to obtain the power spectrum of the refractive index fluctuation. For instance, one can measure the phase difference between the output optical fields obtained after two parallel coherent optical beams, separated by a certain distance, are sent through the turbulence as illustrated in Fig. 2.8.

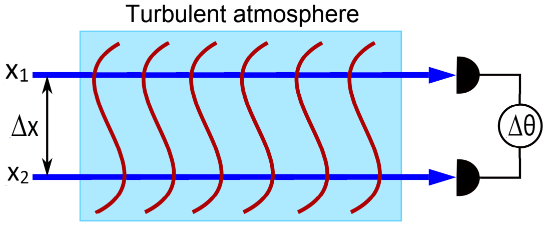

Figure 2.8: A method for measuring the phase differences between two coherent beams propagating in a turbulent atmosphere. The phase difference is measured with an interferometer.

The interference between these two beams, which gives the difference in phase $\Delta\theta$, can then be used to calculate the phase structure function given by

$$\begin{aligned} D_\theta(\mathbf{X}_1 - \mathbf{X}_2) &= \left\langle [(\theta(\mathbf{X}_1) - \theta(\mathbf{X}_2)]^2 \right\rangle \\ &= \left[\langle\theta(\mathbf{X}_1)\rangle^2 + \langle\theta(\mathbf{X}_2)\rangle^2 - 2\langle\theta(\mathbf{X}_1)\theta(\mathbf{X}_2)\rangle \right] \\ &= 2\left[B_\theta(0) - B_\theta(\mathbf{X}_1 - \mathbf{X}_2)\right] . \end{aligned} \tag{2.77}$$

The last expression in Eq. (2.77) relates the phase structure function to the phase autocorrelation function given by

$$B_\theta(\mathbf{X}_1 - \mathbf{X}_2) = \langle\theta(\mathbf{X}_1)\theta(\mathbf{X}_2)\rangle . \tag{2.78}$$

Note that due to the homogeneous statistical properties of the phase functions the phase autocorrelation function only depends on the relative coordinates. In fact, since the phase functions are also isotropic the phase autocorrelation function actually only depends on the magnitude of the relative coordinates. The definition of the phase in Eq. (2.76) ignores an overall constant phase related to the average refractive index, which cancels in the interference and therefore does not contribute to the correlation function. So the phase autocorrelation function becomes

$$B_\theta(\mathbf{X}_1 - \mathbf{X}_2) = k_0^2 \iint\limits_0^{\Delta z} \langle \delta n(\mathbf{x}_1) \delta n(\mathbf{x}_2) \rangle \, \mathrm{d}z_1 \mathrm{d}z_2, \tag{2.79}$$

which gives a relationship between the phase autocorrelation function and the refractive index autocorrelation function.

The refractive index structure function given in Eq. (2.75) is related to the refractive index autocorrelation function by [86]

$$B_n(r) = \langle \delta n(\mathbf{x}_1) \delta n(\mathbf{x}_2) \rangle = B_n(0) - \frac{1}{2} D_n(r). \tag{2.80}$$

According to the Wiener-Khinchin theorem, there exists a Fourier relationship between the autocorrelation function and the power spectral density of a statistical process [86, 118].

$$B_n(\mathbf{x}) = \frac{1}{(2\pi)^3} \iiint_{-\infty}^{\infty} \exp[-i\mathbf{k} \cdot \mathbf{x}] \Phi_n(\mathbf{k}) \mathrm{d}^3\mathbf{k} \tag{2.81}$$

$$\Phi_n(\mathbf{k}) = \iiint_{-\infty}^{\infty} \exp[i\mathbf{k} \cdot \mathbf{x}] B_n(\mathbf{x}) \mathrm{d}^3\mathbf{r} \tag{2.82}$$

For a statistically homogeneous and isotropic atmosphere, the expression giving B_n simplifies to [86]

$$B_n(r) = \int_0^\infty \mathrm{d}k k^2 \Phi_n(k) \int_0^\pi \mathrm{d}\theta \sin\theta \int_0^{2\pi} \mathrm{d}\phi \exp[ikr\cos\phi] \tag{2.83}$$

$$= 4\pi \int_0^\infty k^2 \Phi_n(k) \left(\frac{\sin(kr)}{kr} \right) \mathrm{d}k. \tag{2.84}$$

By combining Eqs. (2.84) and (2.80), one gets

$$D_n(r) = 8\pi \int_0^\infty k^2 \Phi_n(k) \left(1 - \frac{\sin(kr)}{kr} \right) dk. \tag{2.85}$$

The corresponding structure function can be calculated by inverting this integral [113]. To invert this integral, note that

$$\frac{\partial}{\partial r} r^2 \frac{\partial}{\partial r} D_n(r) = 8\pi r \int_0^\infty k^3 \sin(kr) \Phi_n(k) \mathrm{d}k \tag{2.86}$$

then the inverse sine transform gives the corresponding function

$$\Phi_n(k) = \frac{1}{4\pi^2 k^2} \int_0^\infty \mathrm{d}r \left(\frac{\sin(kr)}{kr} \right) \frac{\partial}{\partial r} \left(r^2 \frac{\partial}{\partial r} D_n(r) \right). \tag{2.87}$$

By using $D_n = C_n^2 r^{2/3}$, we obtain

$$\Phi_n(k) = Q C_n^2 k^{-11/3} \tag{2.88}$$

where

$$Q = \frac{5}{18\pi^2} \Gamma\left(\frac{2}{3}\right) \sin\left(\frac{\pi}{3}\right) = 0.033005. \tag{2.89}$$

This is known as the Kolmogorov spectrum and it is only valid over the inertial sub-range ($2\pi/L_0 \ll k \ll 2\pi/l_0$), hence it doesn't take the effects of the inner and outer scales into account.

There are other spectrum models that take the outer and inner scale into consideration. These include the Tatarskii spectrum [119], the von Karman spectrum [87] and the modified von Karman or von Karman Tatarskii spectrum [120]. The Tatarskii spectrum is given by

$$\Phi_n^T(\kappa) = 0.033 C_n^2 \kappa^{-11/3} \exp\left(-\frac{\kappa^2}{\kappa_m^2} \right), \quad \kappa_m = \frac{5.92}{l_0}, \tag{2.90}$$

and it takes into account the inner scale. The von Karman spectrum considers the effect of the outer scale and it is given by

$$\Phi_n^{vK}(\kappa) = 0.033 C_n^2 (\kappa^2 + \kappa_0^2)^{-11/6}, \quad \kappa_0 = \frac{2\pi}{L_0}, \tag{2.91}$$

and the von Karman Tatarskii spectrum

$$\Phi_n^{vKT}(\kappa) = 0.033 C_n^2 (\kappa^2 + \kappa_0^2)^{-11/6} \exp\left(-\frac{\kappa^2}{\kappa_m^2} \right) \tag{2.92}$$

takes into account both the inner and the outer scales.

2.4.3 Simulating atmospheric turbulence: the split-step method

The propagation of light in a source-free medium is given by the Helmholtz equation

$$\nabla^2 E(\mathbf{x}) + n^2 k_0^2 E(\mathbf{x}) = 0, \tag{2.93}$$

where $E(\mathbf{x})$ is the scalar part of the electric field (assuming that the polarization is uniform and can be factored out), k_0 is the wave number in vacuum. In a turbulent atmosphere, the medium, which is represented by the refractive index n, is inhomogeneous. One can represent such a refractive index by

$$n = 1 + \delta n(\mathbf{x}), \tag{2.94}$$

indicating that the average refractive index of air is taken as 1, while the fluctuation is given by $\delta n(\mathbf{x})$.

The fluctuation is very small ($\delta n \ll 1$). As a result one can express the Helmholtz equation as

$$\nabla^2 E(\mathbf{x}) + k_0^2 E(\mathbf{x}) + 2\delta n(\mathbf{x}) k_0^2 E(\mathbf{x}) = 0. \tag{2.95}$$

We also assume that the beam propagates paraxially, which then leads to the paraxial wave equation with the extra inhomogeneous medium term

$$\nabla_T^2 g(\mathbf{x}) - i2k_0 \partial_z g(\mathbf{x}) + 2\delta n(\mathbf{x}) k_0^2 g(\mathbf{x}) = 0, \tag{2.96}$$

where ∇_T is the transverse part of the gradient operator and where, assuming that the paraxial beam propagates in the z-direction, we defined

$$E(\mathbf{x}) = g(\mathbf{x}) \exp(-ik_0 z). \tag{2.97}$$

Thanks to the smallness of $\delta n(\mathbf{x})$ compared to the average refractive index, the modulation by the refractive index fluctuation separates from the free-space propagation in Eq.(2.96). This suggests that one can model the propagation through turbulence by a repeated two-step process that alternates the modulation of the beam by the random phase fluctuation and the propagation of the beam over a short distance through free-space without turbulence.

The numerical technique that is based on this approach is known as the split-step method or the phase screen method [87, 88]. In this method, the atmosphere is represented by a series of phase screens separated by a distance Δz as shown in Fig. 2.9. Each phase screen contains a random phase function that represents a layer of turbulent atmosphere with a thickness of Δz.

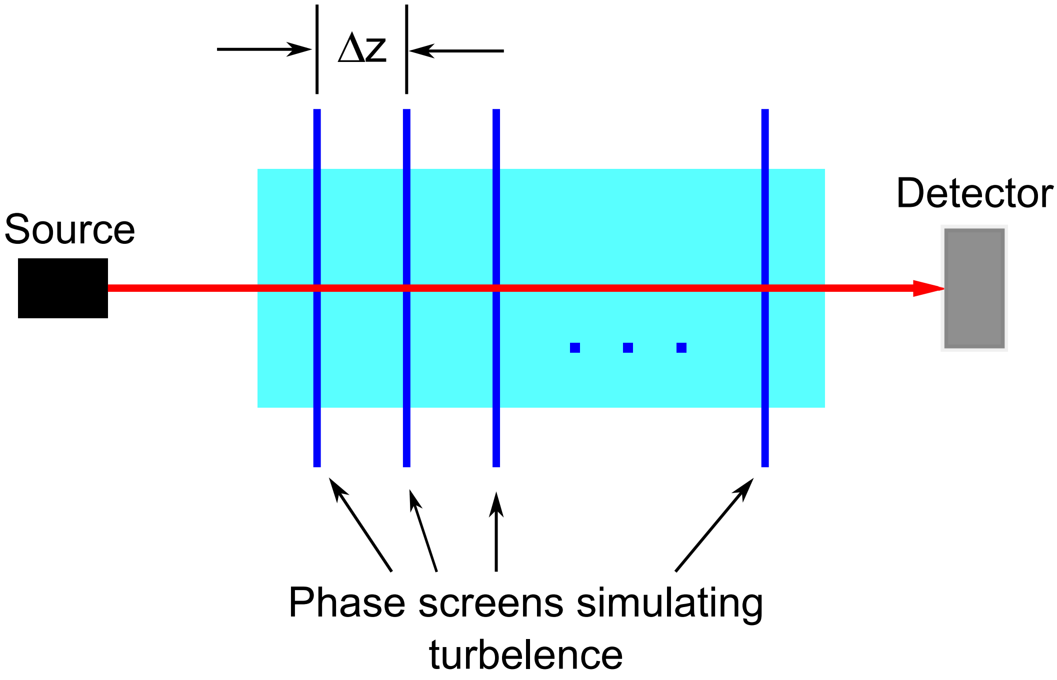

Figure 2.9: Illustration of the split-step method. The turbulent atmosphere is modelled by a series of consecutive phase screens separated by a distance Δz. The phase of the beam is distorted as it goes through a phase screen. After each phase screen, the beam is propagated through the distance Δz where its amplitude is distorted.

Each phase screen imparts a random phase modulation on the phase of the optical beam passing through it. After the phase screen, the beam propagates through free space (without turbulence) over a distance Δz between consecutive phase screens. During that propagation, the phase distortion will induce an amplitude distortion on the beam.

The phase function of the phase screen is expressed in terms of the refractive index fluctuation of the medium through Eq.(2.76). The properties of the random fluctuations of the refractive index are determined by the properties of a turbulent medium. Within the Kolmogorov theory, these properties are given by the power spectral density of the refractive index fluctuations [Eq. (2.82)].

One can use the expression in Eq. (2.82) to infer an expression for the random function of the refractive index fluctuation. Such a random function is conveniently defined as

$$\delta n(\mathbf{x}) = \iiint_{-\infty}^{\infty} \tilde{\chi}(\mathbf{k}) \left[\frac{\Phi_n(\mathbf{k})}{\Delta_k^3}\right]^{1/2} \exp(-i\mathbf{k}\cdot\mathbf{x}) \ \frac{\mathrm{d}^3 k}{(2\pi)^3} \tag{2.98}$$

where $\tilde{\chi}(\mathbf{k})$ is a normally distributed random complex spectral function and Δ_k is its spatial coherence length in the frequency domain. The latter is inversely proportional to the spatial extent of the refractive index fluctuation (typically given by the outer scale of the turbulence). Since the refractive index fluctuation δn is an asymmetric real-valued function $\tilde{\chi}^*(\mathbf{k}) = \tilde{\chi}(-\mathbf{k})$. The autocorrelation function of the random function is given by

$$\langle\tilde{\chi}(\mathbf{k}_1)\tilde{\chi}^*(\mathbf{k}_2)\rangle = (2\pi\Delta_k)^3\delta_3(\mathbf{k}_1-\mathbf{k}_2). \tag{2.99}$$

One can readily verify that Eq. (2.98) is consistent with Eq. (2.82).

Next we substitute Eq. (2.98) into Eq. (2.79). Using Eq. (2.99) to evaluate the ensemble average and evaluating one of the three dimensional Fourier integrals we arrive at

$$\begin{aligned} B_\theta(r) &= k_0^2 \iiint_{-\infty}^{\infty} \Phi_n(\mathbf{k}_1) \iint_0^{\Delta z} \exp(-i\mathbf{k}_1\cdot\mathbf{x}_1) \\ &\quad \times \exp(i\mathbf{k}_1\cdot\mathbf{x}_2) \ \mathrm{d}z_1 \ \mathrm{d}z_2 \ \frac{\mathrm{d}^3 k_1}{(2\pi)^3}, \end{aligned} \tag{2.100}$$

where we used the symmetry of the power spectral density $\Phi_n(-\mathbf{k}) = \Phi_n(\mathbf{k})$.

If we evaluate the two z-integrals we obtain

$$\iint_0^{\Delta z} \exp\left[-ik_z(z_1-z_2)\right] \ \mathrm{d}z_1 \ \mathrm{d}z_2 = \frac{2}{k_z^2}[1-\cos(k_z\Delta z)]. \tag{2.101}$$

Since $\delta n \ll 1$, the effect of the turbulent atmosphere on light propagating through it requires a long propagation distance to become significant. This propagation distance is much longer than the correlation distance of the turbulent medium. Therefore one can assume that Δz is much larger than this correlation distance, which implies that the result in Eq. (2.101) acts like a Dirac delta function. One can therefore substitute $k_z = 0$ in Φ_n in Eq. (2.100) and pull Φ_n out of the k_z-integral. The integral over k_z then gives

$$\int_{-\infty}^{\infty} \frac{2}{k_z^2}[1 - \cos(k_z \Delta z)] \, \mathrm{d}k_z = 2\pi \Delta z. \tag{2.102}$$

The resulting expression for the phase autocorrelation function is then [87, 121]

$$\begin{aligned} B_\theta(\mathbf{X}_1 - \mathbf{X}_2) &= \langle \theta(\mathbf{X}_1)\theta(\mathbf{X}_2) \rangle \\ &= \frac{k_0^2 \Delta z}{2\pi} \iint_{-\infty}^{\infty} \exp[-i\mathbf{K} \cdot (\mathbf{X}_1 - \mathbf{X}_2)] \\ &\quad \times \Phi_n(\mathbf{K}, 0) \, \frac{\mathrm{d}^2 K}{(2\pi)^2}. \end{aligned} \tag{2.103}$$

We now use the expression in Eq. (2.103) to infer an expression for the random phase function, similar to the way we obtained the expression for δn in Eq. (2.98). The expression is

$$\begin{aligned} \theta(\mathbf{X}) &= \frac{k_0}{\Delta_k} \iint_{-\infty}^{\infty} \tilde{\xi}(\mathbf{K}) \left[\frac{dz \Phi_n(\mathbf{K}, 0)}{2\pi} \right]^{1/2} \\ &\quad \times \exp(-i\mathbf{K} \cdot \mathbf{X}) \, \frac{\mathrm{d}^2 K}{(2\pi)^2} \end{aligned} \tag{2.104}$$

where $\tilde{\xi}(\mathbf{K})$ is a two-dimensional normally distributed random complex spectral function such that

$$\langle \tilde{\xi}(\mathbf{K}_1)\tilde{\xi}^*(\mathbf{K}_2) \rangle = (2\pi\Delta_k)^2 \delta_2(\mathbf{K}_1 - \mathbf{K}_2). \tag{2.105}$$

One can now verify that Eq. (2.104) is consistent with Eq. (2.103).

For a real-valued, asymmetric phase function $\tilde{\xi}^*(\mathbf{K}) = \tilde{\xi}(-\mathbf{K})$, however, in the numerical simulation one normally uses a completely asymmetric two-dimensional random complex function $\tilde{\xi}(\mathbf{K})$, which implies that the resulting phase function is complex [87, 121]

$$\theta_1(\mathbf{X}) + i\theta_2(\mathbf{X}) = \frac{k_0}{\Delta_k} \left(\frac{dz}{2\pi} \right)^{1/2} \mathcal{F}^{-1} \left\{ \tilde{\xi}(\mathbf{K}) \Phi_n(\mathbf{K}, 0)^{1/2} \right\}, \tag{2.106}$$

where $\mathcal{F}^{-1}$ represents a two-dimensional inverse Fourier transform. This simply means that with one calculation two random phase functions are generated for two respective phase screens, having transmission functions $t_1 = \exp(i\theta_1)$ and $t_2 = \exp(i\theta_2)$, respectively.

2.4.4 Previous theoretical studies

In the subsequent chapters, the results obtained will be compared with two theoretical studies predicting the evolution of OAM entanglement in atmospheric turbulence: the theory making used of the single phase screen approximation [41] presented by Smith and Raymer in [84] and the infinitesimal propagation equation (IPE) derived in [90]

2.4.5 The single phase screen approximation

The single phase screen approximation assumes that the overall effect of the turbulent medium can be represented by a single phase distortion on the beam followed by a free-space propagation [41] as illustrated in Fig. 2.10.

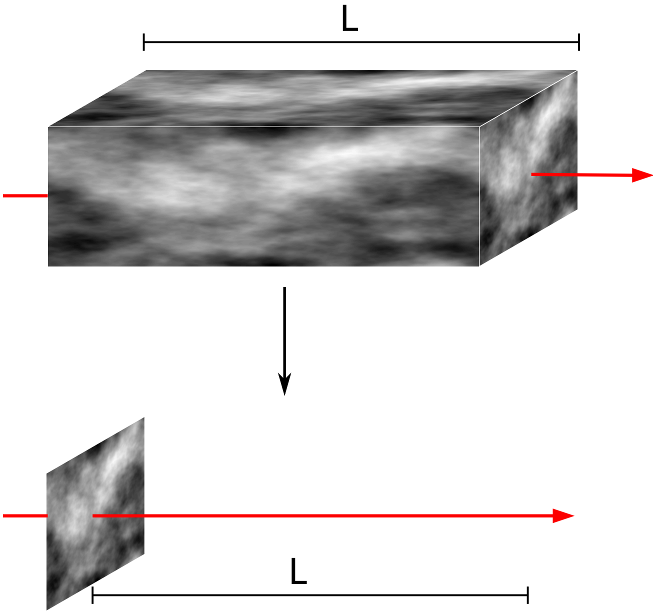

Figure 2.10: Illustration of the single phase screen approximation. A turbulence layer of thickness L is replace with a single phase screen followed by a free-space propagation over the distance L.

If a photon is in the mode $\varphi_\ell(r) = \langle \mathbf{x}|\ell\rangle = R(r)\exp(i\ell\theta)$ initially, and if we assume that the overall effect of the turbulence is a phase distortion [41], then the mode after propagation in turbulence is

$$\Psi(r,\theta) = \langle \mathbf{x}|\ell\rangle^{out} = R(r)\exp(i\ell\theta)\exp[i\phi(r,\theta)]. \tag{2.107}$$

where $R(r)$ is the radial profile of the mode, which we assume is the $p = 0$ LG mode. In what follows higher order ps are neglected. The overlap coefficient a_m^ℓ between the state $|m\rangle$ and the state of the photon $|\ell\rangle$ after it has propagated through turbulence is given by

$$\begin{aligned} a_m^\ell &= \langle m|\ell\rangle^{out} \\ &= \iint R^*(r)\exp(-im\theta)R(r)\exp(i\ell\theta)\exp[i\phi(r,\theta)]r\mathrm{d}r\mathrm{d}\theta \\ &= \iint R^*(r,z)R(r,z)\exp[i(\ell-m)\theta]\exp[i\phi(r,\theta)]r\mathrm{d}r\mathrm{d}\theta. \end{aligned} \tag{2.108}$$

Also, the overlap coefficient a_n^o between the state $|n\rangle$ and the state of the photon $|o\rangle$ after it has propagated through turbulence is given by

$$\begin{aligned} a_n^o &= \langle m|o\rangle^{out} \\ &= \iint R^*(r)\exp(-in\theta)R(r)\exp(io\theta)\exp[i\phi(r,\theta)]r\mathrm{d}r\mathrm{d}\theta \\ &= \iint R^*(r)R(r)\exp[i(o-n)\theta]\exp[i\phi(r,\theta)]r\mathrm{d}r\mathrm{d}\theta. \end{aligned} \tag{2.109}$$

Let considers two qubits that are represented by photons entangled in their OAM mode propagating in turbulence. In order to calculate the elements of the density matrix describing the state of the qubits, one has to calculate the quantity $\langle a_n^{o*}a_m^\ell\rangle$, where $\langle\cdot\rangle$ represents the ensemble average. That quantity is given by

$$\begin{aligned} a_n^{o*}a_m^\ell &= \iint\iint R(r)R^*(r')R^*(r)R(r')\exp[i(\ell-m)\theta-(o-n)\theta'] \\ &\qquad \times\exp[i(\phi(r,\theta)-\phi(r',\theta'))]r\mathrm{d}rr'\mathrm{d}r'\mathrm{d}\theta\mathrm{d}\theta' \end{aligned} \tag{2.110}$$

and

$$\begin{aligned}\langle a_n^{o*} a_m^{\ell} \rangle &= \iint \iint R(r) R^*(r') R^*(r) R(r') \exp[i(\ell - m)\theta - (o - n)\theta'] \\ &\quad \times \langle \exp[i(\phi(r,\theta) - \phi(r',\theta'))] \rangle r \mathrm{d}r r' \mathrm{d}r' \mathrm{d}\theta \mathrm{d}\theta' \qquad (2.111)\end{aligned}$$

where [86]

$$\begin{aligned}\langle \exp[i(\phi(r,\theta) - \phi(r',\theta'))] \rangle &= \exp[-1/2 \langle (\phi(r,\theta) - \phi(r',\theta'))^2 \rangle] \\ &= \exp\left[-\frac{6.88}{2} \left| \frac{\mathbf{r} - \mathbf{r}'}{r_0} \right|^{5/3} \right]. \qquad (2.112)\end{aligned}$$

In order to solve Eq. 2.111, Smith *et al* used of the quadratic approximation of the structure function [85] in the calculation of the phase correlation function. That is, they used $5/3 \approx 2$ in Eq. 2.112. The expression becomes

$$\begin{aligned}\langle \exp[i(\phi(r,\theta) - \phi(r',\theta'))] \rangle &= \exp\left[-\frac{6.88}{2} \frac{|\mathbf{r} - \mathbf{r}'|^2}{r_0^2} \right] \\ &= \exp\left[-\frac{6.88}{2r_0^2} (r^2 + r'^2 - 2rr' \cos(\theta - \theta')) \right]. \qquad (2.113)\end{aligned}$$

By substituting Eq. 2.113 in Eq. 2.111, we get

$$\begin{aligned}\langle a_n^{o*} a_m^{\ell} \rangle &= \iint \iint R(r) R^*(r') R^*(r) R(r') \exp[i(\ell - m)\theta - (o - n)\theta'] \\ &\quad \times \exp\left[-\frac{6.88}{2r_0^2} (r^2 + r'^2 - 2rr' \cos(\theta - \theta')) \right] r \mathrm{d}r r' \mathrm{d}r' \mathrm{d}\theta \mathrm{d}\theta'. \qquad (2.114)\end{aligned}$$

Let $\alpha = \frac{6.88}{2r_0^2}$ and $\theta = \Delta\theta + \theta'$, $\ell - m = \Delta\ell_1$ and $o - n = \Delta\ell_2$. Then

$$\begin{aligned}\langle a_n^{o*} a_m^{\ell} \rangle &= \iint_0^{\infty} \iint_0^{2\pi} R(r) R^*(r') R^*(r) R(r') \mathrm{e}^{i[(\Delta\ell_1 - \Delta\ell_2)\theta' + \Delta\ell_1 \Delta\theta]} \\ &\quad \times \mathrm{e}^{-\alpha(r^2 + r'^2)} \mathrm{e}^{2\alpha r r' \cos\Delta\theta} r \mathrm{d}r r' \mathrm{d}r' \mathrm{d}\Delta\theta \mathrm{d}\theta' \\ &= 2\pi\delta(\Delta\ell_1 - \Delta\ell_2) \iint_0^{\infty} \int_0^{2\pi} R^*(r) R^*(r') R(r) R(r') \\ &\quad \times \mathrm{e}^{-\alpha(r^2 + r'^2)} \mathrm{e}^{\Delta\ell_1 \Delta\theta} \mathrm{e}^{2\alpha r r' \cos\Delta\theta} r \mathrm{d}r r' \mathrm{d}r' \mathrm{d}\Delta\theta. \qquad (2.115)\end{aligned}$$

The delta function in the previous expression implies that this integral is non-zero only when $\Delta\ell_1 = \Delta\ell_2$. Let $\Delta\ell_1 = \Delta\ell_2 = \Delta\ell$. If we make use of the identities:

$$\mathrm{e}^{i\beta cos\phi} = \sum_{n=-\infty}^{\infty} i^n \mathrm{e}^{in\phi} J_n(\beta) \quad \text{and} \quad J_n(ix) = i^n I_n(x), \tag{2.116}$$

we get

$$\mathrm{e}^{2\alpha r r' \cos\Delta\theta} = \sum_{n=-\infty}^{\infty} \mathrm{e}^{-in\Delta\theta} I_n(2\alpha r r'). \tag{2.117}$$

Thus

$$\begin{aligned}\langle a_n^{o*} a_m^{\ell} \rangle &= 2\pi \iint_0^{\infty} R^*(r) R^*(r') R(r) R(r') \mathrm{e}^{-\alpha(r^2+r'^2)} \\ &\quad \times \sum_{n=-\infty}^{\infty} I_n(2\alpha r r') \int_0^{2\pi} \mathrm{e}^{i(\Delta\ell-n)\Delta\theta} \mathrm{d}\Delta\theta r \mathrm{d}r r' \mathrm{d}r'.\end{aligned} \tag{2.118}$$

The $\Delta\theta$ integral is non-zero only when $n = \Delta\ell$ in which case it is equal to 2π. Thus

$$\begin{aligned}\langle a_n^{o*} a_m^{\ell} \rangle &= 4\pi^2 \iint_0^{\infty} R^*(r) R^*(r') R(r) R(r') \\ &\quad \times \mathrm{e}^{-\alpha(r^2+r'^2)} I_{\Delta\ell}(2\alpha r r') r \mathrm{d}r r' \mathrm{d}r'.\end{aligned} \tag{2.119}$$

The radial integrals can now be evaluated by substituting the radial profile of the LG mode.

2.4.6 The IPE

The IPE is a first order differential equation describing the elements of the density matrix representing the state of two photons entangled in the OAM mode as they evolve in turbulence. It was derived by treating the distortion that an OAM state experiences due to propagation through a thin sheet of turbulent atmosphere as an infinitesimal transformation. It is thus based on multiple phase screens. Consequently, it is not limited to the weak fluctuation regime. Consider two photons entangled in the OAM mode propagating in a turbulent atmosphere. Let $\rho(z)$ be the density matrix describing the state of the two photons at a propagation distance z and let dU represent the operator for an infinitesimal propagation through the infinitesimal distance dz in turbulence. Then one can write

$$\rho(z+dz) = dU\rho(z)dU^{\dagger}. \tag{2.120}$$

Because of the randomness of the medium, one has to compute an ensemble average of the density matrix in order to get a meaningful description of the system. Thus

$$\rho(z+dz) = \langle dU\rho(z)dU^{\dagger}\rangle = \frac{1}{N}\sum_{s}^{N} dU_s\rho(z)dU_s^{\dagger} \tag{2.121}$$

where the subscript s represents a particular instance of the turbulent medium. The propagation over a full path z is then performed by repeatedly applying dU. Therefore the operator dU has to take into account the free-space propagation after the phase modulation.

The equation of motion describing a paraxial optical wave propagating in turbulence is given by

$$\nabla_T^2 g(\mathbf{x}) - 2ik_0\partial_z g(\mathbf{x}) + 2k_0^2\delta n(\mathbf{x})g(\mathbf{x}) = 0, \tag{2.122}$$

where $g(\mathbf{x})$ is the scalar electromagnetic field, k_0 is the wave number and $\delta n(\mathbf{x})$ is the refractive index fluctuation. In deriving the previous expression, it was assumed that $\delta n(\mathbf{x}) \ll \langle n\rangle \approx 1$. The statistical properties of the refractive index fluctuation are fully captured by the power spectral density which is a function of the coordinate vector in the Fourier domain. The Fourier transform of Eq. 2.122 is given by

$$-|\mathbf{K}|^2 G(\mathbf{K},z) - 2ik_0\partial_z G(\mathbf{K},z) + 2k_0^2 N(\mathbf{K},z)\star G(\mathbf{K},z) = 0, \tag{2.123}$$

or

$$\partial_z G(\mathbf{K},z) = \frac{i}{2k_0}|\mathbf{K}|^2 G(\mathbf{K},z) - ik_0 N(\mathbf{K},z)\star G(\mathbf{K},z), \tag{2.124}$$

where $\star$ denotes a convolution, $\mathbf{K} = k_x\hat{x} + k_y\hat{y}$ is the two-dimensional transverse Fourier domain coordinate vector, $G(\mathbf{K},z)$ and $N(\mathbf{K},z)$ are the two-dimensional transverse Fourier transforms of the optical field and the refractive index fluctuations respectively. The density matrix representing the state of the two photons can be written in the OAM basis as

$$\rho = \sum_{m,n,p,q} |m\rangle_A |p\rangle_B \rho_{m,n,p,q} \langle n|_A \langle q|_B, \tag{2.125}$$

where $|m\rangle$ and $\langle n|$ are the ket and and bra basis vectors for the photon in path A, and $|p\rangle$ and $\langle q|$ are the ket and and bra basis vectors for the photon in path B. Each of these basis vectors can be written in terms of the momentum basis elements. That is

$$|m\rangle = \int G_m(\mathbf{K}, z)|\mathbf{K}\rangle \frac{\mathrm{d}^2 k}{(2\pi)^2} \tag{2.126}$$

where $|\mathbf{K}\rangle$ represents the two-dimensional momentum basis element and $G_m(\mathbf{K}, z) = \langle \mathbf{K}|m\rangle$. By substituting Eqs.(2.126) and (2.124) into (2.125) and after some algebra, one derives the IPE which is a partial differential equation giving the evolution of the density matrix elements as a function of the propagation distance.

In the case where only one of the two photons propagates in turbulence while the other is left undisturbed, the IPE is given by [90]

$$\begin{aligned} \partial_z \rho_{mnpq} &= i(\mathcal{P}_{mx}\rho_{xnpq} - \rho_{mxpq}\mathcal{P}_{xn} + \mathcal{P}_{px}\rho_{mnxq} - \rho_{mnpx}\mathcal{P}_{xq}) \\ &\quad + \Lambda_{mnxy}\rho_{xypq} - \Lambda_T \rho_{mnpq}, \end{aligned} \tag{2.127}$$

and in the case where both photons propagate through uncorrelated turbulence, it is given by

$$\begin{aligned} \partial_z \rho_{mnpq} &= i(\mathcal{P}_{mx}\rho_{xnpq} - \rho_{mxpq}\mathcal{P}_{xn} + \mathcal{P}_{px}\rho_{mnxq} - \rho_{mnpx}\mathcal{P}_{xq}) \\ &\quad + \Lambda_{mnxy}\rho_{xypq} + \Lambda_{pqxy}\rho_{mnxy} - 2\Lambda_T \rho_{mnpq}. \end{aligned} \tag{2.128}$$

In this expressions,

$$
\begin{aligned}
\mathcal{P}_{mp}(z) &= \frac{1}{2k_0}\int |K|^2 G_m^*(\mathbf{K},z)G_p(\mathbf{K},z)\frac{\mathrm{d}^2k}{(2\pi)^2}, && (2.129)\\
\Lambda_{nmpq} &= k_0^2\int W_{mp}^*(\mathbf{K},z)W_{nq}(\mathbf{K},z)\Phi_0(\mathbf{K},0)\frac{\mathrm{d}^2k}{(2\pi)^2} && (2.130)\\
W_{mn}(\mathbf{K},z) &= \int G_m((\mathbf{K}'+\mathbf{K},z))G_n^*(\mathbf{K}',z)\frac{\mathrm{d}^2k'}{(2\pi)^2} && (2.131)\\
\Lambda_T &= k_0^2\int \Phi_0(\mathbf{K},0)\frac{\mathrm{d}^2k}{(2\pi)^2}. && (2.132)
\end{aligned}
$$

where Φ_0 is the power spectral density of the refractive index fluctuations.

2.5 Summary

In this chapter, the basic concepts that will be used in the following chapters where reviewed. We have discussed the OAM state of light both in the classical and in the quantum regimes. Quantum entanglement and related key concepts were introduced and the non-linear optical process of spontaneous parametric down-conversion, which is a process that produces entangled photon pairs was also discussed. We have also discussed some of the key concepts related to the propagation of optical waves in atmospheric turbulence and we presented some previous theoretical work on the evolution of OAM entanglement in turbulence. In the next two chapters, we present our studies of the evolution of OAM entanglement in turbulence and we compare our results with the previous theoretical studies presented here.

Chapter 3

Numerical simulation of the decay of OAM entanglement in turbulence

3.1 Introduction

In recent years, numerical simulation has become a very important and successful approach for solving complex problems and to gain more insight into scientific phenomena. In this chapter, we present a numerical simulation to study the decay of quantum entanglement between a pair of qubits due to atmospheric turbulence. The qubits are photons entangled in their orbital angular momentum (OAM) mode and the concurrence [122] is used as the entanglement measure. Although some work has in the past been done on the effect of atmospheric turbulence on entangled OAM states [79, 84, 123], the authors assumed that the overall effect of the turbulence over the propagation path can be modelled by a single phase distortion on the beam [41]. This is the single phase screen approximation that was discussed in section 2.4.5. Here, we consider two different cases. In the first case, we use the single phase screen approximation, that is we model the turbulent atmosphere by a single phase screen based on the Kolmogorov theory of turbulence. We then compare our results with those obtained by Smith and Raymer [84] where the single phase screen approximation was used to obtain an analytical expression for the evolution of the OAM entanglement in turbulence. In the second case, we simulate the atmosphere with a series of consecutive phase screens and we compare our results to those obtained by Roux [90] where a multiple phase screen approach was used.

This chapter is organized as follows. In Section 3.2, the numerical method is presented where we describe the simulation process and its validity. The numerical results are presented in Section 3.3 where we first discuss the case where the turbulent atmosphere is modelled by a single phase screen (3.3.1) followed by our discussion of the case where we used the multiple phase screen to simulate turbulence (3.3.2). We end with some conclusions in Section 3.4.

The results presented in this chapter were obtained by the author with input and guidance from Dr. Filippus S. Roux and Prof. Thomas Konrad.

3.2 Numerical simulation

3.2.1 Generating random phase screen

The random phase screens used to simulate the turbulent atmosphere are calculated as described in Section 2.4.3 , and are given by

$$\theta_1(x,y) + \mathrm{i}\theta_2(x,y) = \frac{k_0}{\Delta_k}(2\pi\Delta z)^{1/2}\mathcal{F}^{-1}\left\{\chi(k_x,k_y)\left[\Phi_n(k_x,k_y,0)\right]^{1/2}\right\}, \tag{3.1}$$

where $\mathcal{F}^{-1}$ is the two-dimensional inverse Fourier transform, $\chi(k_x,k_y)$ is a zero-mean normally distributed random complex function and Δ_k is the spacing between samples in the frequency domain. The square root of the power spectral density of the phase function gives the envelope of the Fourier transform of the random phase function on a phase screen. The randomness is added by multiplying this envelope by a normally distributed random complex function with a zero mean $\chi(k_x,k_y)$. The Kolmogorov spectrum of the refractive index fluctuation that was introduced in Section 2.4.2 [Eq.(2.88)] is used. It is repeated here for convenience:

$$\Phi_n(k) = 0.033C_n^2 k^{-11/3} \tag{3.2}$$

where C_n^2 is the refractive-index structure constant. An example of such a phase screen is given in Fig. (3.1).

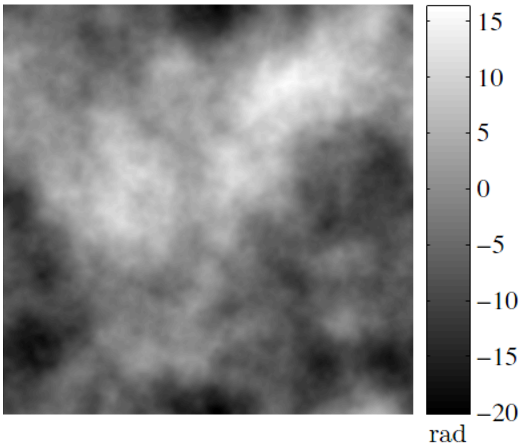

Figure 3.1: A graphical representation of a random phase screen. The phase value is given by the grey scale.

The free-space propagation is done by first computing the angular spectrum $G(k_x, k_y)$, using a two-dimensional Fourier transform of the beam profile at a specific value of z (say $z = 0$)

$$G(k_x, k_y) = \mathcal{F}\left\{g(x, y, 0)\right\}, \tag{3.3}$$

where $\mathcal{F}$ denotes the two-dimensional Fourier transform. Then we multiply the angular spectrum by a phase function that represents the change in phase for each plane wave after propagating a distance Δz. Finally, the beam is reconstructed at $z = \Delta z$ by taking the inverse Fourier transform

$$g(x, y, \Delta z) = \mathcal{F}^{-1}\{G(k_x, k_y) \exp[-\mathrm{i}\Delta z k_z(k_x, k_y)]\}, \tag{3.4}$$

where $k_z(k_x, k_y) = \left(k_0^2 - k_x^2 - k_y^2\right)^{1/2}$.

3.2.2 Accuracy of the phase screens

One can ask the following question: does the phase screen generated as described above truly simulate atmospheric turbulence? A series of tests can be performed to answer that question. The first test we perform is the calculation of the structure function of the phase screens.

The structure function of the phase screens

One way to check if the phase screens simulate the turbulent atmosphere accurately is to calculate the structure function for a sample of these phase screens and compare it to the analytical expression of the phase structure function. For a plane wave source in Kolmogorov turbulence, the phase structure function in the inertial sub-range is given by [86, 113, 124]

$$D_\phi(r) = 6.88 \left(\frac{r}{r_0}\right)^{5/3}, \tag{3.5}$$

where r_0 is the Fried parameter given in Eq. (3.21) [78], which is a measure of the atmospheric coherence length. Figure 3.2 shows a slice of the phase structure function calculated from a 100 phase screens obtained from Eq. 3.1. It is clear from the figure that the calculated phase screens do not have the same statistics as the turbulent atmosphere specially at large r values, which correspond to low spatial frequencies. To understand why this is the case, it should be noted that the power spectrum given in Eq.(3.2) is a spike centred around the origin of the

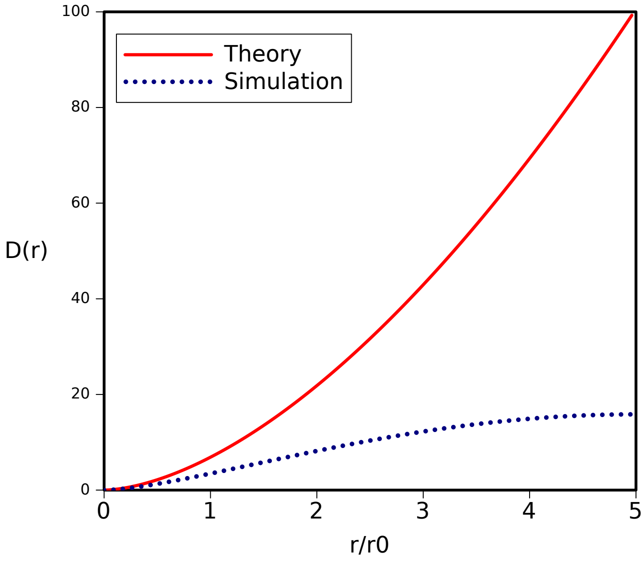

Figure 3.2: A comparison of the structure function of the phase screens with the analytical expression of the structure function.

spatial frequencies (almost like a Dirac delta function) as depicted in Fig. 3.3.

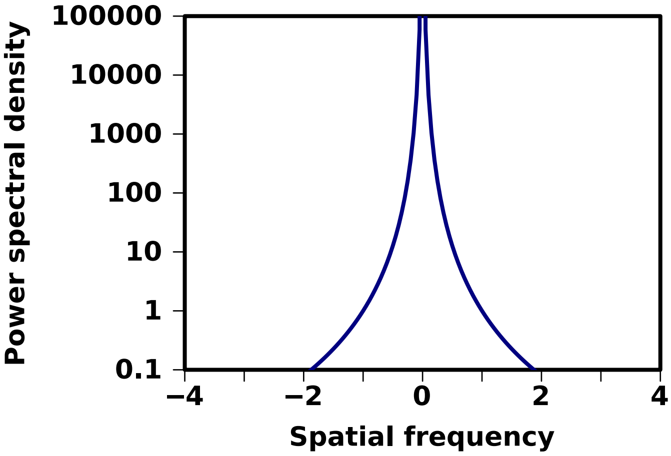

Figure 3.3: The shape of the two dimensional Kolmogorov power spectral density with $C_n^2 = 10^{-15}$.

This means that most of the power is in the low frequencies. The calculated phase screens do not have the correct statistics because these low frequencies were not sampled well enough. Several solutions to this problem have been proposed in the literature, the solution that will be used here is the "addition of sub-harmonic samples" proposed by Lane *et al* in Ref. [125].

The addition of sub-harmonic samples consists of generating additional random frequencies around the origin, as shown in Fig. 3.4, and adding the effects of these low frequencies to the simple sampled frequencies. For the first sub-harmonics samples, the (0,0) point in the frequency space is replaced by 9 points [the (0,0) point and 8 additional points around it]. For the second sub-harmonic samples, the (0, 0) of the first sub-harmonic sample is replace by an additional 9 points. This process is repeated until the desired statistics are obtained. The phase corresponding to the sub-harmonics is given by

$$\theta_{SH}(x,y) = \sum_{p=1}^{N_p} \sum_{n=-1}^{1} \sum_{m=-1}^{1} \chi(k_{x_{n,p}}, k_{y_{m,p}}) \sqrt{\Phi(k_{x_{n,p}}, k_{x_{m,p}})} \exp[\mathrm{i}(k_{x_{n,p}} x + k_{y_{m,p}} y)], \tag{3.6}$$

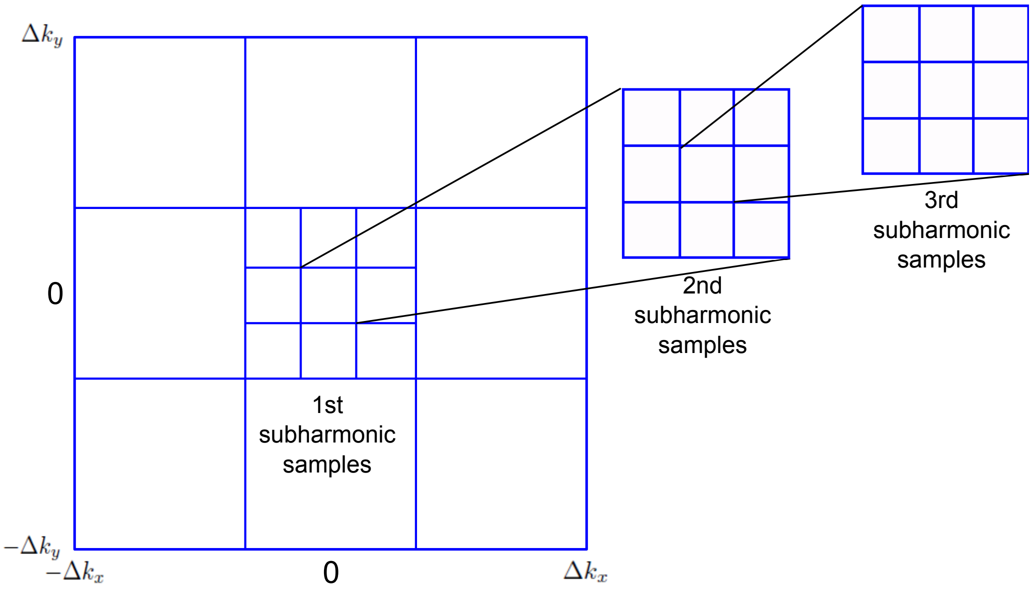

Figure 3.4: The addition of sub-harmonic samples.

where p corresponds to different levels of sub-harmonics. Figure 3.5 shows the structure function of the phase screen with different degrees of sub-harmonics. It is clear that the more sub-harmonics we add, the more low frequencies we sample. As a result, the calculated phase screen represents the statistics of the turbulent atmosphere more accurately.

Unfortunately, adding more sub-harmonics also slows down the simulation process. However, it was observed that phase screens calculated with the third sub-harmonics were good enough for the simulations that will be considered here. This is because results obtained with the third sub-harmonics were similar to those obtained with higher-order of sub-harmonics

The scintillation index

Another cross check one can do is to calculate the scintillation index for a Gaussian beam propagating through simulated turbulence and compare it with its analytical expression. The scintillation index is the normalised variance of the intensity

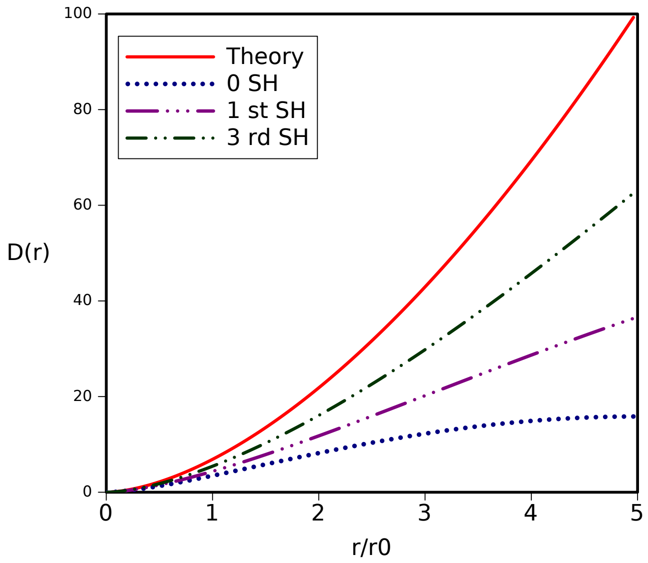

Figure 3.5: A comparison of the structure function of the phase screens with the analytical expression of the structure function. As we add the sub-harmonics, the structure function of the phase screens approaches the analytical expression.

fluctuation. It is defined as [86]

$$\sigma_I^2 = \frac{\langle I^2 \rangle - \langle I \rangle^2}{\langle I \rangle^2}. \tag{3.7}$$

The longitudinal component of the scintillation index of a collimated beam is given on page 356 of Ref. [86].

In this work, we will model the turbulent atmosphere in two different ways. We will first simulate the atmosphere with a single phase screen, this is known as the “single phase screen approximation” [see section 2.4.5]. It assumes that the overall effect of the turbulent medium on the propagating beam is a phase distortion only. This approximation is usually made when simulating weak turbulence. However, as stated in the previous chapters, the single phase screen approximation is only valid in weak scintillation. To have a better model of the turbulent atmosphere, we will use a multiple phase screen approach. That is, we model the turbulent atmosphere with a series of consecutive phase screens as described in section 2.4.3.

It is also important to distinguish between the weak and strong fluctuation

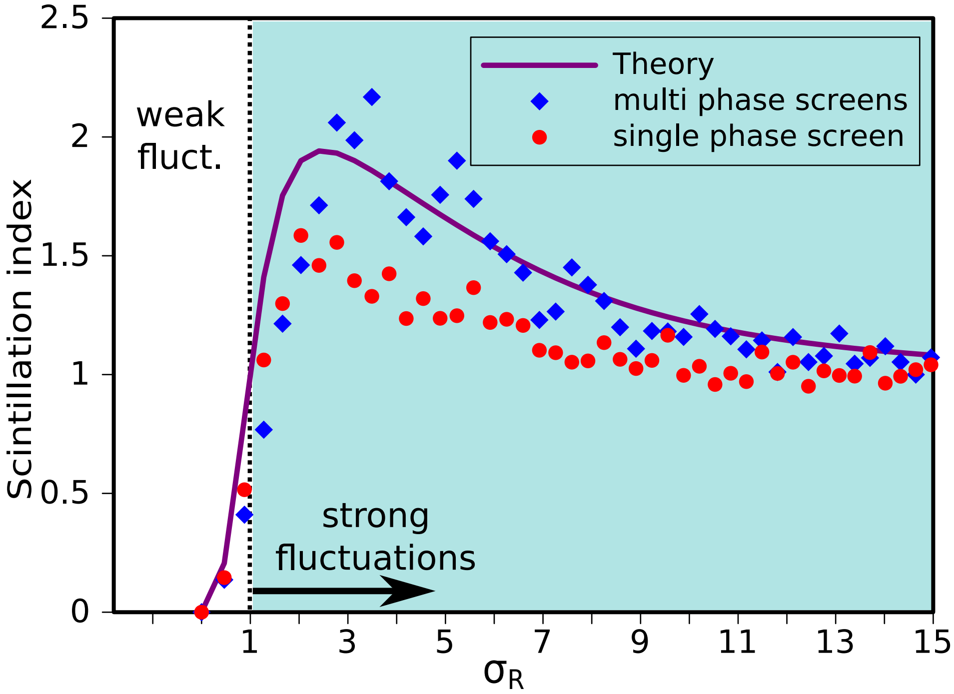

Figure 3.6: The scintillation index against the square root of the Rytov variance $\sigma_R^2 = 1.23C_n^2k^{7/6}z^{11/6}$.

regimes. These are characterised by the Rytov variance given by

$$\sigma_R^2 = 1.23C_n^2k^{7/6}z^{11/6}. \tag{3.8}$$

For plane waves, strong scintillation is said to exist when $\sigma_R^2 > 1$ [86] and for Gaussian beams it exists when $\sigma_R^2 > (t + 1/t)^{5/6}$ [126], where $t = z/z_R$ is the normalised propagation distance with $z_R = \pi w_0^2/\lambda$ being the Rayleigh range.

Figure 3.6 shows the plot of the scintillation index. The curve of the scintillation index obtained with single phase screen approximation agrees well with the theoretical curve in the weak fluctuations regime but deviates from it in the strong fluctuation regime. This supports the fact that the single phase screen approximation is only valid in the weak fluctuation regime. In the strong fluctuation regime, the scintillation index calculated from the multiple phase screens agrees better with the theory.

3.2.3 Decoherence process

The simulated system is shown in Fig 3.7, where the source produces a pair of photons that are entangled in terms of the OAM basis. This is achieved through spontaneous parametric down-conversion (SPDC) as discussed in Section 2.3.1. The two photons then both propagate through turbulent media, after which they are analysed in detectors. The detectors perform a state tomography (see section 2.3.3) to determine the density matrix of the quantum state after the propagation through turbulence.

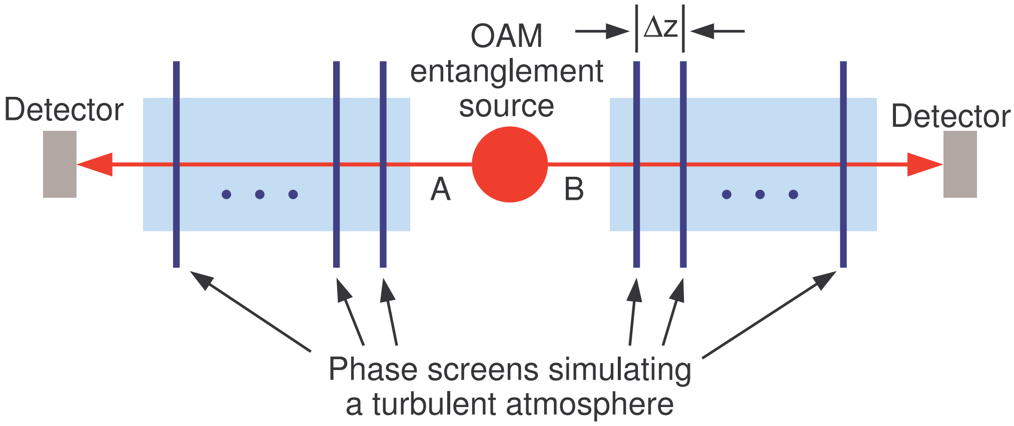

Figure 3.7: The source generates two photons that are entangled in OAM. Each photon is then sent through a turbulent atmosphere (modelled by a series of phase screens) toward a detector.

The initial state that the source in Fig. 3.7 generates is assumed to be the Bell state

$$|\Psi\rangle = \frac{1}{\sqrt{2}} \left(|\ell\rangle_A |-\ell\rangle_B + |-\ell\rangle_A |\ell\rangle_B \right). \tag{3.9}$$

The subscripts A and B are used to label the two different paths of the two photons through turbulence.

When a photon with a given OAM mode propagates through turbulence, the distortions cause the photon to become a superposition of many OAM modes. In other words, any particular OAM state of the photon is scattered into a multitude of OAM states. This can be seen in Fig. 3.8, where we plot the probability of measuring the different modes after a Gaussian beam (with $\ell = 0$) propagates for 10 km in strong turbulence ($C_n^2 = 10^{-13}\text{m}^{-2/3}$).

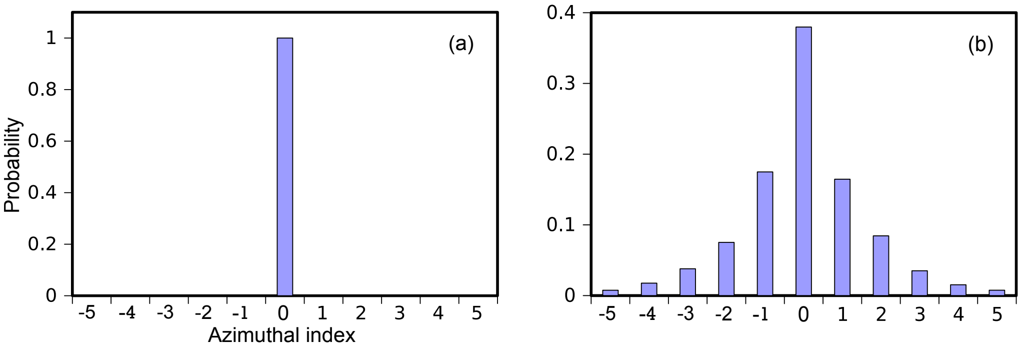

Figure 3.8: The scattering of OAM mode in atmospheric turbulence when a Gaussian beam ($\ell = 0$) propagates for 10 km in strong turbulence ($C_n^2 = 10^{-13}\text{m}^{-2/3}$). Before propagation, only the mode with $\ell = 0$ is present (a). After propagation, the initial mode is scattered into neighbouring modes (b).

We only considered qubits in the results that will be presented in this chapter from this point on. Therefore, when we compute any density matrix, we extract only the information contained in the modes with ℓ and $-\ell$. Hence, we exclude all other modes in the expression of the density matrix.

The state of photon A or B changes as follows after propagating over a distance of Δz through turbulence:

$$\begin{aligned}|\ell\rangle_A &\rightarrow a_\ell|\ell\rangle_A + a_{-\ell}|-\ell\rangle_A \\ |-\ell\rangle_A &\rightarrow b_\ell|\ell\rangle_A + b_{-\ell}|-\ell\rangle_A \\ |\ell\rangle_B &\rightarrow c_\ell|\ell\rangle_B + c_{-\ell}|-\ell\rangle_B \\ |-\ell\rangle_B &\rightarrow d_\ell|\ell\rangle_B + d_{-\ell}|-\ell\rangle_B, \end{aligned} \tag{3.10}$$

where a_ℓ, $a_{-\ell}$, etc. are the complex coefficients in the expansion of the distorted state in terms of the OAM basis. In other words, $a_\ell = \langle\ell|_A U_{\Delta z}|\ell\rangle_A$, $a_{-\ell} = \langle-\ell|_A U_{\Delta z}|\ell\rangle_A$, and so forth where the unitary operator $U_{\Delta z}$ represents propagation through turbulence over a distance of Δz. That is, one can express the distorted state after propagation by $|\Psi'\rangle = U_{\Delta z}|\Psi\rangle$.

After propagating through turbulence, the initial state in Eq. (3.9) will be transformed into

$$\begin{aligned} |\Psi\rangle \to |\Psi\rangle^{out} &= C_1|\ell\rangle_A|\ell\rangle_B + C_2|\ell\rangle_A|-\ell\rangle_B \\ &\quad + C_3|-\ell\rangle_A|\ell\rangle_B + C_4|-\ell\rangle_A|-\ell\rangle_B, \end{aligned} \tag{3.11}$$

where

$$\begin{aligned} C_1 &= \frac{1}{\sqrt{2}}\left(a_\ell d_\ell + b_\ell c_\ell\right), \\ C_2 &= \frac{1}{\sqrt{2}}\left(a_\ell d_{-\ell} + b_\ell c_{-\ell}\right), \\ C_3 &= \frac{1}{\sqrt{2}}\left(a_{-\ell} d_\ell + b_{-\ell} c_\ell\right), \\ C_4 &= \frac{1}{\sqrt{2}}\left(a_{-\ell} d_{-\ell} + b_{-\ell} c_{-\ell}\right). \end{aligned} \tag{3.12}$$

Note that, since only a restricted set of basis elements are retained, the transformation in Eq. (3.11) is not unitary ($|\Psi\rangle^{out} \neq U_{\Delta z}|\Psi\rangle$). The transformed state after the propagation $|\Psi\rangle^{out}$ is however still a pure state, since it is obtained for a specific instance of the turbulent medium (or, in the case of the numerical simulation, for specific phase functions on the phase screens). Because we do not have detailed knowledge of the medium, one needs to compute the ensemble average of the density matrix over all possible (or a representative set of) instances of the medium (or of the phase functions). The resulting density matrix is that of a mixed state. This mixture can be seen as the result of 'tracing over the environment.' The mean density matrix is then given by

$$\rho = \frac{\sum_n^N |\Psi_n\rangle\langle\Psi_n|}{\mathrm{Tr}\left\{\sum_n^N |\Psi_n\rangle\langle\Psi_n|\right\}}, \tag{3.13}$$

where $|\Psi_n\rangle$ is the state of the qubit after the photons propagate through the n^{th} phase screen (the n^{th} realization of the turbulent medium).

The concurrence, which is used as a measure of entanglement [122], is given by

$$C(\rho) = \max\{0, \sqrt{\lambda_1} - \sqrt{\lambda_2} - \sqrt{\lambda_3} - \sqrt{\lambda_4}\}, \tag{3.14}$$

where λ_i are the eigenvalues, in decreasing order, of the Hermitian matrix

$$R = \rho(\sigma_y \otimes \sigma_y)\rho^*(\sigma_y \otimes \sigma_y), \tag{3.15}$$

with * representing the complex conjugate and σ_y being the Pauli y-matrix

$$\sigma_y = \begin{bmatrix} 0 & -\mathrm{i} \\ \mathrm{i} & 0 \end{bmatrix}. \tag{3.16}$$

To simulate the propagation of an entangled quantum state one needs to propagate each of the separate components that make up the state. For the Bell state in Eq. (3.9), this implies two optical fields for each of the propagation paths. Hence, four propagation simulations for each run. The four input optical fields are produced as 256 × 256 arrays of samples of the complex function that represents the mode in the input plane of the system. The complex function for the modes are given in Eq. (2.27), where we set $\ell = \pm q$, $p = 0$ and $z = 0$. We consider the different cases where $q = 1, 3, 5$ and 7. In the simulation, we first multiply the optical fields with the transmission function representing the random phase computed in Eq. (2.106). Then the resulting fields are propagated through free-space over a distance of Δz.

After each free-space propagation step the density matrix of the resulting quantum states is determined by extracting the coefficients of the different modes from the four fields at that point and combining these coefficients into the expression for the states according to Eq. (3.11).

One such run gives a sequence of pure states that represents the evolution of the quantum state of the pair of photons as it propagated through a specific simulated turbulent atmosphere. We performed a number ($N = 1000$) of such runs for N different simulated turbulent atmospheres to obtain N different evolutions of the quantum state. These N runs are used to perform ensemble averaging for each of the elements in the evolution sequence, as expressed in Eq. (3.13), to obtain a sequence of density matrices that represent the evolution of the bi-photon state from an initial pure state to the mixed quantum state that one would observe at a particular point along the propagation path.

3.2.4 Validity of the simulation

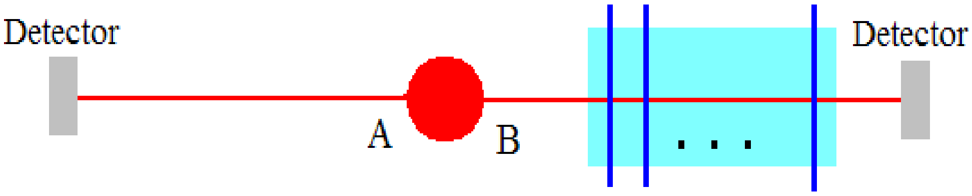

Figure 3.9: The single channel $I \otimes \$$ in Eq. 3.17. Two photons are generated and only one of the two photons propagates in turbulence.

We validate our simulation scheme with the formula derived by Konrad *et al.* [127] stating that the entanglement reduction under a one-sided noisy channel is independent of the initial state and completely determined by the channel's action on a maximally entangled state. More explicitly,

$$\mathcal{C}\left[(I \otimes \$)|\chi\rangle\langle\chi|\right] = \mathcal{C}\left[(I \otimes \$)|\Psi\rangle\langle\Psi|\right]\mathcal{C}(|\chi\rangle), \tag{3.17}$$

where $|\Psi\rangle$ is a Bell state like in Eq. (3.9), $I \otimes \$$ is a one sided noisy channel, χ is a partially entangled pure state and $\mathcal{C}$ represents the concurrence [122] which is an entanglement measure. The one sided channel in our case corresponds to propagating only one of the two photons through turbulence as illustrated in Fig 3.9.

The two sides of Eq. (3.17) are compared in Fig. 3.10 where we plot the evolution

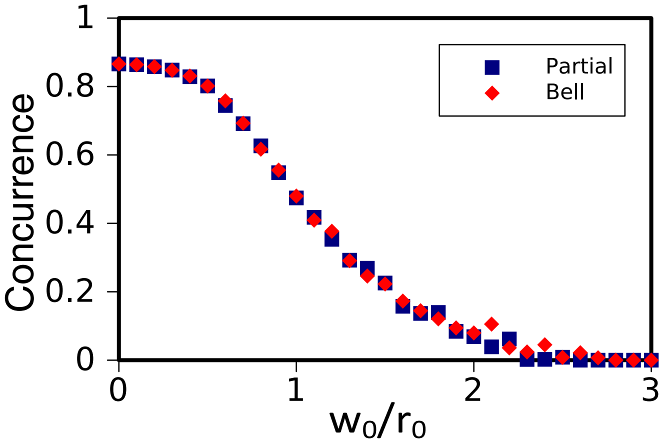

Figure 3.10: Plot of the concurrences $C\left[(I\otimes\$)|\chi\rangle\langle\chi|\right]$ (partial) and $C\left[(I\otimes\$)|\Psi\rangle\langle\Psi|\right]C(|\chi\rangle)$ (Bell) against the scintillation strength.

of the entanglement of a partially entangled pure state

$$|\chi\rangle=\frac{1}{2}|\ell\rangle_A|-\ell\rangle_B+\sqrt{\frac{3}{4}}|-\ell\rangle_A|\ell\rangle_B, \tag{3.18}$$

and the entanglement of the Bell state (multiplied by the initial entanglement of $|\chi\rangle$), both evolving in the single sided channel in Fig. 3.9. It is clear that the entanglement of the Bell state multiplied by the initial entanglement of the $|\chi\rangle$ is consistent with the entanglement of the $|\chi\rangle$ as it evolved through the one sided channel.

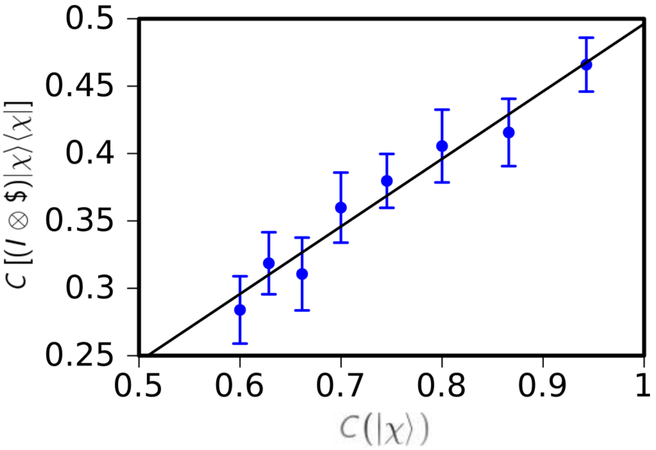

Figure 3.11: $C\,[(I\otimes\$)|\chi\rangle\langle\chi|]$ against $C|\chi\rangle$ for 8 different initial states. Each initial state was averaged over 500 realisations of the turbulent medium. The error bars represent the dispersion of each run from the mean. The solid line is the best fitted line through the points.

Furthermore, if one chooses a fixed propagation distance, and measures the entanglement of a number of partially entangled pure states after they propagate in the single sided channel, one will find that the measured entanglement is linearly related to the initial entanglement. This is shown in Fig. 3.11 where $C\,[(I\otimes\$)|\chi\rangle\langle\chi|]$ is plotted against $C|\chi\rangle$ for 8 different initial states

$$|\chi\rangle_n = \sqrt{\frac{1}{n}}|q\rangle_A|\bar{q}\rangle_B + \sqrt{1-\frac{1}{n}}|\bar{q}\rangle_A|q\rangle_B, \tag{3.19}$$

for $n = 3, 4, 5, \cdots 10$. Each initial state was averaged over 500 realisations of the turbulent medium.

Based on the results presented so far, one can conclude that it is reasonable to use the numerical scheme presented to study the evolution of OAM entanglement in the atmosphere. The results obtained are presented in the following section.

3.3 Results

3.3.1 OAM entanglement through turbulence simulated by a single phase screen

Smith and Raymer (S&R) [84] analytically calculated the curves for the evolution of OAM entanglement between two qubits in turbulence. Their result is based on the Paterson model [41], using the single phase screen approximation as discussed in section 2.4.5. In order to compare our results with theirs, we simulate the atmospheric turbulence with a single phase screen in this section. We further consider two scenarios: in the first, only one of the photons is propagated through turbulence while the other is left undisturbed; on in the second both photons are propagated through turbulence.

Figure 3.12 shows the plots of the concurrence against the scintillation strength for both the numerical simulation and the S&R theory and for $|\ell|-$values 1,3,5 and 7 when one of the photons propagates in turbulence. Figure 3.13 shows the same plots for the case where both photons propagate through turbulence. The scintillation strength is represented by

$$\frac{w_0}{r_0} = 5.4054 w_0 \left(\frac{C_n^2 z}{\lambda^2} \right)^{3/5}, \tag{3.20}$$

where

$$r_0 = 0.185 \left(\frac{\lambda^2}{C_n^2 z} \right)^{3/5} \tag{3.21}$$

is the Fried parameter [78]. The quantity w_0/r_0 depends on both the propagation distance z and the refractive-index structure constant C_n^2 which is a measure of the strength of the refractive-index inhomogeneities. It is thus a measure of the scintillation strength.

The numerical results are consistent with the S&R theory. However, as the value of $|\ell|$ increases, the numerical results deviate slightly from the S&R theory. This is more visible in the case where both photons propagate through turbulence. This might be due to the fact that the S&R theory makes use of the quadratic approximation of the structure function [85] in the calculation of the phase correlation

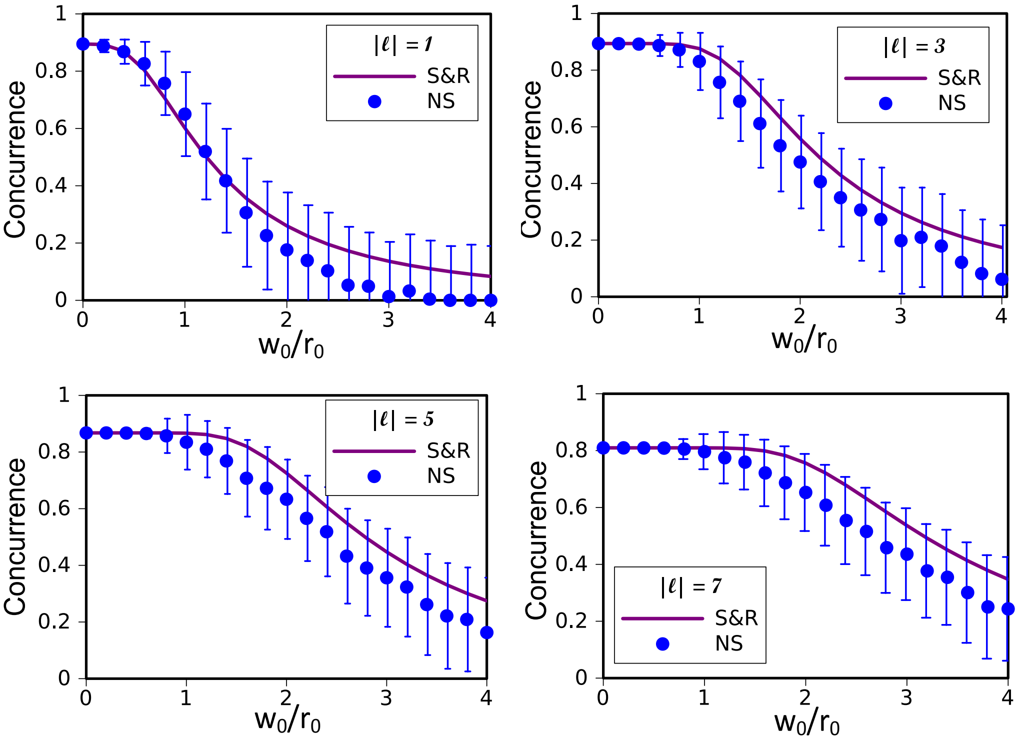

Figure 3.12: The concurrence plotted against the scintillation strength (w_0/r_0) when one of the two photons propagates in turbulence. In (a) $|\ell| = 1$, in (b) $|\ell| = 3$, in (c) $|\ell| = 5$ and in (d) $|\ell| = 7$. In the legend, S&R: theoretical curve derived by Smith and Raymer in [84] and NS: Numerical data points. The error bars are calculated as discussed in appendix A.

function (see section 2.4.5). In other words, instead of using Eq. 3.5 as the phase structure function, they used

$$D_\phi^{quad} = \left(\frac{r}{r_0}\right)^2 . \tag{3.22}$$

This approximation simplifies the calculations, but it tends to over-estimate the concurrence as the value of $|\ell|$ increases.

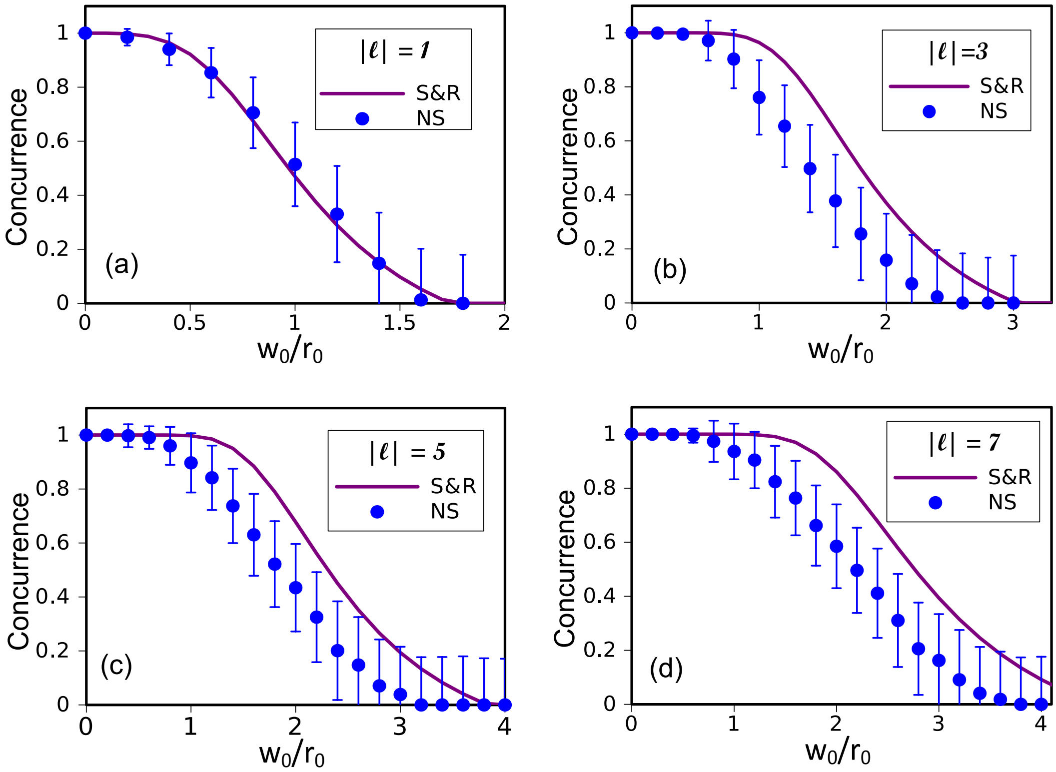

Figure 3.13: The concurrence plotted against the scintillation strength (w_0/r_0) when both photons propagate through turbulence. In (a) $|\ell| = 1$, in (b) $|\ell| = 3$, in (c) $|\ell| = 5$ and in (d) $|\ell| = 7$. In the legend, S&R: theoretical curve derived by Smith and Raymer in [84] and NS: Numerical data points.

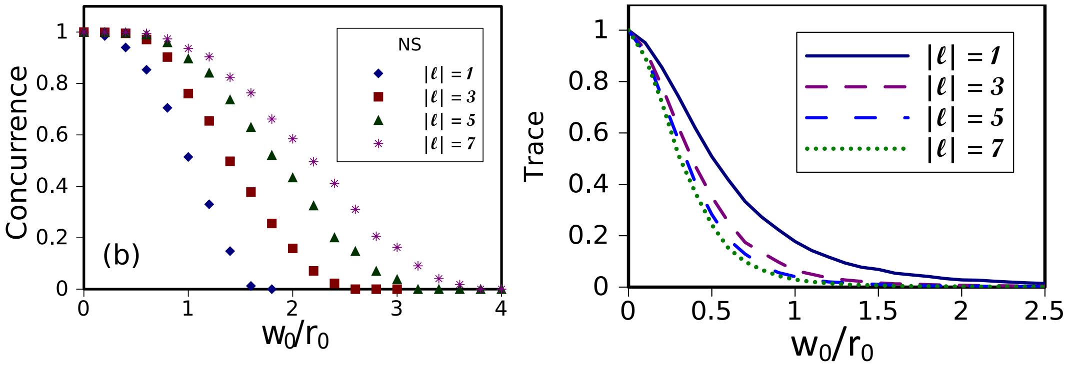

Figure 3.14: The concurrence (a) and the trace of the density matrix before normalisation (b) plotted against the scintillation strength (w_0/r_0) for different values of ℓ when both photons propagate in turbulence.

We observe in Fig. 3.12 and 3.13 that both the S&R theory and the numerical results predict that the concurrence takes longer to decay for higher values of $|\ell|$. This is more clearly seen in Fig. 3.14 (a) where we plot the curves corresponding to the different values of $|\ell|$ on the same graph. This suggests that modes with higher $|\ell|$-values are more robust in turbulence and could thus give an advantage in a free-space quantum communication system. On the other hand, the plots of the trace [Fig. 3.14 (b)] show that the trace decays to zero quicker for higher $|\ell|$-values. This suggests that for higher $|\ell|$-values the scattering into other modes happens more rapidly. The same behaviour was observed in [84, 90].

Scale at which entanglement decays

The S&R theory predicts that the concurrence lasts longer for higher values of $|\ell|$, and that the spacing between adjacent curves decreases as $|\ell|$ increases. This is also true for the numerical simulation and can be seen in Fig. 3.15 where we plot the S&R theory and the numerical results against the scintillation strength on a logarithmic scale. The fact that the concurrence survives longer for higher $|\ell|$-values suggests that the scale of entanglement decay will occur around a different point for larger values of ℓ: the scale at which decoherence occurs depends on the value of ℓ.

To find that ℓ dependence, we use the S&R theory to locate the values of ω_0/r_0 where the concurrence is equal to 0.5 for the different $|\ell|$-values considered. The result obtained is shown in Fig. 3.16 where the ω_0/r_0 values are plotted against the corresponding values of ℓ on a logarithmic scale.

We find $\omega_0/r_0 = 1.35\sqrt{\ell}$ in the single photon case and $\omega_0/r_0 = 1.03\sqrt{\ell}$ in the two photon case. Thus in both cases the entanglement decay happens within an order of magnitude around the point where $\omega_0/r_0 \approx \sqrt{\ell}$. By using the expression of the Fried parameter [Eq.(3.21)], we find that the distance scale at which OAM entanglement decays as a function of ℓ is

$$L_{\mathrm{dec}}(\ell) \approx \frac{0.06\lambda^2\ell^{5/6}}{\omega_0^{5/3}C_n^2}. \tag{3.23}$$

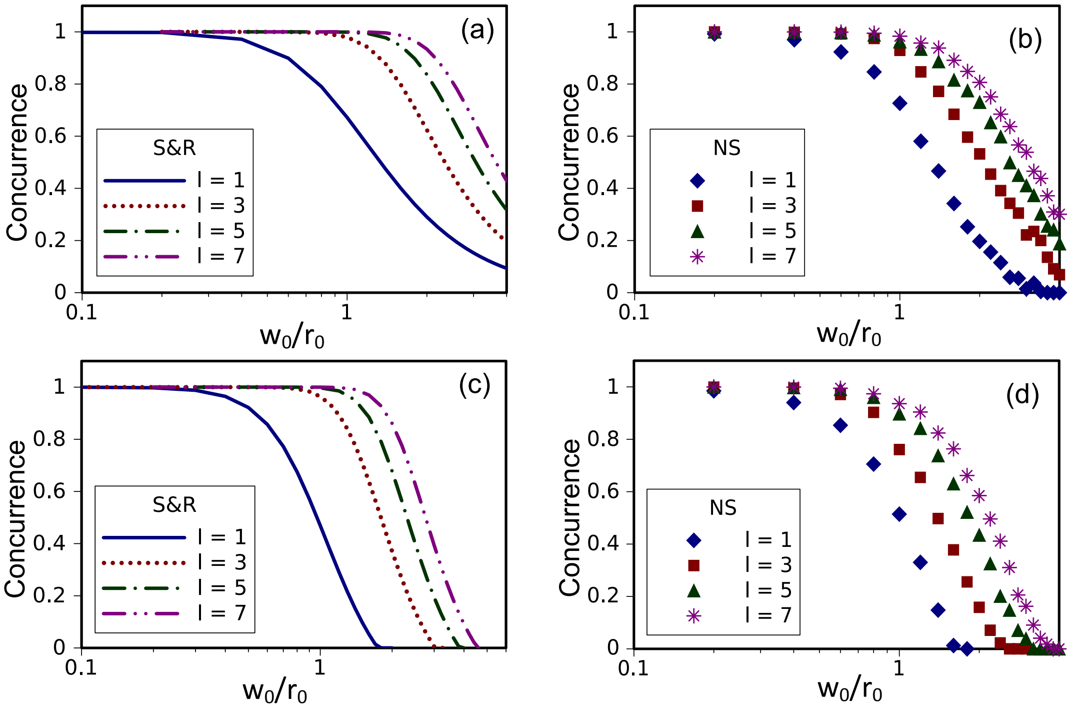

Figure 3.15: The concurrence plotted against the scintillation strength ω_0/r_0 for the S&R theory and the numerical results in the single photon case [(a) and (b)] and in the two-photon case [(c) and (d)]. The horizontal axis is plotted on a logarithmic scale.

Thus for a practical free-space quantum communication system using OAM modes as qubits, the distance between repeaters should be shorter than $L_{\rm dec}(\ell)$. For example, if one would send OAM entangled photons in a beam with $\omega_0 = 10$ cm, a wavelength of $\lambda = 1550$ nm, on a horizontal path in moderate turbulence conditions ($C_n^2 = 10^{-15}$ m$^{-2/3}$), the entanglement between the photons will decay around the distances shown in Table 3.1 for the different values of ℓ.

ℓ	1	3	5	7
$L_{\rm dec}$(km)	6.7	16.7	25.6	33.7

Table 3.1: Distance scale at which entanglement decays for OAM entangled photons in a beam with $\omega_0 = 10$ cm, a wavelength of $\lambda = 1550$ nm, on a horizontal path in moderate turbulence ($C_n^2 = 10^{-15}$ m$^{-2/3}$).

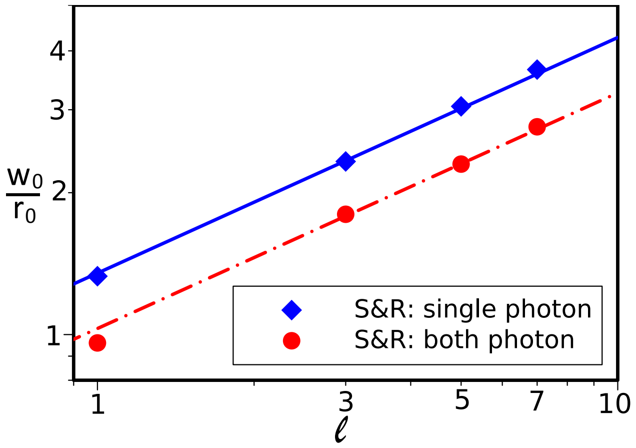

Figure 3.16: The scintillation strength plotted against ℓ on a logarithmic scale for both the single photon case (diamond dots) and the two-photon case (circular dots). The equation of the fitted lines are $\log(\omega_0/r_0) = 0.5\log(\ell) + 0.1303$ in the single photon case and $\log(\omega_0/r_0) = 0.5\log(\ell) + 0.01284$ in the two photon case.

We notice in Table 3.1 that the distance scale at which entanglement decays is relatively short even in moderate turbulence. This suggests that the OAM state of light might not be suitable for long distance free-space quantum communication. One can try to increase that distance by using a smaller beam radius, but that would increase beam divergence, which in turn reduces the received power for a given receiver aperture. The entanglement decay distance can also be increased by using adaptive optics.

3.3.2 OAM entanglement through turbulence simulated by multiple phase screens

The single phase screen approximation limits the validity of the predictions in the previous Section to the weak fluctuations regime. In order to simulate the turbulent atmosphere accurately, one needs to use a multitude of phase screens as described in Section 2.4.3. Here, we simulate the turbulent atmosphere with a series of consecutive phase screens. The distance between adjacent phase screens correspond to an increment of 0.2 in the value of $(w_0/r_0)^{5/3}$ and both photons propagate through turbulence. We use increments of $(w_0/r_0)^{5/3}$ instead of w_0/r_0 because this quantity is linear with the total propagation z. This allows us to have a fixed distance Δz between the phase screens. The numerical results will be compared with the infinitesimal propagation equation (IPE) derived in [90] (discussed in section 2.4.6).

The IPE is a first order differential equation describing the evolution of OAM entanglement in turbulence. It was derived by treating the distortion that an OAM state experiences due to propagation through a thin sheet of turbulent atmosphere as an infinitesimal transformation. It is thus based on multiple phase screens and predicts the evolution of entanglement even in the strong fluctuation regime.

In the weak fluctuation regime, both the single phase screen and the multiple phase screens should return the same results as shown in Fig. 3.17.

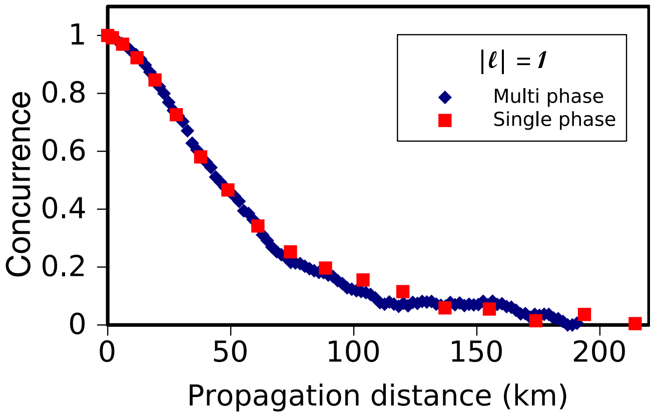

Figure 3.17: The concurrence plotted against the propagation distance for both the single phase screen and multiple phase screens in the weak scintillation regime.

As we increase the fluctuation strength, we expect a difference in the predictions made by the single and multiple phase-screens methods.

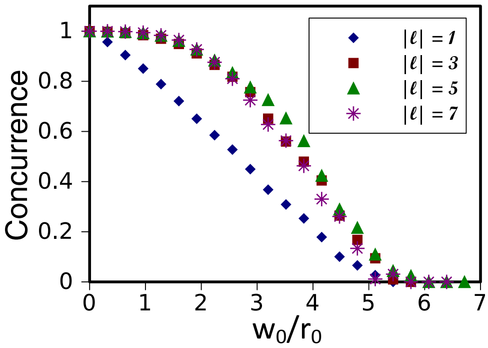

Figure 3.18: The concurrence plotted against the scintillation strength (w_0/r_0) for multiple phase screens in the moderate fluctuation regime.

Figure 3.18 shows the evolution of the concurrence against the scintillation strength in moderate fluctuations ($\sigma_R^2 \approx 0.1$ when the concurrence reaches 0) for the multiple phase screens. Already in this regime, the evolution of the concurrence is different to what was found with the single phase screen approximation in the weak fluctuation regime. For instance, it was observed in the weak fluctuation regime that the concurrence lasts longer for higher values of $|\ell|$, here, we see that the concurrence decays to zero around the same value of w_0/r_0. This suggests that in the moderate to strong fluctuation regime, the evolution of the concurrence can no longer be characterised by a single dimensionless parameter (w_0/r_0) like in the weak-fluctuation regime. This confirms what was reported in Ref. [90] that the evolution of concurrence requires at least two parameter: the normalized propagation distance

$$t = \frac{z}{z_R} = \frac{z\lambda}{\pi w_0^2}, \tag{3.24}$$

which is independent of the turbulent strength, and another parameter

$$K = \frac{C_n^2 w_0^{11/3} \pi^3}{\lambda^3}, \tag{3.25}$$

which is independent of the propagation distance. The dimensionless parameters w_0/r_0 and K are just two possible ways of combining the dimension-carrying parameters. The parameters w_0/r_0, K and t are related by

$$\frac{w_0}{r_0} = 1.37K^{3/5}t^{3/5}. \tag{3.26}$$

$\log(K)$	w_0 [m]	C_n^2 [m$^{-2/3}$]	λ [nm]
1.5	0.2	$9.7 \cdot 10^{-16}$	1400
2	0.05	$3.2 \cdot 10^{-13}$	1190
2.5	0.1	$5.0 \cdot 10^{-15}$	481
3	0.05	$1.0 \cdot 10^{-12}$	807.2
3.5	0.1	$9.7 \cdot 10^{-14}$	600
4	0.1	$5.0 \cdot 10^{-12}$	1494.8
4.5	0.1	$9.7 \cdot 10^{-13}$	600
5	0.5	$9.7 \cdot 10^{-15}$	618.7

Table 3.2: Parameters used for the plots in Fig. 3.19, 3.20, 3.21 and 3.22

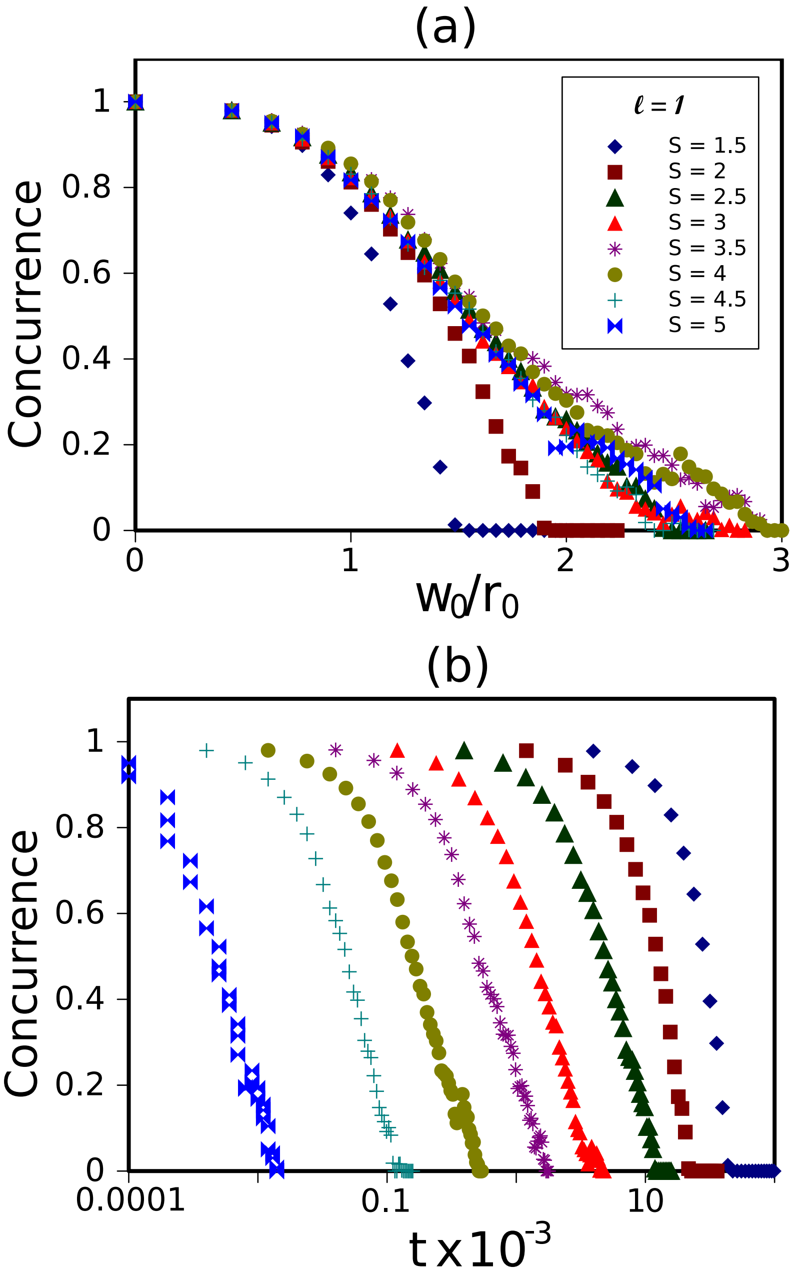

Figure 3.19: The concurrence plotted against w_0/r_0 (a) and against t (b) for $\ell = 1$ and for different values of $S = \log_{10}(K)$ in the multiple phase screen method.

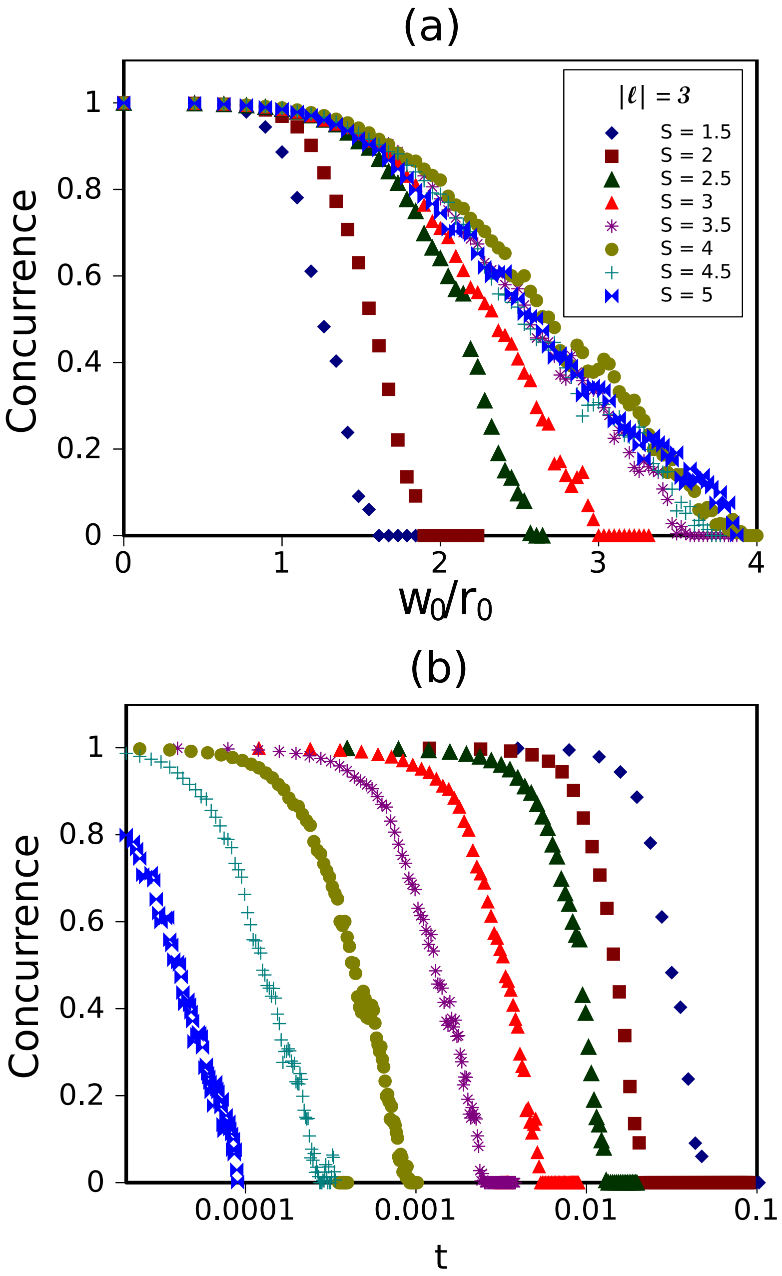

Figure 3.20: The concurrence against w_0/r_0 (a) and against t (b) for $\ell = 3$ and for different values of $S = \log_{10}(K)$ in the multiple phase screen method.

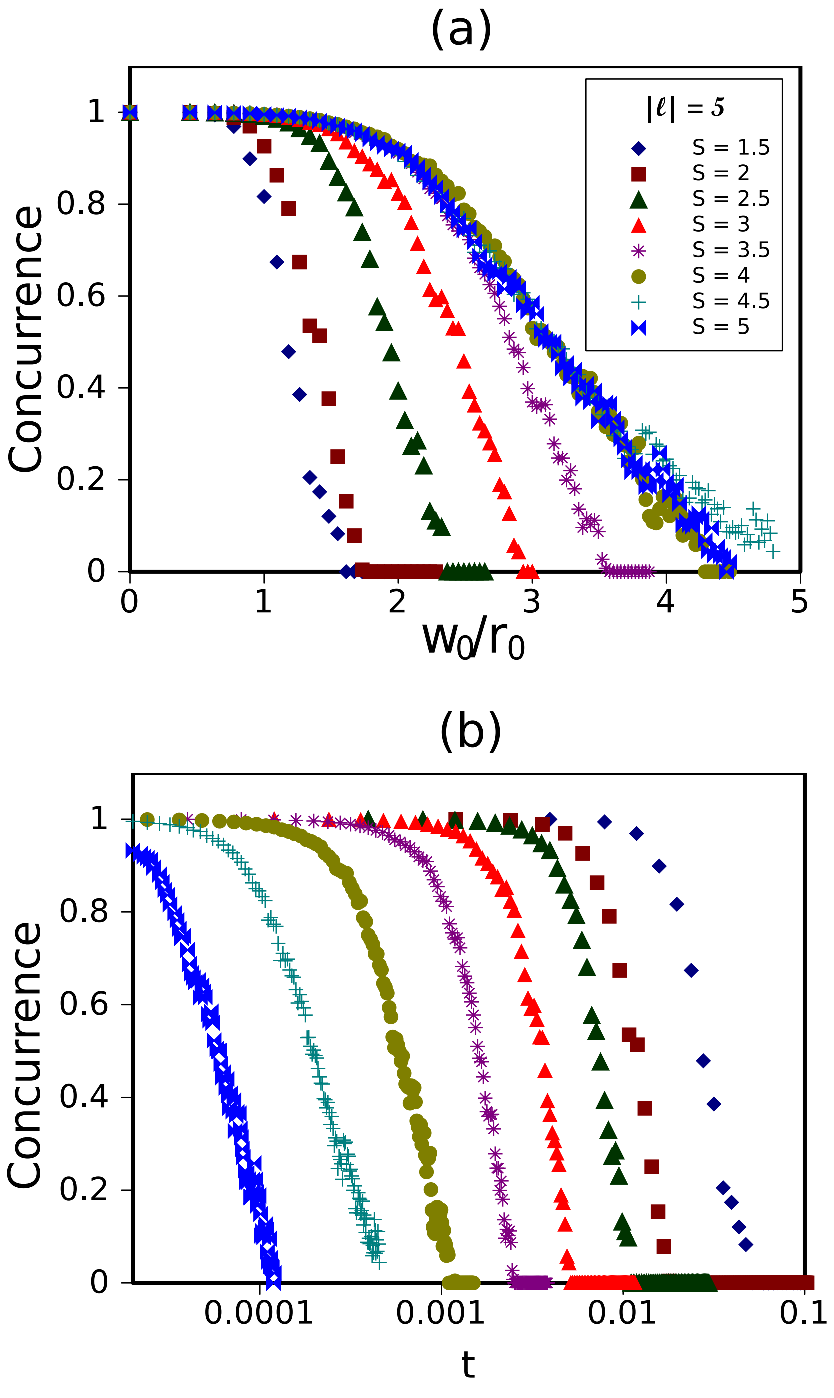

Figure 3.21: The concurrence plotted against w_0/r_0 (a) and against t (b) for $\ell = 5$ and for different values of $S = \log_{10}(K)$ in the multiple phase screen method.

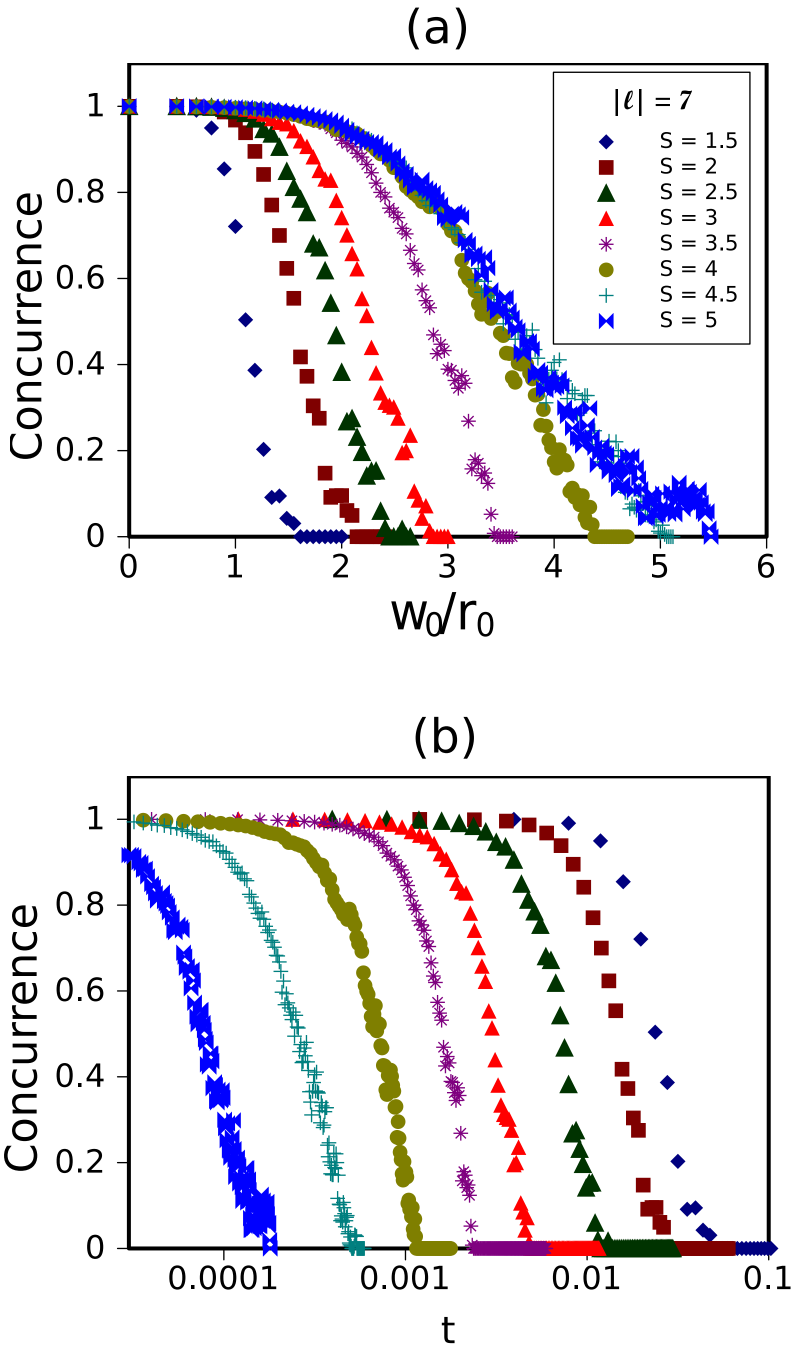

Figure 3.22: The concurrence plotted against w_0/r_0 (a) and against t (b) for $\ell = 7$ and for different values of $S = \log_{10}(K)$ in the multiple phase screen method.

Figures 3.19, 3.20, 3.21 and 3.22 show the plots of the concurrence against w_0/r_0

and against t for the different values of $S = \log_{10}(K)$ and the azimuthal index ℓ considered. The different sets of dimension parameters that were used to produce the different values of K are given in Table 3.2. It can be seen from those figures that the plot of the concurrence against w_0/r_0 coincide with one another for larger values of S, that is they lie on a limiting curve.

As a function of w_0/r_0, the curves of the concurrence lie on the limiting curves for large values of K, but they tend to fall below this limiting curve when K is small. This suggests that there is a value of K beyond which the evolution of the concurrence depends only on w_0/r_0. This corresponds to the situation that is considered in the Paterson model [41], where the behaviour is completely determined by w_0/r_0.

On the other hand, for small values of K, the plots of the concurrence deviate from the limiting curve, in that they decay faster than the limiting curve as a function w_0/r_0. This suggests that the Paterson model can not be used under these conditions. Two dimensionless parameters are required to describe the behaviour of the concurrence and the trace during propagation under these conditions, namely K and t.

Our results are qualitatively similar to those obtained with the IPE [90] (discussed in section 2.4.6), but the detailed behaviour is quantitatively different. The IPE predicts that for a value of the normalised propagation distance $t > 1/3$, the evolution of the OAM entanglement can no longer be described by the single dimensionless parameter w_0/r_0. One needs the two dimensionless parameters K and t. Our results [Fig. 3.19 (b), 3.20 (b), 3.21 (b) and 3.22 (b)] on the other hand, show that the value of t beyond which the Paterson model doesn't hold depends on the value of ℓ. For instance, we see from Fig. 3.19 (b), 3.20 (b), 3.21 (b) and 3.22 (b) that the value of t beyond which one needs the two dimensionless parameters K and t to describe the evolution of the concurrence (the value of t beyond which the curves of the concurrence against w_0/r_0 do not overlap any more) is 0.01 when $\ell = 1$, 0.007 when $\ell = 3$, 0.003 when $\ell = 5$ and 0.001 when $\ell = 7$.

Although one can see from the plots in Figs. 3.19, 3.20, 3.21 and 3.22 that one dimensionless parameter is not enough to describe the evolution of the entanglement, they do not reveal whether more than two dimensionless parameters are not perhaps required. For this purpose we consider different sets of dimension parameters that give the same value for K and plot them as a function of t.

	w_0 [m]	C_n^2 [m$^{-\frac{2}{3}}$]	λ [nm]
Set 1	0.04	10^{-13}	633.0
Set 2	0.05	10^{-14}	385.8
Set 3	0.10	10^{-15}	417.8
Set 4	0.20	10^{-16}	452.4
Set 5	0.40	10^{-17}	489.9

Table 3.3: Parameters used for the plots in Fig. 3.23 ($K = 91.6$).

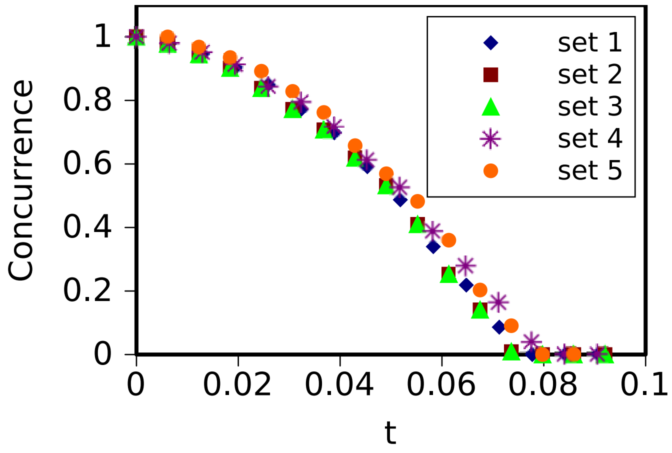

Figure 3.23: Plots of the concurrence plotted against t for $K = 91.6$ when $|\ell| = 1$. The values of the parameters used for each plot is given in table 3.3

Figure 3.23 shows the plots of the concurrence as a function of t for $K = 91.6$ when $|\ell| = 1$. Five different sets of parameters (shown in Table 3.3) that produce the same value of K are considered. We see from the figure that regardless of the values of the individual parameters, all the points that correspond to the same value of K lie on the same curve.

3.4 Conclusion

We have presented a numerical study of the evolution of OAM entanglement between a pair of photons propagating through atmospheric turbulence. Different values of the OAM index were considered and we compared our results with the two theories discussed in section 2.4.4: the S&R [84] and the IPE [90]. We considered two different scenarios: the case where the turbulent atmosphere is simulated with a single phase screen and the case where it is modelled with a series of consecutive phase screens. In the case where the turbulent atmosphere was simulated with a single phase screen, the entanglement of states with larger OAM values took more time to decay, suggesting that states with larger OAM values will be more suitable for free-space quantum communication. On the other hand, it was observed that modes with larger OAM values are scattered more rapidly into higher order modes. Our results are similar to what was found in previous work [84, 90]. We derived an expression for the scale distance at which entanglement decays as a function of ℓ. This expression can be used to find the maximum distance over which OAM-entangled photons propagate before they lose their entanglement in the weak fluctuation regime.

In the case where the turbulent atmosphere was simulated with a series of consecutive phase screens, we studied the evolution of OAM entanglement for different values of the dimensionless parameter K given in Eq. 3.25. It was found that the evolution of OAM entanglement cannot always be described only by the dimensionless parameter w_0/r_0. For smaller values of K, two parameters are required to describe the evolution of the OAM entanglement in turbulence; one being the normalised propagation distance (t) and another which is independent of the propagation distance (K).

Chapter 4

Experimental investigation of the decay of OAM entanglement in turbulence

4.1 Introduction

Many theoretical studies considered the effects of atmospheric turbulence on the orbital angular momentum (OAM) state of light. However, not enough experimental work has been done on the subject. Most of the theoretical work is based on the Paterson model (discussed in Section 2.4.5) using the single phase screen approximation which assumes that the overall effect of the turbulent medium on a propagating beam is a phase distortion only [41].

The single phase screen approximation has also been used to simulate turbulence in experimental studies. For instance, the crosstalk among OAM modes was experimentally measured [80,81], where the turbulence was simulated with a single phase screen.

There have also been experimental studies where the turbulence was not simulated with a single phase screen. These include the work by Pors *et al.* [83], where it was shown, using coincidence counts, that the number of entangled modes (the Shannon dimensionality) decreases with increasing scintillation; and the work by Rodenburg *et al.* [82] where a 1 km thick turbulent medium was simulated in the lab with two phase screens and the cross-talk in the communication channels was reduced using an adaptive correction of the turbulence, as well as optimization of the channel encoding. However, none of the experimental studies directly addressed the decay of OAM entanglement due to atmospheric turbulence. In this chapter, we present the first such experiment. We investigate the decay of OAM entanglement of photon pairs propagating in a turbulent atmosphere modelled with a single phase screen. This is an experimental verification of the theoretical study done by Smith and Raymer (S&R). The results obtained are compared to previous theoretical work (the S&R theory and the IPE) discussed in Section 2.4.4 and the numerical results presented in Chapter 3.

It is important to study the evolution of OAM entanglement in turbulence experimentally. For instance, if one wants to get a realistic picture of a QKD system, one should do experiments in order to include experimental and detection uncertainties.

This chapter is organized as follows: The experimental procedure is presented in section 4.2 followed by the results and discussions in section 4.3. Some conclusions are provided in section 4.4.

The results presented in this chapter were obtained by the author with input and guidance from Dr. Filippus S. Roux, Prof. Thomas Konrad and Prof. Andrew Forbes. Melanie McLaren assisted with the experimental setup.

4.2 Experimental procedure

Our experimental setup is shown in Fig. (5.6). A 3 mm thick type I beta-barium borate (BBO) crystal is pumped with a collimated pump beam that has a radius of 0.5 mm at the crystal, a wavelength of 355 nm and an average power of 350 mW to produce collinear, degenerate entangled photon pairs via spontaneous parametric down conversion (SPDC) as describe in Section 2.3.2. The pump beam is blocked by a filter (IF_1) after passing through the crystal. Because the setup is collinear, both the signal and the idler are incident on the same beam splitter (BS). The crystal plane is imaged using a $4f$ telescope with L_1 ($f_1 = 200$ mm) and L_2 ($f_2 = 400$ mm) onto two separate spatial light modulators (SLMs). The LG

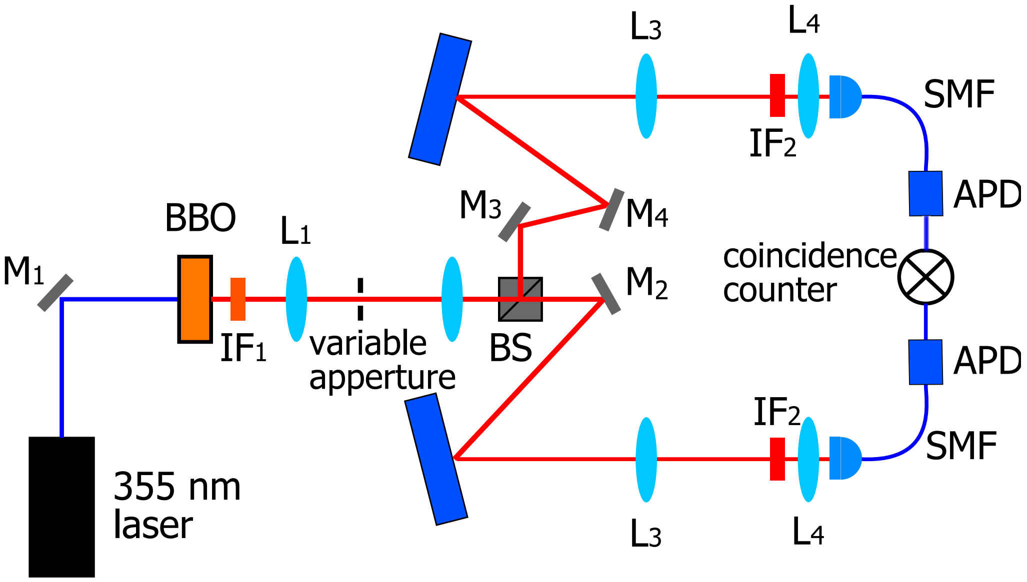

Figure 4.1: Experimental setup used to detect the OAM eigenstate after SPDC. The plane of the crystal is relayed imaged onto two separate SLMs using lenses, L_1 and L_2 (f_1 = 200 mm and f_2 = 400 mm), where the LG modes are selected. Lenses L_3 and L_4 (f_3 = 500 mm and f_4 = 2 mm) are used to relay image the SLM planes through 10 nm bandwidth interference filters (IF) to the inputs of the single-mode fibres (SMF). The fibres are connected to avalanche photodiodes (APDs), which are then connected to a coincidence counter.

modes to be measured, together with the turbulence, is encoded onto the SLMs. The SLMs are imaged by lenses L_3 (f_3 = 500 mm) and L_4 (f_4 = 2 mm) to the inputs of the single-mode fibres, where only the fundamental Gaussian mode is coupled into the fibres. Bandpass filters (IF_2) of width 10 nm and centred at 710 nm are placed in front of the fibres to ensure that the photons detected have the desired wavelength. The fibres are connected to avalanche photodiodes (APDs), which are then connected to a coincidence counter where the photon pairs are registered. The photon fluctuations from the pump beam produced an uncertainty in the measured coincidence counts of approximately 5%. All measured coincidence counts are accumulated over a 10 second integration time with a gating time of 12 ns.

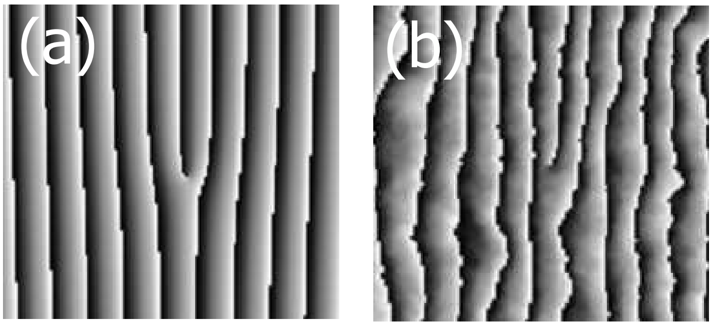

Figure 4.2: the phase function of the SLM when $\ell = 1$ without the random phase fluctuation simulating turbulence (a) and with the random phase added (b).

The atmospheric turbulence is simulated by adding random phase fluctuations [as given by Eq. (2.106)] to the phase function of one of the SLMs in the case when only one of the photons propagates through turbulence, and to the phase functions of both SLMs in the case when both photons propagate through turbulence. Figure 4.2 shows the phase function of the SLM when $\ell = 1$ without the random phase fluctuation simulating turbulence (a) and with the random phase added (b). The scintillation strengths (ω_0/r_0) range from 0 to 4 with an increment of 0.2. Measurements for each scintillation strength are repeated 30 times and a full state tomography (see section 2.3.3) is done after each run to reconstruct the density matrix.

Because of experimental imperfection, the density matrix reconstructed through a state tomography has negative eigenvalues. These negative eigenvalues are removed by adding the absolute value of the most negative eigenvalue to the diagonal elements of the reconstructed density matrix and renormalising the results. Furthermore, if the error bars of the resulting eigenvalues, computed from Poisson statistics, still pushed below zero, the mean and standard deviations of these eigenvalues are adjusted so that they remain above zero. The reconstructed density matrices are then averaged to obtain the mean density matrix for each scintillation strength. And the concurrence [122] is used to quantify the entanglement between the two photons.

4.3 Results and discussion

Two different scenarios will be considered here. In the first scenario, only one of the two photons propagates through the turbulence. This scenario will be referred to as the “single-photon case.” In the second scenario, both photons propagate through the turbulence. This case will be referred to as the “ two-photon case.”

Atmospheric turbulence distorts a propagating optical beam in many ways. For instance, turbulence leads to beam wandering (tip and tilt), beam size changes (defocus) and beam distortion (higher order aberrations) effects. Figure 4.3 shows examples of such beam distortions. These images are the intensity profiles of the beams in the plane of the BBO crystal when the SLM that contains the phase fluctuations is illuminated with back-projected light. That is, the APD in one of the arms of the experimental setup (Fig. 5.6) is replaced by a laser diode, shining light backward through the fibre to illuminate the SLM.

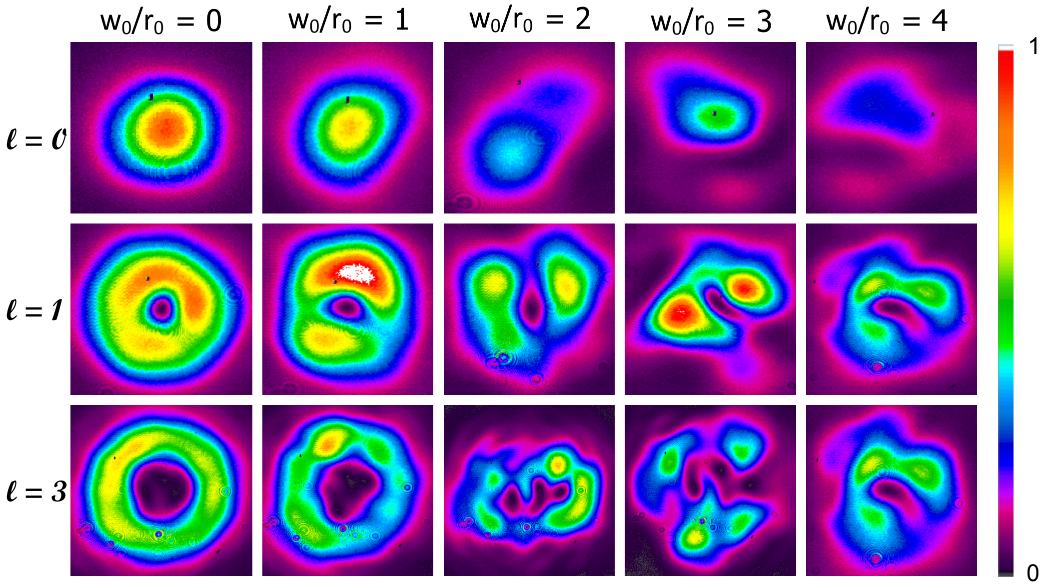

Figure 4.3: The intensity profile of LG beams with different ℓ as they propagates through turbulence with increasing scintillation strength.

At a single photon level, this distortion results in the scattering of the initial OAM mode into neighbouring modes. When a photon with a given OAM mode propagates through turbulence, the distortions cause the photon to become a superposition of many OAM modes. In other words, an initial OAM state of the photon $|l_0\rangle\langle l_0|$ will become

$$|l_0\rangle\langle l_0| \to \sum_{nm} c_{nm}|l_n\rangle\langle l_m| \tag{4.1}$$

after it propagates in turbulence. Here, the c_{nm} are are complex coefficients. Figure 4.4 shows an illustration of the mode scattering for both scenarios where initially [Fig. 4.4(a) and (d)] there is no turbulence and we have coincidences only along the diagonal ($\ell_A = -\ell_B$). When we turn on the turbulence, we detect more coincidences along the off-diagonal ($\ell_A \neq -\ell_B$) as we increase the scintillation strength.

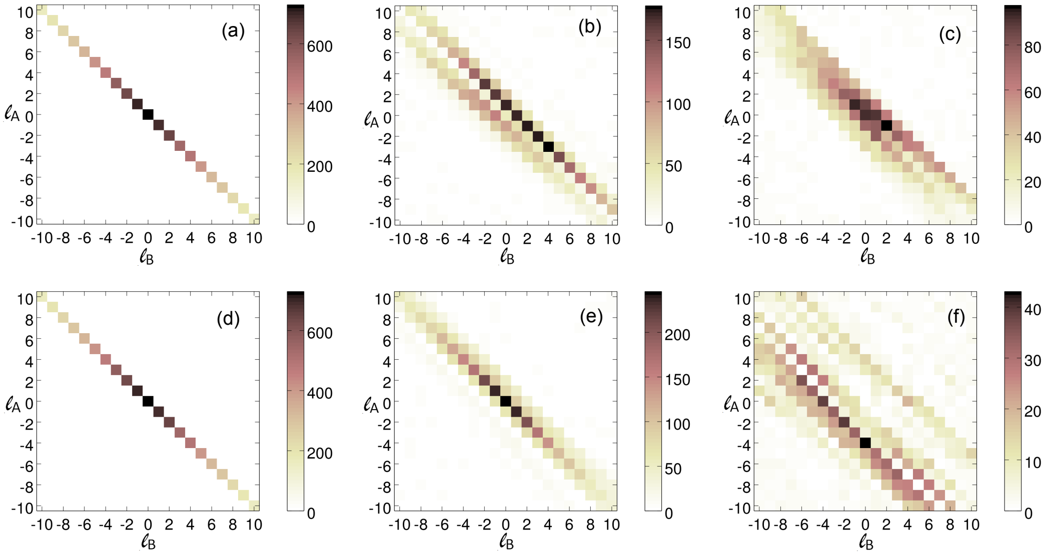

Figure 4.4: Mode scattering under the effect of turbulence given by the coincidence counts for simultaneous measurements of modes with azimuthal index ℓ_A in the signal beam and ℓ_B in the idler beam when only one of the two photons propagates through turbulence [(a), (b) and (c)] and when both photons propagate through turbulence [(d),(e) and (f)]. With no turbulence [(a) and (d)], only anti-correlated coincidences are observed. As the scintillation strength increases to $\omega_0/r_0 = 2$ [(b) and (e)] and $\omega_0/r_0 = 4$ [(c) and (f)], the mode scattering becomes more pronounced.

The entanglement between the two photons will be distorted as a result of the mode scattering. In the next section, we study the evolution of the entanglement in turbulence in the single photon case.

4.3.1 Single photon case

In Fig. 4.5, we compare the experimental data (Exp) with the numerical simulation results (NS) presented in chapter 3 and the two theories discussed in Section 2.4.4, namely the S&R theory and IPE.

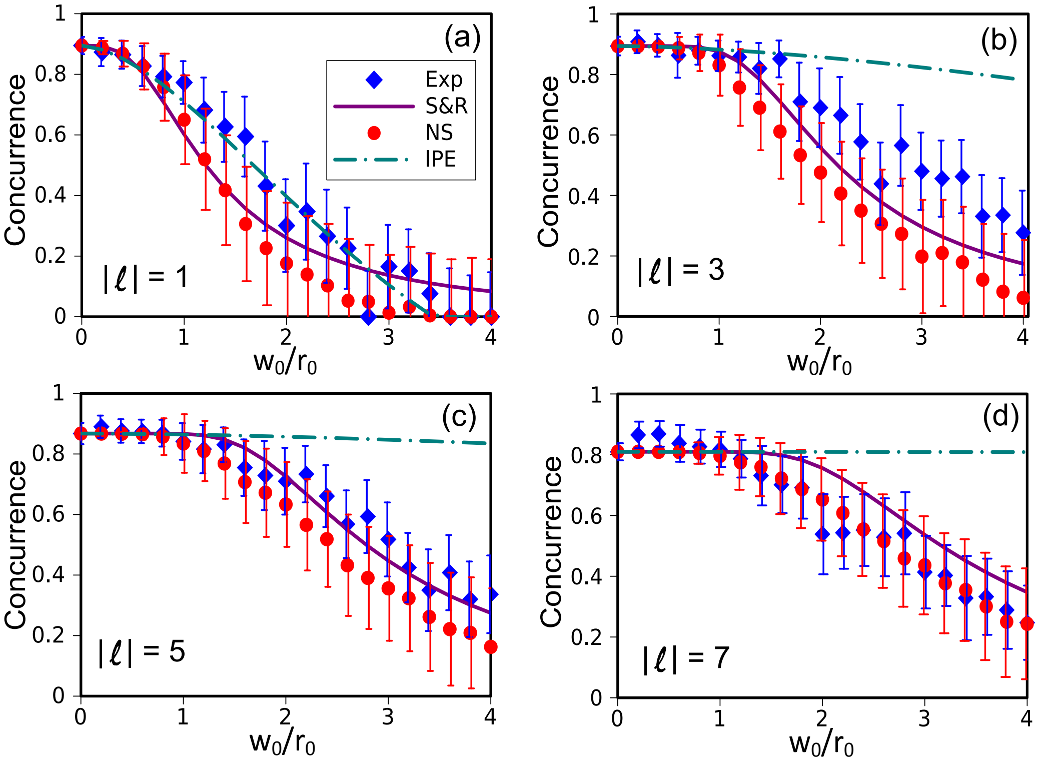

Figure 4.5: The concurrence plotted against the scintillation strength (w_0/r_0) when only one photon is propagated through turbulence. In (a) $|\ell| = 1$, in (b) $|\ell| = 3$, in (c) $|\ell| = 5$ and in (d) $|\ell| = 7$. In the legend, Exp: experimental data points, S&R: theory curve derived by Smith and Raymer in [84], IPE: the infinitesimal propagation equation presented in [90] and NS: Numerical data points.

When $|\ell| = 1$, the experimental results agree, within experimental error with the numerical results, the S&R theory and the IPE. As one increases the value of

$|\ell|$, the experimental results remain consistent with the numerical results and the S&R theory, but increasingly disagree with the IPE.

It can also be observed that both the S&R theory and the numerical results indicate that the concurrence lasts longer for higher values of $|\ell|$. This is clearly seen in Fig. 4.6 where we plot the evolution of the concurrence for all the $|\ell|$-values considered on the same graph for the S&R theory [Fig. 4.6(a)], the IPE [Fig. 4.6(b)], the numerical simulation [Fig. 4.6(c)] and the experiment [Fig. 4.6(d)]. The experimental results were normalized by dividing the values of the concurrence by the initial value obtained for each $|\ell|$. Furthermore, the S&R theory predicts that the spacing between adjacent curves decreases as $|\ell|$ increases. This is also true for the numerical simulation.

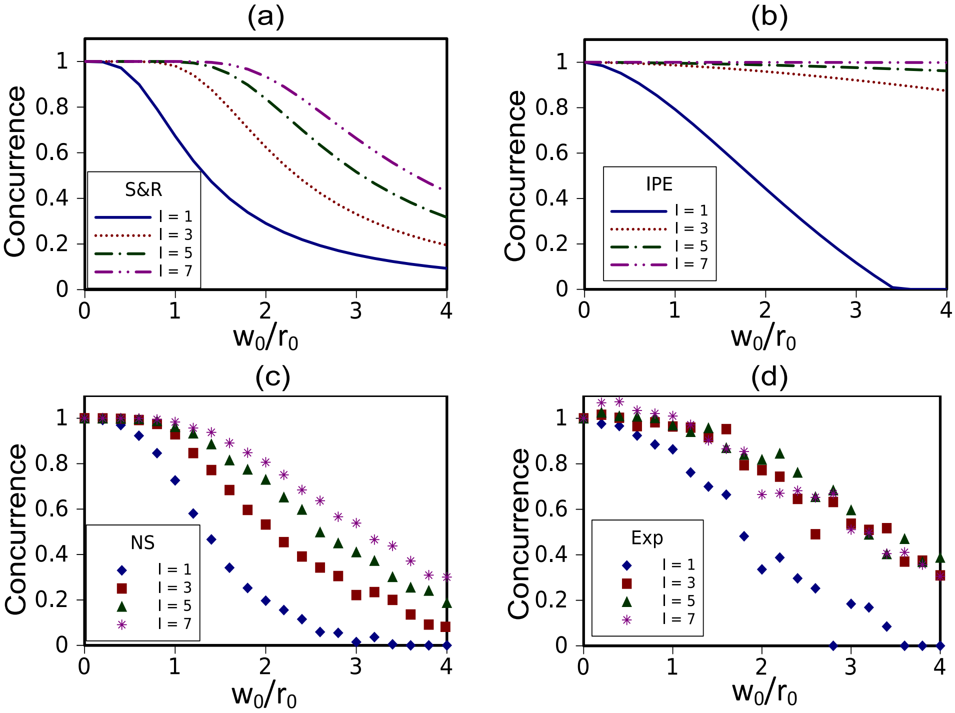

Figure 4.6: The concurrence plotted against the scintillation strength (w_0/r_0) when only one photon is propagated through turbulence for $|\ell| = 1, 3, 5$ and 7. (a): the S&R theory; (b): the IPE; (c): The numerical simulation and (d): the experimental results; we normalized the concurrence by dividing the values by the initial value obtained for each ℓ.

The IPE also predicts that the concurrence will last longer for higher $|\ell|$-values as shown in Fig. 4.6(b), in addition, it predicts that the concurrence decays at a much slower rate and it completely deviates from the other curves when $|\ell| > 1$. The reason for this is that the IPE underestimates the coupling of different basis elements that are far apart. This is discussed in section 4.3.3.

Our experimental results also suggest that the concurrence lasts longer for higher $|\ell|$-values as we can see a clear increment between $|\ell| = 1$ and $|\ell| = 3$ as predicted by both theories and the numerical simulation [Fig. 4.6(d)]. For instance when $|\ell| = 1$, the concurrence decays to zero around the point where $\omega_0/r_0 = 4$ whereas the value of the concurrence is about 0.25 at $\omega_0/r_0 = 4$ when $|\ell| = 3$. However there is no clear distinction between the points corresponding to $|\ell| = 3, 5$ and 7 (the concurrence is about 0.25 at $\omega_0/r_0 = 4$ for all these cases). This might be due to experimental imperfection. As the $|\ell|$-value increases, the coincidence counts drop significantly and background counts have a more important effect on the results.

4.3.2 Two-photon case

It is important to quantify the effect of atmospheric turbulence on the OAM entanglement when both photons propagate through the turbulent medium. This is because this scenario can occur quite often in a practical quantum communication system. For instance, we can think of a situation where a pair of entangled photons is generated and sent to two different parties (Alice and Bob) for a quantum information task such as quantum teleportation. In this section, the results obtained in the two-photon scenario are presented.

The general evolution of the concurrence in the two-photon case is quite similar to the evolution in the single photon case as one can see in Fig. 4.7 where the concurrence is plotted against the scintillation strength. The main difference between the two scenarios is that the concurrence decays quicker in the two-photon case.

Just like in the single-photon case, the experimental results agree with the numerical results and both theories when $\ell = 1$ [Fig. 4.7(a)]. As we increase the value

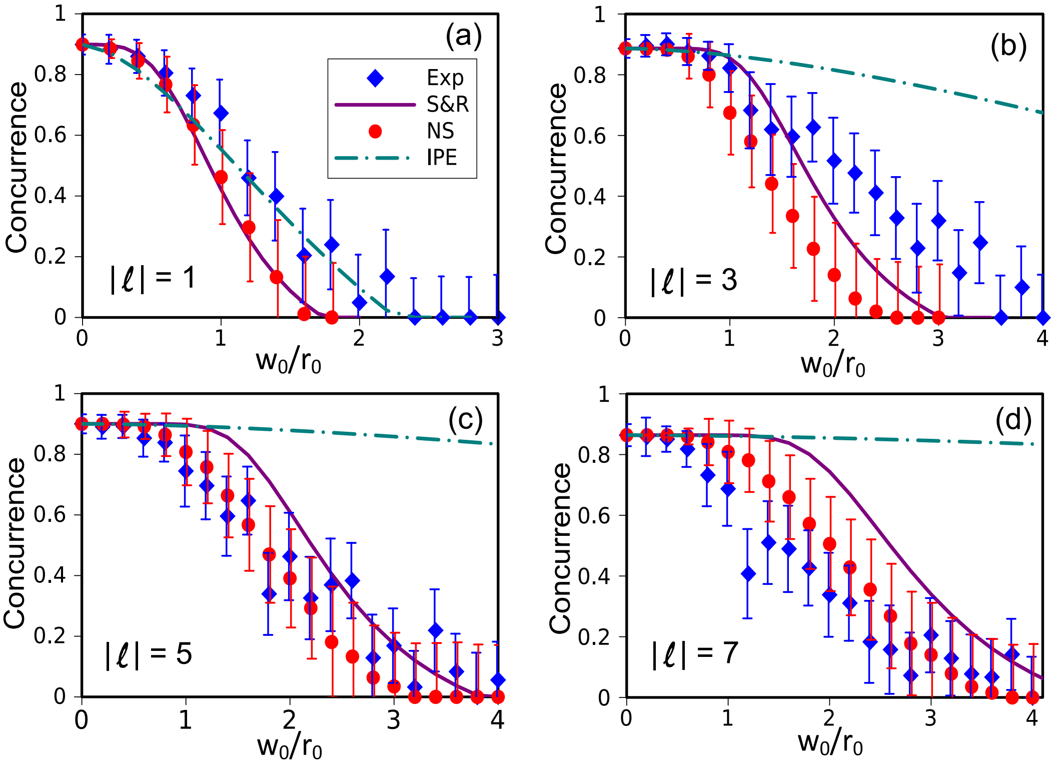

Figure 4.7: The concurrence plotted against the scintillation strength (w_0/r_0) when both photons are propagated through turbulence. In (a) $|\ell| = 1$, in (b) $|\ell| = 3$, in (c) $|\ell| = 5$ and in (d) $|\ell| = 7$. In the legend, Exp: experimental data points, S&R: theory curve derived by Smith and Raymer in [84], IPE: the infinitesimal propagation equation presented in [90] and NS: Numerical data points.

of ℓ, the experimental results remain consistent with the numerical simulation and the S&R theory but increasingly disagree with the IPE.

It can also be seen in Fig. 4.7 that the concurrence decays slower for higher ℓ-values, as in the single photon case. This is more clearly seen in Fig. 4.8 where we plot the evolution of the concurrence for all the $|\ell|$-values considered on the same graph for the S&R theory [Fig. 4.8(a)], the IPE [Fig. 4.8(b)], the numerical simulation [Fig. 4.8(c)] and the experiment [Fig. 4.8(d)].

The IPE predicts a slower decay rate and completely deviates from the other curves when $\ell > 1$ for the reasons discussed in Section 4.3.3.

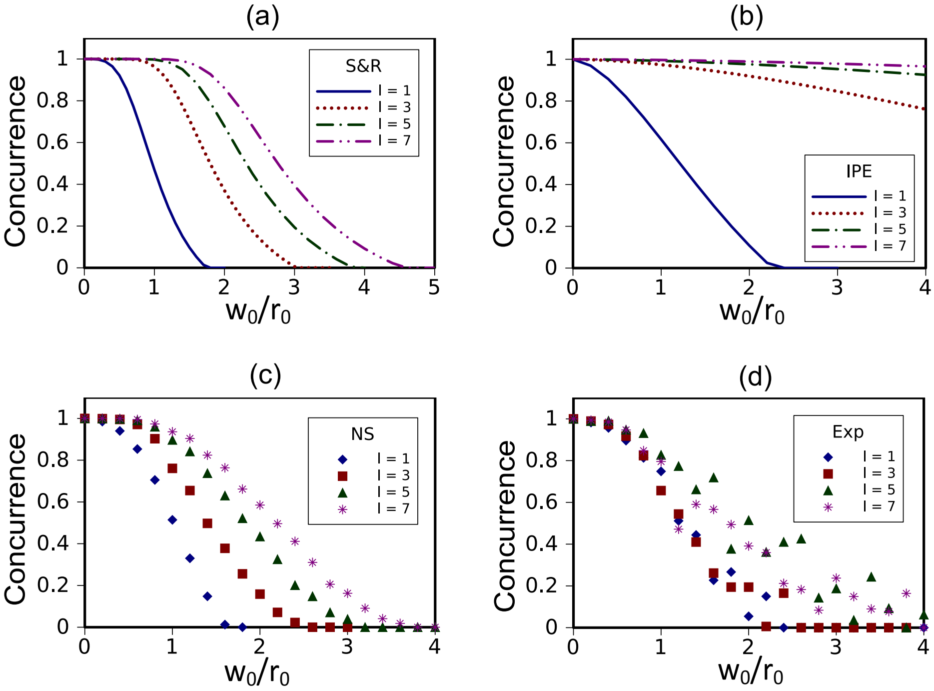

Figure 4.8: The concurrence plotted against the scintillation strength (w_0/r_0) when both photons propagate through turbulence for $|\ell| = 1, 3, 5$ and 7. (a): the S&R theory; (b): the IPE; (c): The numerical simulation and (d): the experimental results; we normalized the concurrence by dividing the values by the initial value obtained for each ℓ.

Our experimental results support the fact that the concurrence lasts longer for higher $|\ell|$-values [Fig. 4.8(d)]. The concurrence decays to zero around $\omega_0/r_0 = 2.5$ when $|\ell| = 1$ and 3 whereas it decays to zero around $\omega_0/r_0 = 4$ when $|\ell| = 5$ and 7. The curves corresponding to $\ell = 1$ and 3 and those corresponding to $\ell = 5$ and 7 seem to overlap. This is again due to experimental imperfections. As it was stated in the previous section, it becomes more difficult to measure the mode accurately for higher $|\ell|$-values. Furthermore, because now both photons propagate in the turbulence, the fluctuations in the coincidence counts are higher than in the single-photon case.

4.3.3 Truncation problem in the IPE

Even though the IPE is not based on the single phase screen and the quadratic structure function approximations that are made in the S&R calculation, it suffers from a drawback when it comes to the effect of truncations.

In order to obtain the density matrix describing the evolution of OAM entanglement between two qubits, the IPE and the Paterson model both need to be truncated. The effect of truncations is to remove all the backward interactions from the neglected elements to those that are included in the truncated matrix. The turbulent medium represented by the single phase screen in the Paterson model is a thicker medium than the infinitesimal step in the IPE. Consequently, the single phase screen in the Paterson model incorporates multiple scattering. This causes the coupling strengths between basis element that are further apart to be stronger in the Paterson model than they are in the IPE. The IPE cannot see the multiple scattering that would take $\ell = q$ to $\ell = -q$ via the intermediate basis elements with $|\ell| < q$ if these latter basis elements are removed from the truncated matrix. Thus the coupling between $\ell = q$ and $\ell = -q$ becomes much smaller in the IPE than the equivalent coupling in the Paterson model. Due to the smaller couplings in the truncated IPE, it predicts a much slower decay rate for the concurrence than is observed experimentally and numerically.

4.4 Conclusions

We presented the first experiment studying the evolution of OAM entanglement between two qubits in atmospheric turbulence. The turbulent atmosphere was modelled with a single phase screen and modes with $|\ell|$-values 1,3, 5 and 7 were considered. Our results were compared with the numerical results presented in Chapter 3 and the two theories discussed in Section 2.4.4: the S&R [84] and the IPE [90]. We considered two different scenarios: the case where only one of the two photons propagates through turbulence and the case where both photons propagate through turbulence. In both these scenarios, our results agree with the numerical results and the S&R theory and suggest that modes with higher $|\ell|$-values are more robust in turbulence. This implies that modes with higher ℓ-values could thus give an advantage in a free-space quantum communication system. However, it is also observed that modes with higher $|\ell|$-values are more difficult to measure experimentally. This is due to the fact that as the value of ℓ increases, the coincidence counts drop significantly and background counts have a more important effect on the results.

Our results disagree with the IPE when $\ell = 3, 5$ and 7. The reason for this could be the fact that the IPE underestimates the coupling of different basis elements that are far apart.

Chapter 5

Decay of multidimensional entanglement through turbulence

5.1 Introduction

Quantum entanglement is the main resource that gives an advantage to quantum communication and information tasks over their classical counterparts. A great majority of these quantum information tasks make use of two-dimensional entangled systems (qubits). This is because the dynamics of quantum entanglement between two qubits have been extensively studied and are better understood. Moreover, it is not easy to manipulate and quantify entanglement in multidimensional systems.

However, as mentioned in chapter 1 multidimensionally entangled systems have been proved to significantly improve many quantum information tasks.

The evolution of OAM entanglement between two qubits in turbulence has been studied theoretically [84,90], numerically and experimentally in the previous chapters. However, the effects of turbulence on the OAM entanglement between two systems of dimensions higher than two have received little attention. In this chapter, the effects of atmospheric turbulence on the OAM entanglement between two qutrits (quantum state described by a three-dimensional Hilbert space) is investigated theoretically and experimentally. The qutrits are represented by photons entangled in the OAM basis. The turbulence is simulated with a single thin phase screen, using a spatial light modulator (SLM). Photon pairs entangled in the OAM mode are generated and one photon from each pair propagates through the turbulence while the other is left undisturbed. The entanglement is quantified by the tangle [128, 129] and the results obtained are compared with those presented in the previous chapters.

This chapter is organized as follows: The experimental procedure is presented in section 5.2 followed by the numerical procedure in section 5.3. The results and discussions are presented in section. 5.4. We introduce an experiment where down-converted photons are simulated with back-projected light in section 5.5 and some conclusions are provided in section 5.6.

The results presented in this chapter were obtained by the author with input and guidance from Dr. Filippus S. Roux, Prof. Thomas Konrad and Prof. Andrew Forbes. Melanie McLaren assisted with the experimental setup.

5.2 Experimental procedure

The experimental setup is the same as the setup presented in section 4.2. Entangled photon pairs were generated via spontaneous parametric down-conversion (SPDC) by pumping a 3 mm thick BBO crystal with a mode-locked laser having a 355 nm wavelength and an average power of 350 mW. The plane of the crystal was imaged onto two separate SLMs in the signal and idler beams, respectively. The SLMs served to perform projective measurements for quantum state tomography [130] by selecting particular pairs of modes for detection. The atmospheric turbulence was simulated by adding random phase fluctuations to the phase function of one of the SLMs. The SLM planes were re-imaged and coupled into single-mode fibres, which extract a near Gaussian mode from the incident field. Avalanche photo diodes (APDs) that were connected to the fibres registered the photon pairs via a coincidence counter (CC). All measured coincidence counts were accumulated over a 10 second integration time with a gating time of 10 ns.

The random phase screen that represents the turbulent medium is given by

Eq. (2.106) in section 2.4.3. This random phase was added to the phase function of one of the SLMs.

The Kolmogorov spectrum [86, 114]

$$\Phi_n^K(k) = 0.033\ C_n^2 k^{-11/3} \tag{5.1}$$

was used to allow for a comparison with existing studies, and subgrid sample points were added, as described in section 3.2.2 [125] to ensure that the random phase functions can reproduce the Kolmogorov structure function. The scintillation strength considered ranged from $w_0/r_0 = 0$ to 4, in 0.4 increments. Thirty realisations corresponding to different phase fluctuations were performed for each scintillation strength and a full quantum state tomography [130] was performed for each realization to reconstruct the density matrix describing the state of the two qutrits. These matrices were then averaged to obtain the density matrix corresponding to each scintillation strength.

The concurrence [122] is the preferred entanglement measure for two-dimensional bipartite systems. Unfortunately the generalisation of the concurrence to multidimensional systems is not a trivial problem. The lower bound for the concurrence can be obtained for multidimensional systems by computing the convex roof [131], however, this is computationally demanding. There are some generalisations of the concurrence to multidimensional systems, these include the G-concurrence [132, 133] and the I-concurrence [134]. Here, the tangle is used to quantify the amount of entanglement between the two qutrits [128, 129]. It is defined as

$$\tau(\rho) = 2\mathrm{tr}(\rho^2) - \mathrm{tr}(\rho_A^2) - \mathrm{tr}(\rho_B^2), \tag{5.2}$$

where ρ_A and ρ_B are the reduced density matrices of subsystems A and B. If ρ_{max} is a $d \times d$ dimensional density matrix representing a maximally entangle state, then

$$\tau(\rho_{max}) = 2(d-1)/d. \tag{5.3}$$

For bipartite two-dimensional states (qubits), the tangle is the lower bound for the square of the concurrence. This is illustrated in Fig. 5.1 where the tangle and

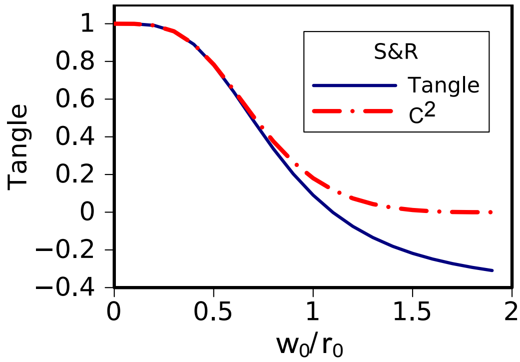

Figure 5.1: The tangle and the concurrence squared plotted against the scintillation strength (w_0/r_0). These curve are the S&R theory calculation for the evolution of the OAM entanglement between two qubits ($|\ell| = 1$) as they evolve in atmospheric turbulence (section. 2.4.5).

the concurrence squared are plotted against the scintillation strength. These curves are the S&R theory calculation for the evolution of the OAM entanglement between two qubits ($|\ell| = 1$) as they evolve in atmospheric turbulence (section. 2.4.5).

So far, only LG modes were considered in this work. In this chapter, we consider Bessel-Gauss (BG) modes instead [21]. The electric field of these modes is given by Eq. (2.31) in chapter 2, it is repeated here for convenience

$$M_\ell^{BG}(r,\phi,z;k_r) = \frac{iz_R}{q(z)} J_\ell\left(\frac{iz_R k_r r}{q(z)}\right) \exp\left[-\frac{k_r^2 z_R z}{2kq(z)} - ikz\right] \exp(i\ell\phi) \tag{5.4}$$

where $q(z) = z + iz_R$, $J(\cdot)$ is the Bessel function and $z_R = \pi w_0^2/\lambda$ is the Rayleigh range. The radial profile of the beam can be scaled by choosing different values of the radial k_r. Just like LG beams, the BG beams also carry an OAM of $\ell\hbar$ per photon. The BG modes can thus be used as a basis to represent the quantum state of the two photons after SPDC. In the BG basis, one can write the state of the two photons produced by SPDC as [72]

$$|\Psi\rangle = \sum_\ell \iint a_\ell(k_{r1},k_{r2})|\ell,k_{r1}\rangle_s|-\ell,k_{r2}\rangle_i \mathrm{d}k_{r1}\mathrm{d}k_{r2}, \tag{5.5}$$

with $|a_\ell(k_{r1},k_{r2})|^2$ being the probability of measuring the signal and idler photons in the states $|\ell,k_{r1}\rangle_s$ and $|-\ell,k_{r2}\rangle_i$ respectively. In our experiment, we selected

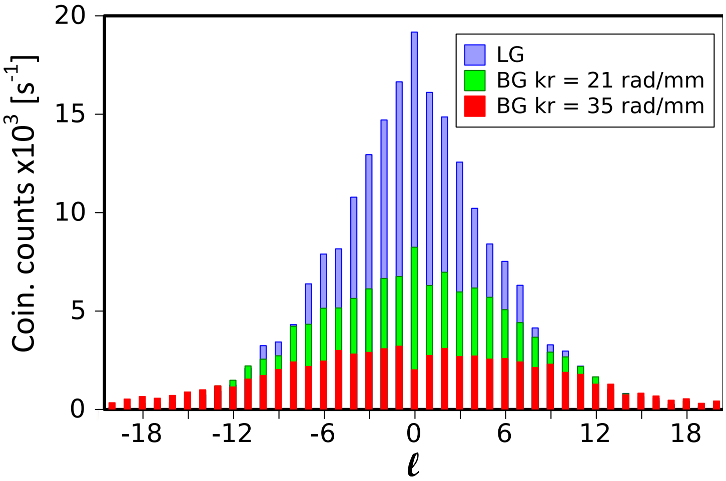

Figure 5.2: the OAM spectrum for LG modes (blue); for BG modes with k_r = 21 rad/mm (green) and for BG modes with $k_r = 35$ rad/mm (red).

a particular k_r value for both the signal and idler photons. We can thus write the state of the two photons as

$$|\Psi(k_r)\rangle = \sum_{\ell} a_\ell |\ell\rangle_s |-\ell\rangle_i \tag{5.6}$$

The motivation behind using the BG modes instead of LG modes is that BG modes have a broader and flatter OAM spectrum compared to LG modes [72]. This is illustrated in Fig. 5.2 where we plot the OAM spectrum for LG and BG modes on the same graph. The OAM spectrum is flatter for BG modes in the sense that the difference in the coincidence counts between $\ell = 0$ and the higher ℓ values is smaller for the BG modes compared to the LG modes. For instance, the difference in the number of counts between $\ell = 0$ and $\ell = 3$ is 66 counts for LG modes whereas it is 23 counts for BG with $k_r = 21$ rad/mm and 7 counts for BG with $k_r = 35$ rad/mm. Also, the difference in number of counts between $\ell = 0$ and $\ell = 5$ is 108 counts for LG modes whereas it is 26 counts for BG with $k_r = 21$rad/mm and 6 counts for BG with $k_r = 35$rad/mm. The flatness of the OAM spectrum plays an important role in the reconstruction of the density matrix representing the state of the two photons produced by SPDC. If we consider a state

$$|\Psi\rangle_{in} = \frac{1}{\sqrt{3}}(|\ell\rangle_A|{-\ell}\rangle_B + |0\rangle_A|0\rangle_B + |{-\ell}\rangle_A|\ell\rangle_B), \tag{5.7}$$

a big difference in the coincidence counts between the OAM values 0 and ℓ will lead to an inaccurate reconstruction of the density matrix. This is illustrated in Fig. 5.3, where we plot the density matrices describing the state of two qutrits represented by photons generated through SPDC for $\ell = 1, 3$ and 5 and for both LG and BG modes. One can see that the reconstructed density matrix becomes increasingly less accurate for LG modes as the value of ℓ is increased.

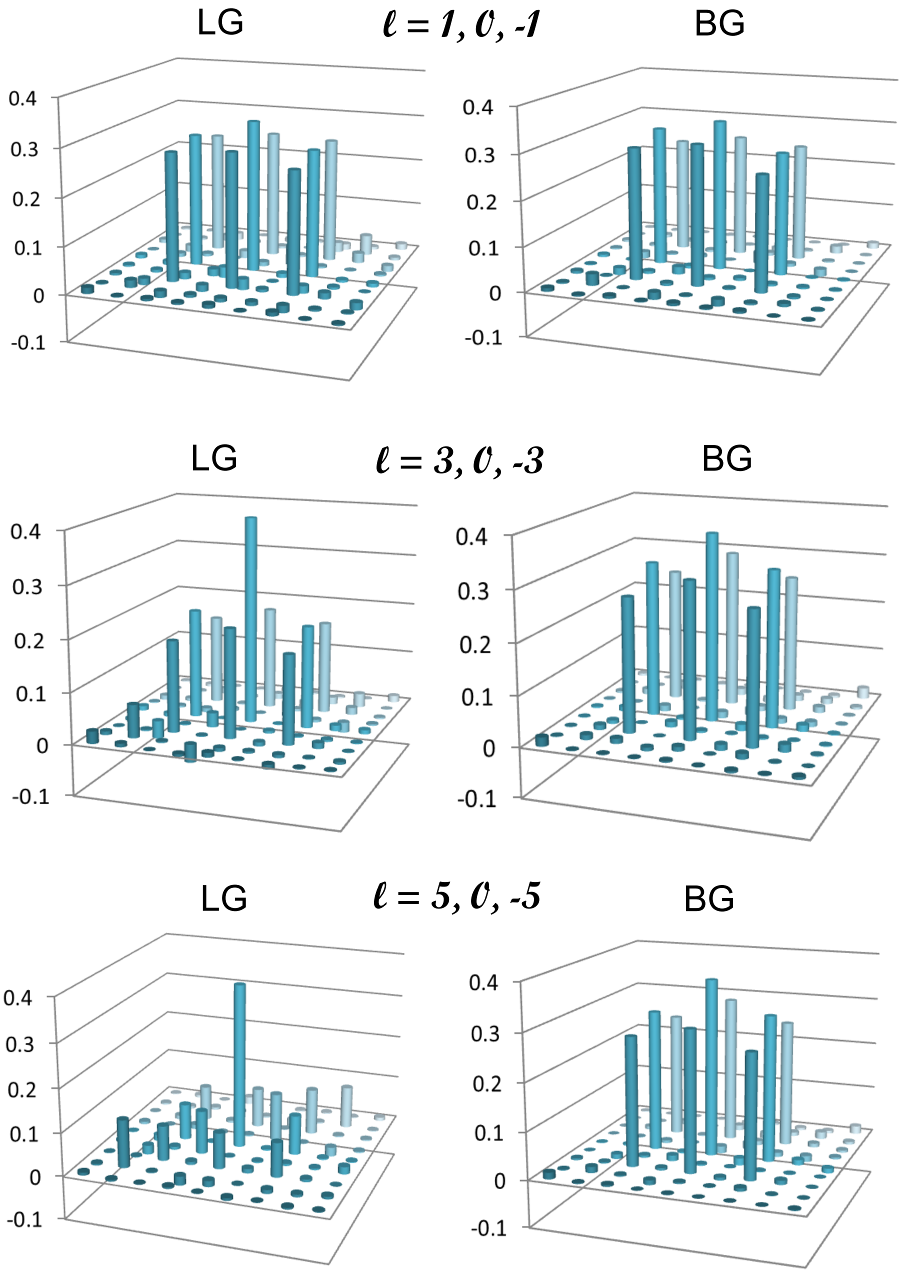

Figure 5.3: Real part of the density matrices describing the state of two qutrits represented by photons generated through SPDC for different ℓ values and both LG and BG modes. The x and y axis represent the basis vectors.

5.3 Numerical procedure

The numerical procedure is similar to that presented in Chapter 3 but adapted for the qutrit case. The initial state of the two qutrits is assumed to be the maximally entangled state given by Eq. (5.7). We consider $|\ell|$-values 1, 3 and 5. When photon A propagates in turbulence, its state will change as follows

$$\begin{aligned} |\ell\rangle_A &\rightarrow a_\ell|\ell\rangle_A + a_0|0\rangle_A + a_{-\ell}|-\ell\rangle_A \\ |0\rangle_A &\rightarrow e_\ell|\ell\rangle_A + e_0|0\rangle_A + e_{-\ell}|-\ell\rangle_A \\ |-\ell\rangle_A &\rightarrow c_\ell|\ell\rangle_A + c_0|0\rangle_A + c_{-\ell}|-\ell\rangle_A, \end{aligned}$$

where a_ℓ, a_0, etc. are the complex coefficients in the expansion of the distorted state in terms of the OAM basis.

After propagating through turbulence, the initial state in Eq. (5.7) will be transformed into

$$\begin{aligned} |\Psi\rangle_{in} \rightarrow |\Psi\rangle^{out} &= a_{-\ell}|-\ell\rangle|-\ell\rangle + a_\ell|\ell\rangle|-\ell\rangle + e_{-\ell}|-\ell\rangle|0\rangle + c_{-\ell}|-\ell\rangle|\ell\rangle \\ &\quad + a_0|0\rangle|-\ell\rangle + e_0|0\rangle|0\rangle + c_0|0\rangle|\ell\rangle + e_1|\ell\rangle|0\rangle + c_\ell|\ell\rangle|\ell\rangle. \end{aligned} \tag{5.8}$$

The state $|\Psi\rangle^{out}$ represents the state of the two qutrits for a specific instance of the turbulent medium. Because of the randomness of the medium, one has to compute the ensemble average of the density matrices over a representative set of instances of the medium as we did in the previous chapters. Then one gets

$$\rho = \frac{\sum_n^N |\Psi_n\rangle\langle\Psi_n|}{\mathrm{Tr}\left\{\sum_n^N |\Psi_n\rangle\langle\Psi_n|\right\}}, \tag{5.9}$$

where $|\Psi_n\rangle$ is the state of the qutrits after photon A propagates through the n^{th} phase screen (the n^{th} realisation of the turbulence medium).

5.4 Results and discussion

The value $k_r = 21$ rad/mm is used throughout the experiment. Figure 5.4 shows the evolution of the OAM entanglement between two qutrits initially in the state given in Eq. 5.7 as a function of the scintillation strength w_0/r_0 when one of the qutrits propagated through turbulence. The experimental and numerical results are plotted on the same graph for the different $|\ell|$-values considered. It can be observed from Fig. 5.4 that the experimental results agree within experimental error with the numerical results.

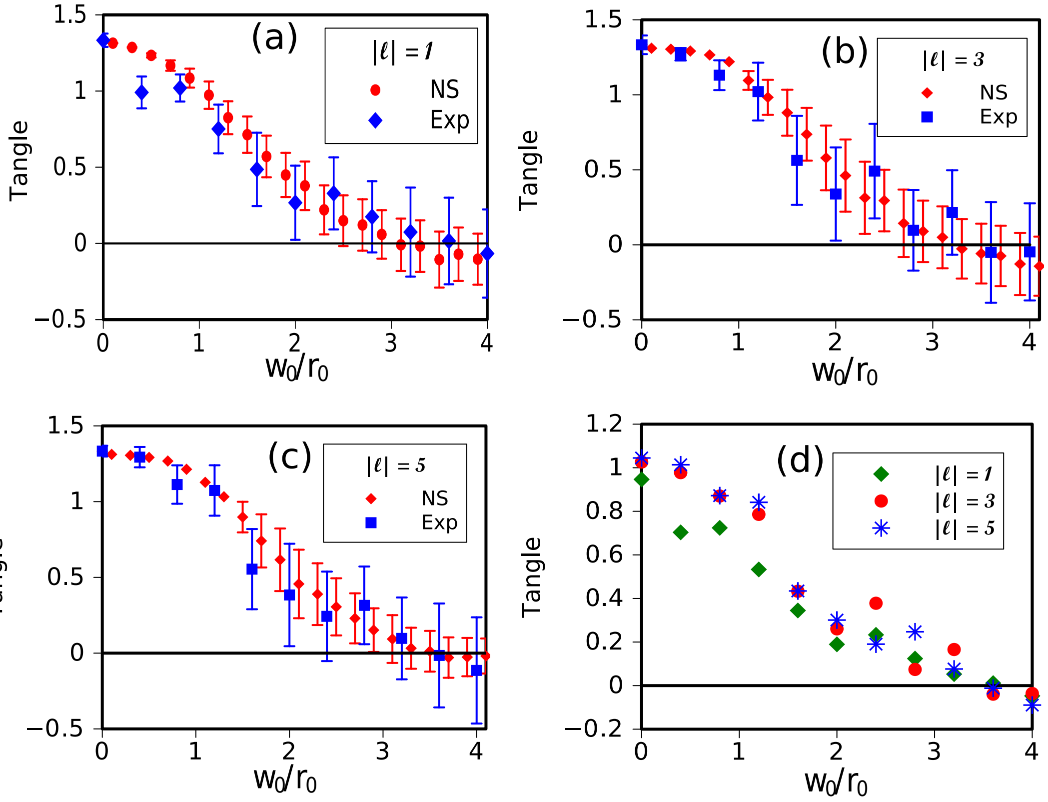

Figure 5.4: The tangle plotted against the scintillation strength (w_0/r_0) for both the experimental (Exp) and numerical (NS) results. (a): $\ell = 1$, (b): $\ell = 3$, (c): $\ell = 5$ and (d): plot of the experimental results for the different values of $|\ell|$ considered. The experimental results were normalised to start at 4/3 like the numerical curves.

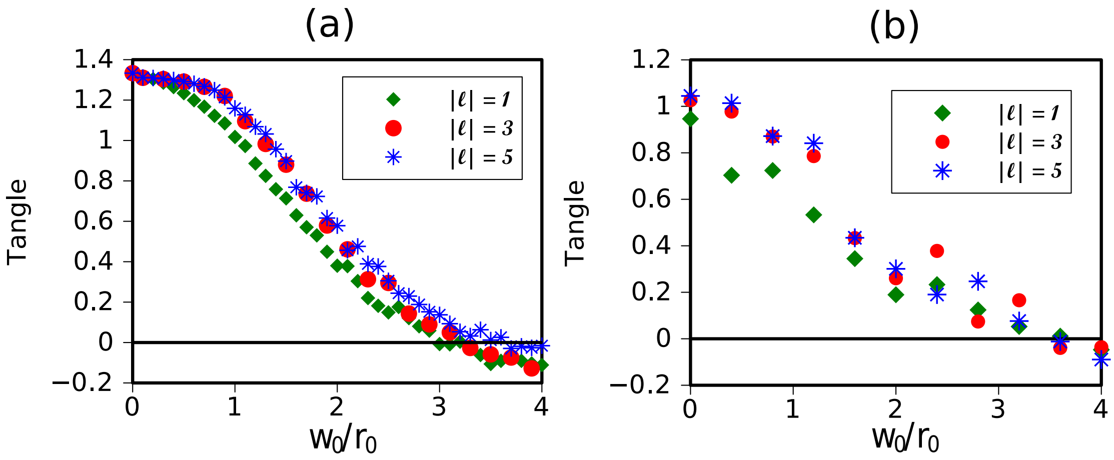

Figure 5.5: Numerical (a) and experimental (b) results of the evolution of the tangle between two qutrits against the scintillation strength for $|\ell| = 1, 3$ and 5.

The evolution of the entanglement between two qutrits is qualitatively similar to the evolution of entanglement between two qubits initially in a Bell state presented in the previous chapters. However, unlike what was observed in the qubit case, The experimental curves of the tangle corresponding to different $|\ell|$-values seem to lie on top of one another [Fig. 5.4(d)]. The numerical results also show that the curves of the tangle corresponding to $|\ell| = 3$ and 5 overlap, but the tangle decays slightly quicker when $|\ell| = 1$. This difference is more visible in Fig. 5.5 (a) (apart from the error bars) where we plot the numerical results for the evolution of the tangle between two qutrits on the same graph.

Compared to the results presented in chapters 3 and 4, the result presented in Fig. 5.4 suggest OAM entanglement between qutrits decays at an equal or faster rate compared to OAM entanglement between two qubits propagating in atmospheric turbulence.

5.5 Simulating down-converted photons with back-projected light

The experiment presented in this chapter is very time consuming. Because of the lack of an experimentally measurable entanglement measure for multidimensional quantum systems, one has to do a full quantum state tomography to reconstruct the density matrix describing the state of the two photons. The number of measurements needed for a full quantum state tomography increases exponentially with the dimension of the system. And because of the randomness of the atmosphere, one has to repeat these measurement a reasonable number of times and average the results to get a meaningful statistical description of the evolution of the entanglement.

In this section, we propose an experiment that can be used to mimic the down conversion experiment. We obtain similar results in significantly less time. The proposed experiment is based on the Klyshko picture [135]. If one considers a two photon state $|\psi\rangle$, then the probability of detecting the signal and idler in the state $|\psi\rangle_s$ and $|\psi\rangle_i$ respectively is given by

$$P(\psi_s, \psi_i) = |\langle\psi_i|\langle\psi_s|\psi\rangle|^2. \tag{5.10}$$

The joint detection probability $P(\psi_s, \psi_i)$ is the prediction of the measurement outcome according to quantum mechanics. It is proportional to the coincidence counts one would detect in a down-conversion experiment (like the one discribed in chapter 4 and section 5.2). The Klyshko picture is an approach that can be used to predict the measurement of the coincidence counts using “back-propagation” or back-projected light from one detector to the other and replacing the crystal with a mirror. This approach can only predict the coincidence accurately when the phase-matching condition is satisfied and when the pump beam can be considered to be a plane wave. The Klyshko picture can be used to verify the experimental procedure and to simulate down-converted photons classically [136, 137].

The experimental setup used to simulate the down-conversion experiment is presented in Fig. 5.6(b). That setup is almost identical to the original setup, with

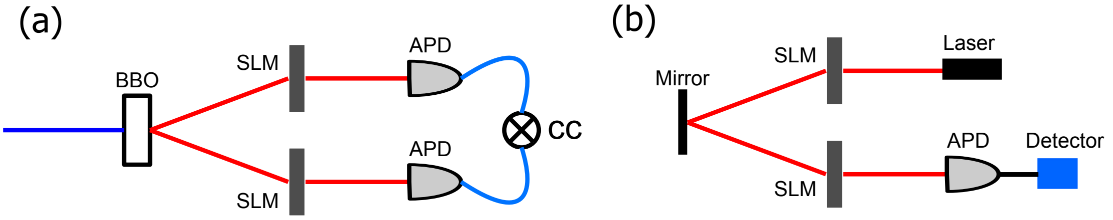

Figure 5.6: (a) Simplified diagram of the experimental setup used to detect the OAM eigenstates after SPDC.(b) Diagram of the setup used to simulate the down-conversion experiment with back projected classical light. One of the APDs is replaced with a diode laser at a wavelength of 710 nm and the BBO crystal with a mirror.

the difference that we replaced one of the APDs with a diode laser at a wavelength of 710 nm (equal to the wavelength of the downcoverted photons) and the BBO crystal with a mirror. The phase functions of the SLMs remained the same as in the original setup, and the random phase simulating the turbulence was added to the phase function of one of the SLMs. But now, because the back-projected light has many more photons, we do not need to undertake th measurement with a 10 second integration time, a 1 second integration time would suffice.

We do a full state tomography to reconstruct the density matrix describing the state of the two- qutrits. However, instead of using the coincidence counts as we did with down-converted photons, we used the number of single counts for each settings of the SLMs.

In Fig. 5.7, we compare the density matrices obtained through a full quantum state tomography to reconstruct the state of two maximally entangled qutrits in both the original down-conversion experiment and the classical experiment. It is clear from the plots of the density matrices that the back-projection experiment simulates the down-conversion experiment well.

Furthermore, a calculation of the fidelity, the linear entropy and the tangle suggest that the density matrices obtained in both experiments are identical and very close to the theoretical density matrix as can be seen in Table 5.1.

To further compare the two experiments, we study the evolution of the OAM

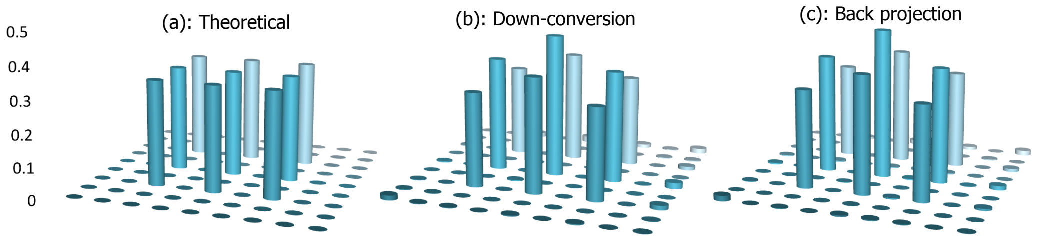

Figure 5.7: The real part density matrix representing the state of the two qutrits obtained from a full quantum state tomography. (a) theoretical density matrix, (b) density matrix obtain from down-converted photons, (c) density matrix obtain from back-projected classical light. The x and y axis represent the basis vectors

	ρ_{Theory}	$\rho_{Down-conversion}$	$\rho_{Back-projection}$
Fidelity	1	0.95 ± 0.01	0.93 ± 0.01
Linear entropy	0	0.01 ± 0.01	0.03 ± 0.01
Tangle	1.33	1.07 ± 0.02	0.95 ± 0.03

Table 5.1: Comparison of the fidelity, the linear entropy and the tangle for the theoretical density matrix and the matrices obtained in down-conversion and back-projection experiments.

entanglement between the two qutrits when one of the qubits propagates in turbulence while the other is left undisturbed. The result is presented in Fig. 5.8. Once again, the back projection experiment returns similar results as the down-conversion experiment.

Simulating the down-conversion experiment with back projected light has advantages. The most significant of these advantages is that it allows one to obtain results in much less time. For instance, to compute the curves for the evolution of the entanglement between two qutrits evolving in turbulence we considered 11 different strengths of turbulence and 30 realisations for each turbulence strength. We thus reconstructed 330 density matrices. A full quantum state tomography to reconstruct these matrices took a bit more than 8 days with a 10s integration time. The same results can be obtained with back-projected classical light in about 21 hours. This is because a 1 second integration time is sufficient in the

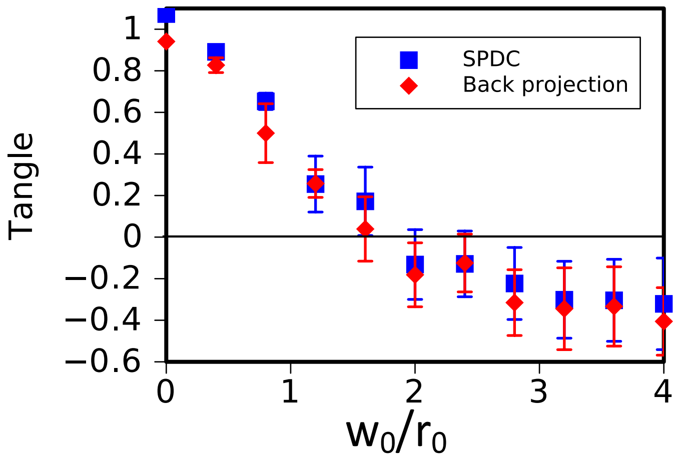

Figure 5.8: The tangle plotted against the scintillation strength w_0/r_0 for both the down-conversion experiment and the back projection experiment.

back projection experiment since the back-projected light has many more photons.

5.6 Conclusions

The evolution of the OAM entanglement between two qutrits was investigated numerically and experimentally when only one of the photons propagates through turbulence. The results obtained were compared with the numerical results based on the single phase screen approximation and with the results previously obtained in the qubit case. The curves of the tangle suggest that OAM entanglement between qutrits decays at an equal or faster rate compared to OAM entanglement between qubits. This supports the conclusions reached in the previous chapter, namely that the OAM state of light might not be a suitable candidate for free-space quantum communication with multidimensional entangled states. However, there are ways in which one can improve the maximum distance over which one can propagate OAM entangled photons and still have a useful amount of entanglement between them. For instance, one can use the most robust initial states [138] to encode information before sending it through the free-space channel. These are states that are least affected by turbulence. Alternatively, one can use adaptive optics to correct for the aberrations caused by turbulence. This technique has already been used to correct for the channel crosstalk between OAM channels [82, 139].

we also presented an experiment that simulates down-converted photons with back-projected classical light. The results obtained were similar to those produced by the down-conversion experiment.

Chapter 6

Conclusion and future work

A literature review was presented in chapter 1 giving the historical background and the current state of research on the effects of the atmospheric turbulence on the OAM state of light. Our objectives and motivations for the current work were also presented in that chapter. We next presented the theoretical background that will be used in the current work in chapter 2.

Our first objective was to verify the analytical work by Smith and Raymer [84], we did that in chapter 3, where we presented a numerical study of the evolution of OAM entanglement between a pair of photons propagating through atmospheric turbulence modelled by a single phase screen. Different values of the OAM index were considered. It was found that the entanglement of states with larger OAM values took more time to decay, suggesting that states with larger OAM values will be more suitable for free-space quantum communication. On the other hand, it was observed that modes with larger OAM values are scattered more rapidly into higher order modes. Our results agreed with what was found by S&R [84]. We further derived an expression for the scale distance at which entanglement decays as a function of ℓ. This expression can be used to find the maximum distance over which OAM-entangled photons propagate before they lose their entanglement.

Our second goal was to have a more realistic model of the turbulence by going beyond the single phase screen approximation since this approximation is only valid in the weak fluctuation regime. We thus presented in the second part of chapter 3 a numerical simulation of the evolution of OAM entanglement in turbulence modelled by a series of consecutive phase screens. It was found that the evolution of OAM entanglement cannot always be described only by the dimensionless parameter w_0/r_0. In certain regimes, two parameters are required to describe the evolution of the OAM entanglement in turbulence; one being the normalised propagation distance (t) and another which is independent of the propagation distance (K). This confirmed the predictions of the IPE [90].

Our third objective was to present an experimental study directly considering the evolution of OAM entanglement between two qubits evolving in atmospheric turbulence. In order to compare our work with that of S&R, we simulated the atmospheric turbulence with a single phase screen placed on a SLM. We considered modes with $|\ell|$-values 1,3, 5 and 7 and we related our results with the numerical results presented in Chapter 3, the S&R [84] and the IPE [90]. We considered two different scenarios: the case where only one of the two photons is propagated through turbulence and the case where both photons are propagated through turbulence. In both these scenarios, our results agreed with the numerical results and the S&R theory and suggest that modes with higher $|\ell|$-values are more robust in turbulence and could thus give an advantage in a free-space quantum communication system. Our results disagreed with the IPE when $\ell = 3, 5$ and 7. The reason for this could be the fact that the IPE doesn't take into account the effects of cross-correlation between modes with different ℓ-values.

In chapter 5 we addressed our fourth objective, that is, we presented a theoretical and experimental study of the evolution of OAM entanglement between two qutrits when only one of the qutrits propagates through turbulence. The results obtained were compared with the numerical results based on the single phase screen approximation and with the results previously obtained in the qubit case. Our results suggested that OAM entanglement between qutrits decays at an equal or faster rate compared to OAM entanglement between qubits. This supports the conclusion that the OAM states of light might not be a suitable candidate for free-space quantum communication with multidimensional entangled states.

An experiment that simulates down-converted photons with back-projected classical light was also presented in chapter 5. Results similar to those obtained with down-converted photons were achieved in significantly less time.

There still remains much to be done on the evolution of OAM entanglement in turbulence. For instance, we ignored the radial index p of LG modes that we considered in this work. It might be interesting to study how the atmospheric turbulence affects the OAM entanglement in LG modes with non-zero p.

All the results we presented suggest that photonic OAM might not be a suitable candidate for long distance free-space quantum communication because the OAM entanglement decays rather quickly in turbulence. However, there are ways in which one can improve the maximum distance over which one can propagate OAM entangled photons and still have a useful amount of entanglement between them. For instance, one can use the most robust initial states [138] to encode information before sending it through the free-space channel. These are states that are least affected by turbulence. Alternatively, one can use adaptive optics to correct for the aberrations caused by turbulence. This technique has already been used to correct for the channel crosstalk between OAM channels [82,139]. It might be worthwhile to study the extend to which the combination of the most robust initial state and adaptive optics can improve the distance scale of entanglement decay.

We simulated atmospheric turbulence with a single phase screen based on the Kolmogorov theory of turbulence in all the experiments presented in this thesis. We did so because we wanted to test the S&R analytical study. Furthermore, this is the simplest method one can use to simulate turbulence. However, the single phase screen approximation can only model turbulence in the weak fluctuation regime. The next step will be to consider a more realistic model of real turbulence, like a turbulence pipe for example. This is a device that simulates turbulence by mixing cold and hot air. Eventually, one would need to do the experiment with real turbulence but it is imperative to find efficient ways of improving the distance scale of entanglement decay beforehand.

Appendix A: Calculation of the error bars for the concurrence obtained from the experimental and numerical results

The idea is to use the Bloch representation of the density matrix; this is because the Bloch coefficients are real unlike the elements of the density matrix. In this calculation we assume that the Bloch coefficients are statistically independent.

The density matrix ρ can be written in the Bloch representation as

$$\rho = \sum_{i,j}^{16} B_{ij} \sigma_i \otimes \sigma_j, \tag{1}$$

where the B_{ij} are the Bloch coefficients.

The concurrence is a function of the eigenvalues of the matrix $R = \rho\tilde{\rho}$ where $\tilde{\rho} = \sigma_y \otimes \sigma_y \rho^* \sigma_y \otimes \sigma_y$ [122]. The matrix R can be written in the Bloch representation as

$$\begin{aligned} R &= \sum_{ijkl}^{16} B_{ij} B_{kl} (\sigma_i \otimes \sigma_j)(\sigma_y \otimes \sigma_y)(\sigma_i^* \otimes \sigma_j^*)(\sigma_y \otimes \sigma_y) \\ &= \sum_{ijkl}^{16} B_{ij} B_{kl} \Gamma_{ijkl}, \end{aligned} \tag{2}$$

where $\Gamma_{ijkl} = \sigma_i \sigma_y \sigma_k^* \sigma_y \otimes \sigma_j \sigma_y \sigma_l^* \sigma_y$.

We calculate the error in R by propagating the errors associated with the Bloch coefficients B_{ij}, and the error associated with the Bloch coefficients is given by

$$\Delta B = \sqrt{\langle B \rangle^2 - \langle B^2 \rangle}. \tag{3}$$

Here, B is a 4×4 matrix containing the coefficients B_{ij} and B^2 is obtained by squaring the elements of B.

Since we assumed that the B_i are statistically independent, we need to calculate their independent contribution to the error in R. Thus the error in the matrix R due to the Bloch coefficients B_{mn} (m, $n = 0$ to 4) is given by [140]

$$\begin{aligned}\Delta R &= \frac{\partial R}{\partial B_{mn}} \Delta B_{mn} \\ &= \sum_{ijklmn}^{4} \left\{ \frac{\partial B_{ij}}{\partial B_{mn}} \Delta B_{mn} B_{kl} \Gamma_{ijkl} + B_{ij} \frac{\partial B_{kl}}{\partial B_{mn}} \Delta B_{mn} \Gamma_{ijkl} \right\} \\ &= \sum_{ijklmn}^{4} \Delta B_{mn} B_{kl} \Gamma_{nmkl} + \Delta B_{mn} B_{ij} \Gamma_{ijmn}. \end{aligned} \tag{4}$$

To get the previous results, we used the chain rule on Eq. 2 and the fact that $\partial B_{xy}/\partial B_{mn} = 1$ if $xy = mn$ or zero otherwise.

The error in the eigenvalues of R are obtained by propagating the error in the R. The error in the eigenvalue λ_n is given by

$$\Delta \lambda_n = V_n^\dagger \Delta R V_n, \tag{5}$$

where λ_n is the n^{th} eigenvalue with corresponding eigenvector V_n.

Finally, the error in the concurrence is given by [140]

$$\begin{aligned}\Delta \mathcal{C} &= \sqrt{\sum_{i}^{4} \frac{\partial \mathcal{C}}{\partial \lambda_i} \Delta \lambda_i} \\ &= \frac{1}{2} \left[\left(\frac{\Delta \lambda_1}{\sqrt{\lambda_1}} \right)^2 + \left(\frac{\Delta \lambda_2}{\sqrt{\lambda_2}} \right)^2 + \left(\frac{\Delta \lambda_3}{\sqrt{\lambda_3}} \right)^2 + \left(\frac{\Delta \lambda_4}{\sqrt{\lambda_4}} \right)^2 \right]^{1/2}. \end{aligned} \tag{6}$$

Bibliography

[1] J. Maxwell, *A Treatise on Electricity and Magnetism.* Oxford: Clarendon Press, 1891.

[2] J. H. Poynting, “On the transfer of energy in the electromagnetic field,” *Phil. Trans.*, vol. 174, p. 343, 1884.

[3] J. H. Poynting, “The wave motion of a revolving shaft, and a suggestion as to the angular momentum in a beam of circularly polarised light,” *Proc. Roy. Soc. A*, vol. 82, p. 560, 1909.

[4] R. A. Beth, “Mechanical detection and measurement of the angular momentum of light,” *Phys. Rev.*, vol. 50, pp. 115–125, Jul 1936.

[5] L. Mandel and E. Wolf, *Optical Coherence and Quantum Optics.* Cambridge: Cambridge University Press, 1995.

[6] J. D. Jackson, *Classical Electrodynamics.* New York: Wiley, 3rd ed., 1999.

[7] D. J. Griffiths, *Introduction to Electrodynamics.* New Jersey: Prentice Hall, 3rd ed., 1999.

[8] C. J. Bouwkamp and H. B. G. Casimir, “On multipole expansions in the theory of electromagnetic radiation,” *Physica*, vol. 20, p. 539, 1954.

[9] M. E. Rose, *Multipole Fields.* Wiley, New York, 1955.

[10] C. G. Darwin, “Notes on the theory of radiation. , 136(829):36 52, 1932.,” *Proc. R. Soc. Lond. A*, vol. 136, pp. 36–52, 1932.

[11] L. Allen, M. W. Beijersbergen, R. J. C. Spreeuw, and J. P. Woerdman, “Orbital angular momentum of light and the transformation of laguerre-gaussian laser mode,” *Phys. Rev. A*, vol. 45, pp. 8185–8189, 1992.

[12] M. W. Beijersbergen, L. Allen, H. E. L. O. Van der Veen, and J. P. Woerdman, “Astigmatic laser mode converters and transfer of orbital angular momentum,” *Opt. Commun.*, vol. 96, pp. 123–132, 1993.

[13] M. W. Beijersbergen, R. P. C. Coerwinkel, M. Kristensen, and J. P. Woerdman, “Helical-wavefront laser beams produced with a spiral phaseplate,” *Optics Communications*, vol. 112, pp. 321–327, 1994.

[14] L. Marrucci, C. Manzo, and D. Paparo, “Optical spin-to-orbital angular momentum conversion in inhomogeneous anisotropic media,” *Phys. Rev. Lett.*, vol. 96, p. 163905, Apr 2006.

[15] E. Karimi, B. Piccirillo, E. Nagali, L. Marrucci, and E. Santamato, “Efficient generation and sorting of orbital angular momentum eigenmodes of light by thermally tuned q-plates,” *Appl. Phys. Lett.*, vol. 94, p. 231124, 2009.

[16] V. Y. Bazhenov, M. V. . Vasnetsov, and M. S. Soskin, “Laser beams with screw dislocations in their wavefronts,” *JETP Lett.*, vol. 52, 1990.

[17] N. R. Heckenberg, R. McDuff, C. P. Smith, H. Rubinsztein-Dunlop, and M. J. Wegener, “Laser beams with phase singularities,” *Optical and Quantum Electronics*, vol. 29, pp. S951–S962, 1992.

[18] M. S. Soskin, V. N. Gorshkov, M. V. Vasnetsov, J. T. Malos, and N. R. Heckenberg, “Topological charge and angular momentum of light beams carrying optical vortices,” *Phys. Rev. A*, vol. 56, pp. 4064–4075, Nov 1997.

[19] J. E. Curtis, B. A. Koss, and D. G. Grier, “Dynamic holographic optical tweezers,” *Opt. Commun.*, vol. 207, p. 169, 2002.

[20] D. McGloin and K. Dholakia, "Bessel beam: diffraction in a new light," *Contemporary Physics*, vol. 46, pp. 15 – 28, 2005.

[21] F. Gori, G. Guattari, and C. Padovani, "Bessel-gauss beams," *Opt. Commun.*, vol. 64, pp. 491 – 495, 1987.

[22] J. Gutierrez-Vega, M. Iturbe-Castillo, and S. Chavez-Cerda, "Alternative formulation for invariant optical fields: Mathieu beams," *Opt. Lett.*, vol. 25, pp. 1493 – 1495, 2000.

[23] M. A. Bandres and J. C. Gutirrez-Vega, "Ince-Gaussian beams," *Opt. Lett.*, vol. 29, pp. 144 – 146, 2004.

[24] H. He, M. E. J. Friese, N. R. Heckenberg, and H. Rubinsztein-Dunlop, "Direct observation of transfer of angular momentum of absorptive particles from a laser beam with a phase singularity," *Phys. Rev. Lett.*, vol. 75, pp. 826–829, 1995.

[25] H. He, N. Heckenberg, and H. Rubinsztein-Dunlop, "Optical particle trapping with higher-order doughnut beams produced using high efficiency computer generated holograms," *J. Mod. Opt.*, vol. 42, p. 217, 1995.

[26] M. E. J. Friese, T. A. Nieminen, N. R. Heckenberg, and H. Rubinsztein-Dunlop, "Optical alignment and spinning of laser-trapped microscopic particles," *Nature*, vol. 394, p. 348, 1998.

[27] N. B. Simpson, K. Dholakia, L. Allen, and M. J. Padgett, "Mechanical equivalence of spin and orbital angular momentum of light: an optical spanner," *Opt. Lett.*, vol. 22, pp. 52 – 54, 1997.

[28] M. Friese, H. Rubinsztein-Dunlop, J. Gold, P. Hagberg, and D. Hanstorp, "Optically driven micromachine elements," *Appl. Phys. Lett.*, vol. 78, pp. 547 – 549, 2001.

[29] P. Galajda and P. Ormos, "Complex micromachines produced and driven by light," *Appl. Phys. Lett.*, vol. 78, p. 249, 2001.

[30] J. Leach, H. Mushfique, R. di Leonardo, M. Padgett, and J. Cooper, “An optically driven pump for microfluidics,” *Lab Chip*, vol. 6, p. 735, 2006.

[31] K. Ladavac and D. G. Grier, “Microoptomechanical pumps assembled and driven by holographic optical vortex arrays,” *Opt. Express*, vol. 12, pp. 1144 – 1149, 2004.

[32] S. W. Hell, “Toward fluorescence nanoscopy,” *Nature Biotechnol.*, vol. 21, pp. 1347 – 1355, 2003.

[33] L. Torner and J. P. Torres, “Digital spiral imaging and silvia carrasco,” *Opt. Express*, vol. 13, p. 873, 2005.

[34] S. Bernet, A. Jesacher, S. Frhapter, C. Maurer, and M. Ritsch-Marte, “Quantitative imaging of complex samples by spiral phase contrast microscopy,” *Opt. E*, vol. 14, pp. 3792 – 3805, 2006.

[35] G. Swartzlander, “The optical vortex lens,” *Opt. Photon. News*, vol. 17, pp. 39 – 43, 2006.

[36] H. Bechmann-Pasquinucci and W. Tittel, “Quantum cryptography using larger alphabets,” *Phys. Rev. A*, vol. 61, p. 062308, May 2000.

[37] R. W. Boyd, A. Jha, M. Malik, C. O’Sullivan, B. Rodenburg, and D. J. Gauthier, “Quantum key distribution in a high-dimensional state space: Exploiting the transverse degree of freedom of the photon,” in *Proc. of SPIE Vol. 7948 79480L*, 2011.

[38] S. P. Walborn, D. S. Lemelle, M. P. Almeida, and P. H. S. Ribeiro, “Quantum key distribution with higher-order alphabets using spatially encoded qudits,” *Phys. Rev. Lett.*, vol. 96, p. 090501, Mar 2006.

[39] P. B. Dixon, G. A. Howland, J. Schneeloch, and J. C. Howell, “Quantum mutual information capacity for high-dimensional entangled states,” *Phys. Rev. Lett.*, vol. 108, p. 143603, Apr 2012.

[40] G. Gibson, J. Courtial, and M. J. Padgett, “Free-space information transfer using light beams carrying orbital angular momentum,” *Opt. Express*, vol. 12, pp. 5448 – 5456, 2004.

[41] C. Paterson, “Atmospheric turbulence and orbital angular momentum of single photons for optical communication,” *Phys. Rev. Lett.*, vol. 94, p. 153901, 2005.

[42] G. Molina-Terriza, J. P. Torres, and L. Torner, “Twisted photons,” *Nature Physics*, vol. 3, pp. 305 – 310, 2007.

[43] A. C. Dada, J. Leach, G. S. Buller, M. J. Padgett, and E. Andersson, “Experimental high-dimensional two-photon entanglement and violations of generalized bell inequalities,” *Nature Physics*, vol. 7, pp. 677 – 680, 2011.

[44] M. H. Ryszard Horodecki, Pawel. Horodecki and K. Horodecki, “Quantum entanglement,” *Rev. Mod. Phys.*, vol. 81, pp. 865 – 942, 2009.

[45] M. Genovese, “Research on hidden variable theories: a review of recent progresses,” *Phys. Rep.*, vol. 413, pp. 319 – 396, 2005.

[46] E. Schrödinger *Naturwissenschaften*, vol. 23, pp. 807 – 812, 1935.

[47] A. Einstein, B. Podolsky, and N. Rosen, “Can quantum-mechanical description of physical reality be considered complete?,” *Phys. Rev.*, vol. 47, pp. 777–780, May 1935.

[48] J. S. Bell, “On the Einstein-Podolsky-Rosen Paradox,” *Physics*, vol. 1, pp. 195 – 200, 1964.

[49] J. S. Bell, *Speakable and unspeakable in quantum mechanics.* Cambridge University Press, 1987.

[50] S. J. Freedman and J. F. Clauser, “Experimental test of local hidden-variable theories,” *Phys. Rev. Lett.*, vol. 28, pp. 938–941, Apr 1972.

[51] M. A. Nielsen and I. L. Chuang, *Quantum Computation and Quantum Information.* Cambridge: Cambridge University Press, 2000.

[52] C. H. Bennett, G. Brassard, C. Crépeau, R. Jozsa, A. Peres, and W. K. Wootters, "Teleporting an unknown quantum state via dual classical and Einstein-Podolsky-Rosen channels," *Phys. Rev. Lett.*, vol. 70, pp. 1895–1899, Mar 1993.

[53] A. Ekert and R. Jozsa, "Quantum computation and shor's factoring algorithm," *Rev. Mod. Phys.*, vol. 68, pp. 733–753, Jul 1996.

[54] V. Giovannetti, S. Lloyd, and L.Maccone, "Quantum-enhanced measurements: beating the standard quantum limit," *Science*, vol. 306, p. 1330, 2004.

[55] C. H. Bennett and S. J. Wiesner, "Communication via one- and two-particle operators on Einstein-Podolsky-Rosen states," *Phys. Rev. Lett.*, vol. 69, pp. 2881–2884, Nov 1992.

[56] A. K. Ekert, "Quantum cryptography based on bell's theorem," *Phys. Rev. Lett.*, vol. 67, pp. 661–663, Aug 1991.

[57] J. T. Barreiro, T.-C. Wei, and P. G. Kwiat, "Beating the channel capacity limit for linear photonic superdense coding," *Nat. Phys.*, vol. 4, p. 282, 2008.

[58] S. P. Walborn, D. S. Lemelle, M. P. Almeida, and P. H. S. Ribeiro, "Quantum key distribution with higher-order alphabets using spatially encoded qudits," *Phys. Rev. Lett.*, vol. 96, p. 090501, Mar 2006.

[59] H. Bechmann-Pasquinucci and A. Peres, "Quantum cryptography with 3-state systems," *Phys. Rev. Lett.*, vol. 85, pp. 3313–3316, Oct 2000.

[60] H. Bechmann-Pasquinucci and W. Tittel, "Quantum cryptography using larger alphabets," *Phys. Rev. A*, vol. 61, p. 062308, May 2000.

[61] T. Vértesi, S. Pironio, and N. Brunner, “Closing the detection loophole in bell experiments using qudits,” *Phys. Rev. Lett.*, vol. 104, p. 060401, Feb 2010.

[62] D. Collins, N. Gisin, N. Linden, S. Massar, and S. Popescu, “Bell inequalities for arbitrarily high-dimensional systems,” *Phys. Rev. Lett.*, vol. 88, p. 040404, Jan 2002.

[63] L. Olislager, J. Cussey, A. T. Nguyen, P. Emplit, S. Massar, J.-M. Merolla, and K. P. Huy, “Frequency-bin entangled photons,” *Phys. Rev. A*, vol. 82, p. 013804, Jul 2010.

[64] H. de Riedmatten, I.Marcikic, H. Zbinden, and N. Gisin, “Creating high dimensional entanglement using mode-locked lasers,” *Quant. Inf. Comp.*, vol. 2, p. 425, 2002.

[65] R. T. Thew, A. Acín, H. Zbinden, and N. Gisin, “Bell-type test of energy-time entangled qutrits,” *Phys. Rev. Lett.*, vol. 93, p. 010503, Jul 2004.

[66] L. Neves, G. Lima, J. G. Aguirre Gómez, C. H. Monken, C. Saavedra, and S. Pádua, “Generation of entangled states of qudits using twin photons,” *Phys. Rev. Lett.*, vol. 94, p. 100501, Mar 2005.

[67] M. N. O’Sullivan-Hale, I. Ali Khan, R. W. Boyd, and J. C. Howell, “Pixel entanglement: Experimental realization of optically entangled $d = 3$ and $d = 6$ qudits,” *Phys. Rev. Lett.*, vol. 94, p. 220501, Jun 2005.

[68] T. Yarnall, A. F. Abouraddy, B. E. A. Saleh, and M. C. Teich, “Experimental violation of bell’s inequality in spatial-parity space,” *Phys. Rev. Lett.*, vol. 99, p. 170408, Oct 2007.

[69] J. T. Barreiro, N. K. Langford, N. A. Peters, and P. G. Kwiat, “Generation of hyperentangled photon pairs,” *Phys. Rev. Lett.*, vol. 95, p. 260501, Dec 2005.

[70] G. Vallone, R. Ceccarelli, F. De Martini, and P. Mataloni, "Hyperentanglement of two photons in three degrees of freedom," *Phys. Rev. A*, vol. 79, p. 030301, Mar 2009.

[71] W.-B. Gao, C.-Y. Lu, X.-C. Yao, P. Xu, O. Guhne, A. Goebel, Y.-A. Chen, C.-Z. Peng, Z.-B. Chen, and J.-W. Pan, "Experimental demonstration of a hyper-entangled ten-qubit schrodinger cat state," *Nat. Phys.*, vol. 6, p. 331, 2010.

[72] M. McLaren, M. Agnew, J. Leach, F. S. Roux, M. J. Padgett, R. W. Boyd, and A. Forbes, "Entangled bessel-gaussian beams," *Opt. Express*, vol. 20, pp. 23589–23597, 2012.

[73] C. Bennett and G. Brassard, "Quantum cryptography: Public key distribution and coin tossing," in *Proceedings of IEEE Inter- national Conference on Computers, Systems and Signal Processing, Bangalore, India (IEEE, New York, 1984) pp. 175179.*, 1984.

[74] N. Gisin, G. Ribordy, W. Tittel, and H. Zbinden, "Quantum cryptography," *Rev. Mod. Phys.*, vol. 74, pp. 145–195, Mar 2002.

[75] N. Gisin and R. Thew, "Quantum communication," *Nature Photonics*, vol. 1, p. 165, 2007.

[76] V. Scarani, H. Bechmann-Pasquinucci, N. J. Cerf, M. Dusek, N. Lutkenhaus, and M. Peev, "The security of practical quantum key distribution," *Rev. Mod. Phys.*, vol. 81, pp. 1301 – 1350, 2009.

[77] G. A. Tyler and R. W. Boyd, "Influence of atmospheric turbulence on the propagation of quantum states of light carrying orbital angular momentum," *Opt. Lett.*, vol. 34, pp. 142–144, 2009.

[78] D. L. Fried, "Optical resolution through a random inhomogeneous medium for very long and very short exposures," *J. Opt. Soc. Am.*, vol. 56, pp. 1372–1379, 1966.

[79] C. Gopaul and R. Andrews, “The effect of atmospheric turbulence on entangled orbital angular momentum states,” *New J. Phys.*, vol. 9, p. 94, 2007.

[80] M. Malik, M. OSullivan, B. Rodenburg, M. Mirhosseini, J. Leach, M. P. J. Lavery, M. J. Padgett, and R. W. Boyd, “Influence of atmospheric turbulence on optical communications using orbital angular momentum for encoding,” *Opt. Express*, vol. 20, p. 13195, 2012.

[81] B. Rodenburg, M. P. J. Lavery, M. Malik, M. N. OSullivan, M. Mirhosseini, D. J. Robertson, M. Padgett, and R. W. Boyd, “Influence of atmospheric turbulence on states of light carrying orbital angular momentum,” *Opt. Lett.*, vol. 37, p. 3735, 2012.

[82] B. Rodenburg, M. Mirhosseini, M. Malik, M. Yanakas, L. Maher, N. K. Steinhoff, G. A. Tyler, and R. W. Boyd, “Simulating real-world turbulence in the lab: orbital angular momentum communication through 1 km of atmosphere,” *ArXiv:1301.7454v1*, 2013.

[83] B.-J. Pors, C. H. Monken, E. R. Eliel, and J. P. Woerdman, “Transport of orbital-angular-momentum entanglement through a turbulent atmosphere,” *Opt. Express*, vol. 19, pp. 6671–6683, 2011.

[84] B. J. Smith and M. G. Raymer, “Two-photon wave mechanics,” *Phys. Rev. A*, vol. 74, p. 062104, 2006.

[85] S. M. Wandzura, “Meaning of quadratic structure functions,” *J. Opt. Soc. Am.*, vol. 70, pp. 745–747, 1980.

[86] L. C. Andrews and R. L. Phillips, *Laser Beam Propagation Through Random Media.* Washington: SPIE, 1998.

[87] J. M. Martin and S. M. Flatté, “Intensity images and statistics from numerical simulation of wave propagation in 3-d random media,” *Appl. Opt.*, vol. 27, pp. 2111–2126, 1988.

[88] J. M. Martin and S. M. Flatté, "Simulation of point-source scintillation through three-dimensional random media," *J. Opt. Soc. Am. A*, vol. 7, pp. 838–847, 1990.

[89] J. A. Anguita, M. A. Neifeld, and B. V. Vasic, "Turbulence-induced channel crosstalk in an orbital angular momentum-multiplexed free-space optical link," *Appl. Opt.*, vol. 47, 2008.

[90] F. S. Roux, "Infinitesimal-propagation equation for decoherence of an orbital-angular-momentum-entangled biphoton state in atmospheric turbulence," *Phys. Rev. A*, vol. 83, p. 053822, 2011.

[91] D. L. Andrews and M. Babiker, eds., *The Angular Momentum of Light.* Cambridge University Press, 2013.

[92] A. T. O'Neil, I. MacVicar, L. Allen, and M. J. Padgett, "Intrinsic and extrinsic nature of the orbital angular momentum of a light beam," *Phys. Rev. Lett.*, vol. 88, p. 053601, Jan 2002.

[93] L. Allen and M. J. Padgett, "The Poynting vector of Laguerre-Gaussian beams and the interpretation of thier angular momentum density," *Opt. Commun.*, vol. 184, 2000.

[94] M. I. Kolobov, ed., *Quantum Imaging.* Springer, 2007.

[95] A. E. Siegman, *Lasers.* University Science Books, 1986.

[96] A. M. Yao and M. J. Padgett, "Orbital angular momentum: origins, behavior and applications," *Advances in Optics and Photonics*, vol. 3, p. 161?204, 2011.

[97] J. Durnin, J. J. Miceli, and J. H. Eberly, "Diffraction-free beams," *Phys. Rev. Lett.*, vol. 58, pp. 1499–1501, Apr 1987.

[98] A. Aspect, P. Grangier, and G. Roger, "Experimental tests of realistic local theories via bell's theorem," *Phys. Rev. Lett.*, vol. 47, pp. 460–463, Aug 1981.

[99] A. Aspect, J. Dalibard, and G. Roger, “Experimental test of bell’s inequalities using time- varying analyzers,” *Phys. Rev. Lett.*, vol. 49, pp. 1804–1807, Dec 1982.

[100] R. Boyd, *Nonlinear Optics.* Electronics & Electrical, Acad. Press, 2003.

[101] C. Gerry and P. Knight, *Introductory Quantum Optics.* Cambridge University Press, 2005.

[102] Y. H. Shih and C. O. Alley, “New type of Einstein-Podolsky-Rosen-Bohm experiment using pairs of light quanta produced by optical parametric down conversion,” *Phys. Rev. Lett.*, vol. 61, pp. 2921–2924, Dec 1988.

[103] A. Mair, A. Vaziri, G. Weihs, and A. Zeilinger, “Entanglement of the orbital angular momentum states of photons,” *Nature*, vol. 412, p. 313, 2001.

[104] S. P. Walborn, A. N. de Oliveira, S. Pádua, and C. H. Monken, “Multimode hong-ou-mandel interference,” *Phys. Rev. Lett.*, vol. 90, p. 143601, Apr 2003.

[105] K. W. Chan, J. P. Torres, and J. H. Eberly, “Transverse entanglement migration in hilbert space,” *Phys. Rev. A*, vol. 75, p. 050101, May 2007.

[106] J. P. Torres and L. Torner, eds., *Chapter 11 in Twisted Photons.* WILEY-VCH Verlag & Co. KGaA, 2011.

[107] C. K. Law, I. A. Walmsley, and J. H. Eberly, “Continuous frequency entanglement: Effective finite hilbert space and entropy control,” *Phys. Rev. Lett.*, vol. 84, pp. 5304–5307, Jun 2000.

[108] F. Miatto, T. Brougham, and A. Yao, “Cartesian and polar schmidt bases for down-converted photons,” *Eur. Phys. J. D*, vol. 66, p. 183, 2012.

[109] K. Vogel and H. Risken, “Determination of quasiprobability distributions in terms of probability distributions for the rotated quadrature phase,” *Phys. Rev. A*, vol. 40, pp. 2847–2849, 1989.

[110] U. Leonhardt, *Measuring the Quantum State of Light.* New York: Cambridge University Press, 1997.

[111] Z. Hradil, "Quantum-state estimation," *Phys. Rev. A*, vol. 55, pp. R1561–R1564, Mar 1997.

[112] R. Blume-Kohout, "Optimal, reliable estimation of quantum states," *New J. Phys.*, vol. 12, p. 043034, 2010.

[113] A. D. Wheelon, *Electromagnetic Scintillation.* Cambridge, U.K.: Cambridge University Press, 2004.

[114] A. N. Kolmogorov, "The local structure of turbulence in an incompressible viscous fluid for very large reynolds numbers," *C. R. (Doki) Acad. Sci. U.S.S.R.*, vol. 30, pp. 301–305, 1922.

[115] L. F. Richardson, *Weather Prediction by Numerical Process.* Cambridge, U.K.: Cambridge University Press, 2007.

[116] A. M. Obukhov, "On the spectrum of isotropic temperature fluctuations in an isotropic turbulence," *Izv. Acad. Nauk. SSSR, Ser. Georgr. I Geofiz*, vol. 13, pp. 58–69, 1949.

[117] S. Corrsin, "On the spectrum of isotropic temperature fluctuations in an isotropic turbulence," *J. Appl. Phys.*, vol. 22, pp. 469–473, 1951.

[118] D. W. Ricker, *Echo signal processing.* springer, 2003.

[119] V. I. Tatarskii, *The Effects of the Turbulent Atmosphere on Wave Propagation.* Jerusalem: trans. for NOVAA by Israel Program for science translations, 1971.

[120] A. Belmonte, "Feasibility study for the simulation of a beam propagation: consideration of coherent lidar performance," *Appl. Opt.*, vol. 39, pp. 5426–5445, 2000.

[121] D. L. Knepp, “Multiple phase-screen calculation of the temporal behavior of stochastic waves,” *Proc. IEEE*, vol. 71, pp. 722–737, 1983.

[122] W. K. Wootters, “Entanglement of formation of an arbitrary state of two qubits,” *Phys. Rev. Lett.*, vol. 80, pp. 2245–2248, 1998.

[123] A. K. Jha, G. A. Tyler, and R. W. Boyd, “Effects of atmospheric turbulence on the entanglement of spatial two-qubit states,” *Phys. Rev. A*, vol. 81, p. 053832, 2010.

[124] J. D. Schmidt, *Numerical Simulation of Optical Wave Propagation with With examples in MATLAB*. SPIE PRESS, 2010. Atmospheric optics.

[125] R. G. Lane, A. Glindemann, and J. C. Dainty, “Simulation of a kolmogorov phase screen,” *Waves in Random Media*, vol. 2, pp. 209–224, 1992.

[126] W. B. Miller, J. C. Ricklin, and L. C. Andrews, “Effects of the refractive index spectral model on the irradiance variance of a gaussian beam,” *J. Opt. Soc. Am. A*, vol. 11, p. 2719, 1994.

[127] T. Konrad, F. de Melo, M. Tiersch, C. Kasztelan, A. Aragao, and A. Buchleitner, “Evolution equation for quantum entanglement,” *Nature Physics*, vol. 4, p. 99, 2007.

[128] F. Mintert and A. Buchleitner, “Observable entanglement measure for mixed quantum states,” *Phys. Rev. L*, vol. 98, p. 140505, 2007.

[129] F. Mintert, “Robust entangled states,” *J. Phys. A: Math. Theor.*, vol. 43, p. 245303, 2010.

[130] R. T. Thew, K. Nemoto, A. G. White, and W. J. Munro, “Qudit quantum-state tomography,” *Phys. Rev. A*, vol. 66, p. 012303, 2002.

[131] F. Mintert, M. Kus, and A. Buchleitner, “Concurrence of mixed bipartite quantum states in arbitrary dimensions,” *Phys. Rev. Lett.*, vol. 92, p. 167902, 2004.

[132] G. Gour, “Family of concurrence monotones and its applications,” *Phys. Rev. A*, vol. 71, p. 012318, Jan 2005.

[133] G. Gour, “Mixed-state entanglement of assistance and the generalized concurrence,” *Phys. Rev. A*, vol. 72, p. 042318, Oct 2005.

[134] P. Rungta and C. M. Caves, “Concurrence-based entanglement measures for isotropic states,” *Phys. Rev. A*, vol. 67, p. 012307, Jan 2003.

[135] D. N. Klyshko, “Combined epr and two-slit experiments: Interference of advanced waves,” *Phys. Lett. A*, vol. 132, pp. 299–304, 1988.

[136] M. Mafu, A. Dudley, S. Goyal, D. Giovannini, M. McLaren, M. J. Padgett, T. Konrad, F. Petruccione, N. Lütkenhaus, and A. Forbes, “Higher-dimensional orbital-angular-momentum-based quantum key distribution with mutually unbiased bases,” *Phys. Rev. A*, vol. 88, p. 032305, Sep 2013.

[137] S. S. R. Oemrawsingh, J. A. de Jong, X. Ma, A. Aiello, E. R. Eliel, G. W. ’t Hooft, and J. P. Woerdman, “High-dimensional mode analyzers for spatial quantum entanglement,” *Phys. Rev. A*, vol. 73, p. 032339, Mar 2006.

[138] T. Brünner and F. S. Roux, “Robust entangled qutrit states in atmospheric turbulence,” *New J. Phys.*, vol. 15, p. 063005, 2013.

[139] S. M. Zhao, J. Leach, L. Y. Gong, J. Ding, and B. Y. Zheng, “Aberration corrections for free-space optical communications in atmosphere turbulence using orbital angular momentum states,” *Opt. Express*, vol. 20, p. 452, 2012.

[140] J. R.Taylor, *An Introduction to Error Analysis.* Sausalito, California: University Science Books, 1997.